UNIVERSITY OF CALIFORNIA
RIVERSIDE

Measurement of the Drell-Yan Differential Cross Section and Forward-Backward Asymmetry in $p\bar{p} \rightarrow e^+e^-$ Events using the DØ Detector

A Dissertation submitted in partial satisfaction
of the requirements for the degree of

Doctor of Philosophy

in

Physics

by

Raymond Gelhaus

August 2005

Dissertation Committee:
Dr. John Ellison, Chairperson
Dr. Benjamin Shen
Dr. Stephen Wimpenny

The Dissertation of Raymond Gelhaus is approved:

Committee Chairperson

University of California, Riverside

Acknowledgements

First, I would like to thank the DØ collaboration for all the countless hours they put in to make this detector such a huge success. Without such a large team effort, I would have nothing to present. I have been lucky to work with so many interesting and diverse people.

A large part of my success belongs to my advisor, Prof. John Ellison. He has taught me so much about high energy physics. He is a person that I look up to and hope I could be like. I would also like to thank the other members of the DØ collaboration at the University of Califoria, Riverside: Prof. Bob Clare, Dr. Ann Heinson, and Prof. Steve Wimpenny. They have all supported me throughout my time as a graduate student.

Many colleagues from the Electroweak group have also helped me along the way. Particularly, I would like to thank Dr. Dmitri Denisov, Dr. Ia Iashvili, Dr. Marco Verzocchi, Prof. Terry Wyatt, and Dr. Junjie Zhu, who gave me guidance and suggestions for improvement. The Editorial Board members: Prof. Cecilia Gerber, Prof. Tim Bolton, Dr. Alan Bross, Dr. Fred Borcherding, Dr. Thomas Nunnemann, Prof. Ken Johns, and Prof. Paul Padley, gave suggestions and input that was very important to get a clear understanding of the analysis.

Working in the Silicon Microstrip Tracker (SMT) and tracking algorithm groups have also helped to improve my knowledge of the detector and it's operation.

My great friend Tim Isberg and his family have treated me like part of their family. Tim is a person I could always count on being there for me. His kind of friendship is rare, and I really appreciate all he has done for me.

Last, but not least, I would like to thank my DØ friends who made this an enjoyable experience: Claus Buszello, Robert Harrington, Amber Jenkins, Lydia Lobo, Philip Perea, and Paul Telford.

To my

Mother

and

Sister

ABSTRACT OF THE DISSERTATION

Measurement of the Drell-Yan Differential Cross Section and Forward-Backward Asymmetry in $p\bar{p} \to e^+e^-$ Events using the DØ Detector

by

Raymond Gelhaus

Doctor of Philosophy, Graduate Program in Physics
University of California, Riverside, August 2005
Dr. John Ellison, Chairperson

We present measurements of the inclusive Drell-Yan e^+e^- differential cross section ($d\sigma/dM_{e^+e^-}$) and forward-backward asymmetry (A_{FB}) as a function of the dielectron invariant mass over the range $70 - 400$ GeV/c^2. The data sample consists of 177.3 pb^{-1} of $p\bar{p}$ collisions at $\sqrt{s} = 1.96$ TeV collected by the DØ detector. The results are consistent with the predictions of the standard model.

Contents

List of Figures

List of Tables

Chapter 1

Introduction

1.1 The Standard Model

The Standard Model describes how the fundamental units of matter (quarks and leptons) interact via the quanta associated with the fundamental forces of nature, called the gauge bosons. The quarks and leptons, collectively known as the fundamental fermions, appear to be pointlike when probed at the shortest distance scales accessible to current accelerators. The leptons have an intrinsic angular momentum of $\frac{1}{2}\hbar$ and are referred to as spin-1/2 particles. They have a charge of 0 or ± 1. There are three generations of leptons: (e ν_e), (μ ν_μ), (τ ν_τ), where the two highest generation leptons can decay into a lower generation lepton, except for the neutrinos, which do not decay. An example is the decay $\mu \rightarrow e\bar{\nu}_e\nu_\mu$. The quarks are also spin-1/2 particles, but have fractional electric charge and are not observed

individually in nature; the quarks are said to be "confined." The quarks also have three generations: $(u\ d)$, $(c\ s)$, and $(t\ b)$, where the two highest generation quarks can decay into a lower generation quark. Table 1.1 shows some properties of the fundamental fermions. For each fundamental fermion, there is a corresponding antifermion, which has the same mass and lifetime as the fermion, but which has the opposite sign of charge.

FERMIONS					
Leptons spin = 1/2			**Quarks** spin = 1/2		
Flavor	Mass (GeV/c^2)	Electric charge	Flavor	Mass (GeV/c^2)	Electric charge
electron neutrino (ν_e)	$< 1 \times 10^{-8}$	0	up (u)	0.003	2/3
electron (e)	0.000511	-1	down (d)	0.006	-1/3
muon neutrino (ν_μ)	< 0.0002	0	charm (c)	1.3	2/3
muon (μ)	0.106	-1	strange (s)	0.1	-1/3
tau neutrino (ν_τ)	< 0.02	0	top (t)	175	2/3
tau (τ)	1.7771	-1	bottom (b)	4.3	-1/3

Table 1.1: The matter constituents.

The gauge bosons mediate the four forces of nature: the strong, weak, electromagnetic, and gravitational forces. The photon (γ) mediates the electromagnetic force, the W^+, W^-, and Z^0 mediate the weak force, and the gluon mediates the strong force. The graviton is the gauge boson conjectured to mediate the gravitational force, although no self-consistent theory of quantum gravity has been found. The W^+, W^-, and Z^0 bosons are the only massive gauge bosons.

Properties of the gauge bosons and the fundamental interactions are shown in Tables 1.2 and 1.3.

BOSONS					
Unified Electroweak spin = 1			**Strong (color)** spin = 1		
Name	Mass (GeV/c^2)	Electric charge	Name	Mass (GeV/c^2)	Electric charge
photon (γ)	0	0	gluon (g)	0	0
W^-	80.4	-1			
W^+	80.4	+1			
Z^0	91.187	0			

Table 1.2: The force carriers.

PROPERTIES OF THE INTERACTIONS					
	Gravitational	Weak	Electromagnetic	Strong	
		Electroweak		Fundamental	Residual
Acts on:	Mass-Energy	Flavor	Electric Charge	Color Charge	
Particles experiencing:	All	Quarks, Leptons	Electrically charged	Quarks, Gluons	Hadrons
Particles mediating:	Graviton	W^+, W^-, Z^0	γ	Gluons	Mesons
Strength (rel. to electromag.) for two u quarks at:					
10^{-18} m	10^{-41}	0.8	1	25	N/A
3×10^{-17} m	10^{-41}	10^{-4}	1	60	N/A
for two protons in nucleus	10^{-36}	10^{-7}	1	N/A	20

Table 1.3: Properties of the four interactions of nature.

The gluons bind quarks together to form bound states of matter. Baryons are a bound state of three quarks, and mesons are composed of a quark and an antiquark. Collectively, mesons and baryons are referred to as hadrons. The proton consists of a *uud* bound quark state. The quark quantum numbers are additive, so the proton charge is +1 ($Q = \frac{2}{3} + \frac{2}{3} - \frac{1}{3}$). Table 1.4 shows properties of some of the baryons. The quantum numbers obey conservation laws: baryon number, lepton number, and isospin are conserved in strong interactions; strangeness is conserved in strong and electromagnetic interactions. All particle reactions conserve energy, momentum, angular momentum and electric charge. Quarks have an additional quantum number called "color." Otherwise there would be a problem for a baryon like the spin-3/2 omega (Ω^-), since there are three identical strange quarks in the same ground state with identical quantum numbers ($s \uparrow s \uparrow s \uparrow$), which is forbidden by the Pauli exclusion principle. Quarks have three primary color charges: red (R), green (G), and blue (B). Antiquarks have complementary colors: cyan ($\bar{R}$), magenta ($\bar{G}$), and yellow ($\bar{B}$). The Ω^-, is a $s_R s_G s_B$ quark bound state, and therefore the three strange quarks are not identical; they have different color quantum numbers. All particle states observed in nature are "colorless"; baryons have a color state "RGB" and mesons have color states of $R\bar{R}$, $G\bar{G}$, $B\bar{B}$. Gluons are the quanta of the color field that bind the quark states. They are bicolored and come in eight states: $R\bar{B}$, $R\bar{G}$, $B\bar{G}$, $B\bar{R}$, $G\bar{R}$, $G\bar{B}$, $\frac{1}{\sqrt{2}}(R\bar{R} - B\bar{B})$,

$\frac{1}{\sqrt{6}}(R\bar{R} + B\bar{B} - 2G\bar{G})$. We would expect $3^2 = 9$ combinations from three colors and three anticolors, but one state ($\frac{1}{\sqrt{3}}(R\bar{R} + B\bar{B} + G\bar{G})$) carries no net color and is excluded. Gluons can interact with other gluons, because they carry the color charge. If one tried to separate quarks in a bound state, the color force field will strengthen with distance, due to the gluon-gluon interactions. As energy is increased to overcome the color force field, there comes a point where it requires less energy to form a quark-antiquark pair from the vacuum, than to further increase the inter-quark separation. Therefore, a new meson is created and the quarks remain bound.

Some Baryons (qqq) and Antibaryons ($\bar{q}\bar{q}\bar{q}$)					
Symbol	Name	Quark content	Electric charge	Mass (GeV/c^2)	Spin
p	proton	uud	1	0.938	1/2
$\bar{p}$	anti-proton	$\bar{u}\bar{u}\bar{d}$	-1	0.938	1/2
n	neutron	udd	0	0.940	1/2
Λ	lambda	uds	0	1.116	1/2
Ω^-	omega	sss	-1	1.672	3/2

Table 1.4: Properties of some baryons.

1.2 Electroweak Interactions

One of the goals of physics is to have a unified theory of the four forces in nature. The unification of the electromagnetic and weak forces is described by the

electroweak theory of Glashow, Salam, and Weinberg [1]. This theory is based on four gauge fields, W_μ^i (i = 1, 2, 3) and B_μ, and the gauge symmetry group $SU(2)_L \times U(1)_Y$. This unification would take place at large energies much greater than 10^4 GeV. At low energies ($\leq$ 1 TeV), the symmetry is resulting in four separate vector bosons: one massless (photon) and three massive (W^+, W^-, and Z^0).

In the electromagnetic theory a current j_μ^{em} is coupled to the photon field A^μ with coupling e:

$$-ie(j^{em})^\mu A_\mu \tag{1.1}$$

In the electroweak theory there is an isotriplet of vector fields W_μ^i that have a coupling strength of g to the weak isospin current J_μ^i, plus a vector field B_μ coupled with strength $g'/2$ to the weak hypercharge current j_μ^Y. This leads to the electroweak interaction

$$-ig(J^i)^\mu W_\mu^i - i\frac{g'}{2}(j^Y)^\mu B_\mu. \tag{1.2}$$

Introducing a scalar isospin doublet (the Higgs field [2])

$$\phi = \begin{pmatrix} \phi^+ \\ \phi^0 \end{pmatrix}$$

with a vacuum expectation value

$$\phi_0 \equiv \sqrt{\frac{1}{2}} \begin{pmatrix} 0 \\ \\ v \end{pmatrix}$$

into the electroweak Lagrangian leads to the physical fields

$$\begin{aligned} W_\mu^\pm &= \sqrt{\frac{1}{2}}(W_\mu^1 \mp i W_\mu^2), & (1.3) \\ Z_\mu &= \frac{g W_\mu^3 - g' B_\mu}{\sqrt{g^2 + (g')^2}} = -\sin\,\theta_W B_\mu + \cos\,\theta_W W_\mu^3, & (1.4) \\ A_\mu &= \frac{g' W_\mu^3 + g B_\mu}{\sqrt{g^2 + (g')^2}} = \cos\,\theta_W B_\mu + \sin\,\theta_W W_\mu^3, & (1.5) \end{aligned}$$

with masses $M_W = \frac{1}{2}vg$, $M_Z = \frac{1}{2}v\sqrt{g^2 + (g')^2}$, and $M_A = 0$. Here we used the relation $g'/g = \tan\,\theta_W$, where θ_W is the weak mixing angle. Inserting Eqs. (1.4) and (1.5) into the electroweak neutral current part of Eq. (1.2), we obtain

$$\begin{aligned} -ig(J_\mu^3)(W^3)^\mu - i\frac{g'}{2}(j_\mu^Y)B^\mu = & \\ -i\left(g\,\sin\,\theta_W J_\mu^3 + g'\,\cos\,\theta_W \frac{j_\mu^Y}{2}\right) A^\mu & \\ -i\left(g\,\cos\,\theta_W J_\mu^3 - g'\,\sin\,\theta_W \frac{j_\mu^Y}{2}\right) Z^\mu. & (1.6) \end{aligned}$$

The first term can be compared to Eq. (1.1), where $ej_\mu^{em} \equiv e(J_\mu^3 + \frac{1}{2}j_\mu^Y)$, which leads to the unification relationship

$$g \sin \theta_W = g' \cos \theta_W = e. \tag{1.7}$$

Using these relations in the second term, we can define the weak neutral current J^{NC} as

$$J_\mu^{NC} \equiv J_\mu^3 - \sin \theta_W j_\mu^{em}. \tag{1.8}$$

1.3 The Drell-Yan Process

The Drell-Yan process describes the annihilation of a quark-antiquark pair and the production of a dilepton pair via an intermediate Z-boson or virtual photon (γ^*) [3]. This is shown in Fig. 1.1. The Drell-Yan process was first observed by colliding protons on a uranium target and detecting the resulting muon pairs; this was done by a group at Brookhaven National Laboratory led by Leon Lederman in 1968 [4]. The first experimental observation of the e^+e^- final state was by a group led by Samuel Ting at Brookhaven in 1974 [5].

To calculate the lowest order Drell-Yan cross section, we begin by considering the parton-level differential cross section $d\hat{\sigma}(q\bar{q} \to \gamma^*/Z^0 \to l^+l^-)/d\theta$, where θ is the polar emission angle of the electron in the rest frame of the e^+e^-

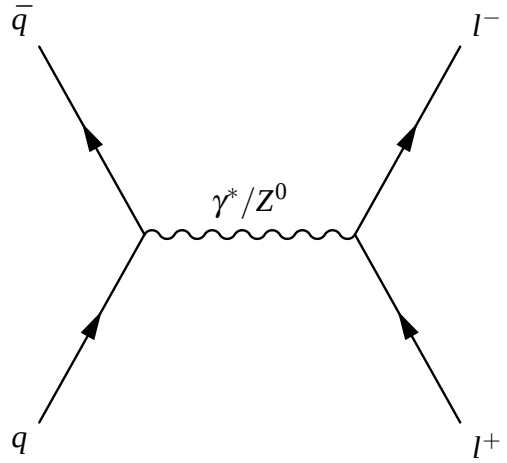

Figure 1.1: Feynman diagram of the parton-level Drell-Yan process.

pair. The differential cross section is given by

$$\frac{d\hat{\sigma}}{d\cos\theta} = \frac{1}{32\pi\hat{s}}\overline{|\mathcal{M}|^2}(q\bar{q} \to \gamma^*/Z^0 \to \ell^+\ell^-), \tag{1.9}$$

where $\mathcal{M}$ is the invariant amplitude for the Feynman diagram in Fig. 1.1, and

$$\overline{|\mathcal{M}|^2} \;=\; \left(\frac{1}{3}\right)_{q \text{ colors}} \cdot \left(\frac{1}{3}\right)_{\bar{q} \text{ colors}} \cdot \left(\frac{1}{2}\right)_{q \text{ spin}} \cdot \left(\frac{1}{2}\right)_{\bar{q} \text{ spin}} \cdot \sum_{\text{colors}} \sum_{\text{spins}} |\mathcal{M}|^2$$

and $\hat{s} = q^2 = (2E)^2$ is the center-of-mass energy of the $q\bar{q}$ interaction. The spins and colors of the incoming quarks are unknown, so we must average over these quantities and then sum over the spins of the final state leptons. We have

$$|\mathcal{M}|^2 = \mathcal{M}^\dagger\mathcal{M}$$

where $\mathcal{M}^\dagger = (\mathcal{M}^*)^{\mathrm{T}}$. For the photon propagator diagram we have

$$\mathcal{M}_\gamma = -e_q^2[\bar{u}(p_3)\gamma^\mu v(p_4)]\frac{g_{\mu\nu}}{q^2}[\bar{v}(p_2)\gamma^\nu u(p_1)],$$

while for the Z propagator diagram,

$$\mathcal{M}_Z = -\frac{g_Z^2}{4}[\bar{u}(p_3)\gamma^\mu(c_V^f - c_A^f\gamma^5)v(p_4)][\bar{v}(p_2)\gamma^\nu(c_V^e - c_A^e\gamma^5)u(p_1)]$$

$$\times \left(\frac{g_{\mu\nu} - q_\mu q_\nu/M_Z^2}{q^2 - M_Z^2 + iq^2\Gamma_Z/M_Z}\right),$$

where: p_1, p_2, p_3, p_4 are the 4-momenta of the e^-, e^+, q, $\bar{q}$ respectively; q is the 4-momentum of the propagator; e is the electron charge; $g_Z = e/\sin\theta_W\cos\theta_W$; θ_W is the weak mixing angle; $g_{\mu\nu}$ is the metric tensor; M_Z, Γ_Z are the mass and total decay rate of the Z-boson; and c_V, c_A are the vector and axial-vector couplings of the quarks and leptons (see Table 1.5). The Dirac particle and antiparticle spinors are $u(p)$ and $v(p)$, while $\bar{u}(p)$ and $\bar{v}(p)$ are the conjugate spinors defined by $\bar{u} \equiv u^\dagger\gamma^0$ and $\bar{v} \equiv v^\dagger\gamma^0$. The Dirac matrices are defined by

$$\gamma^0 = \begin{pmatrix} I & 0 \\ 0 & -I \end{pmatrix}, \gamma = \begin{pmatrix} 0 & \boldsymbol{\sigma} \\ -\boldsymbol{\sigma} & 0 \end{pmatrix}, \gamma^5 = \begin{pmatrix} 0 & I \\ I & 0 \end{pmatrix},$$

where I is the identity matrix and $\boldsymbol{\sigma} = (\sigma_1, \sigma_2, \sigma_3)$ are the Pauli spin matrices. The result for the differential cross section when only the photon exchange diagram

	c_V	c_A
e	$-\frac{1}{2} + 2\sin^2(\theta_W)$	$-\frac{1}{2}$
q (u-type)	$\frac{1}{2} - \frac{4}{3}\sin^2(\theta_W)$	$\frac{1}{2}$
q (d-type)	$-\frac{1}{2} + \frac{2}{3}\sin^2(\theta_W)$	$-\frac{1}{2}$

Table 1.5: Axial and axial-vector couplings of the electron and quarks.

is considered is

$$\frac{d\hat{\sigma}(q\bar{q} \to \gamma^* \to \ell^+\ell^-)}{d\cos\theta} = \frac{e_q^2}{3}\frac{\pi\alpha^2}{2\hat{s}}(1+\cos^2\theta), \tag{1.10}$$

where α is the fine structure constant defined by $\alpha^2 = e^4/16\pi^2$. Note that this differential cross section is symmetric in $\cos\theta$. The total cross section is

$$\hat{\sigma}(q\bar{q} \to \gamma^* \to \ell^+\ell^-) = \frac{4\pi\alpha^2}{9\hat{s}}e_q^2 = \frac{4\pi\alpha^2}{9M^2}e_q^2. \tag{1.11}$$

For the Z propagator diagram, we find

$$\frac{d\hat{\sigma}(q\bar{q} \to Z^0 \to e^+e^-)}{d\cos\theta} = \frac{g_Z^4 E^2}{128\pi[(4E^2 - M_Z^2)^2 + 16E^4\Gamma_Z^2/M_Z^2]}$$
$$\times [[(c_V^f)^2 + (c_A^f)^2][(c_V^e)^2 + (c_A^e)^2][(1+\cos^2\theta)] - 8c_V^f c_A^f c_V^e c_A^e \cos\theta] \tag{1.12}$$

Note that due to the last term this is not symmetric in $\cos\theta$, i.e. there is a forward-backward asymmetry. Forward events are those for which the electron is in the forward hemisphere ($\cos\theta > 0$) and backward events have the electron in the

backward hemisphere ($\cos\theta < 0$). The total cross section is given by

$$\hat{\sigma}(q\bar{q} \to Z^0 \to e^+e^-) = \frac{g_Z^4 E^2}{48\pi} \frac{[(c_V^f)^2 + (c_A^f)^2][(c_V^e)^2 + (c_A^e)^2]}{[(4E^2 - M_Z^2)^2 + 16E^4\Gamma_Z^2/M_Z^2]}. \tag{1.13}$$

For $\hat{s} \approx M_Z^2$, where $\hat{s} = q^2 = (2E)^2 = M_Z^2$,

$$\hat{\sigma}(q\bar{q} \to Z^0 \to e^+e^-) = \frac{g_Z^4}{192\pi\Gamma_Z^2}[(c_V^f)^2 + (c_A^f)^2][(c_V^e)^2 + (c_A^e)^2]. \tag{1.14}$$

To obtain the cross section for proton-antiproton scattering ($p\bar{p} \to \gamma^*/Z^0 \to \ell^+\ell^-$) we must convolve the partonic cross section with the parton distribution functions. The full Drell-Yan cross section is

$$\sigma(p\bar{p} \to \gamma^*/Z^0 \to \ell^+\ell^-) = \sum_{flavor} \int_0^1 \int_0^1 dx_a dx_b f_a(x_a) f_b(x_b) \hat{\sigma}(q\bar{q} \to \gamma^*/Z^0 \to \ell^+\ell^-), \tag{1.15}$$

where $f_a(x_a), f_b(x_b)$ are the parton distributions functions for the interacting partons, and x_a, x_b are the fractions of the proton or antiproton momentum carried by partons a and b respectively.

Higher order corrections to the leading order cross section due to QED radiative corrections and QCD corrections have been calculated by the authors of Refs. [6] and [7, 8] respectively.

1.4 The Forward-Backward Asymmetry

The presence of both vector and axial-vector couplings of the quarks and leptons to the Z-boson gives rise to an asymmetry in the polar emission angle θ of the electron in the rest frame of the e^+e^- pair. The differential cross section for the parton level process $q\bar{q} \to \gamma^*/Z^0 \to e^+e^-$ can be written

$$\begin{aligned}\frac{d\sigma(q\bar{q} \to \gamma^*/Z^0 \to e^+e^-)}{d\cos\theta} = \\ C\frac{\pi\alpha^2}{2\hat{s}}[e^2e_q^2(1+\cos^2\theta) + ee_qRe(\chi(\hat{s}))(2c_V^fc_V^e(1+\cos^2\theta) + 4c_A^fc_A^e\cos\theta) \\ + |\chi(\hat{s})|^2\left(((c_V^f)^2+(c_A^f)^2)((c_V^e)^2+(c_A^e)^2)(1+\cos^2\theta)\right) \\ + |\chi(\hat{s})|^2\left(8c_V^fc_A^fc_V^ec_A^e\cos\theta\right)] \end{aligned} \tag{1.16}$$

where C is the color factor, e is the electron charge, e_q is the quark charge, θ is the emission angle of the electron relative to the quark in the e^+e^- rest frame, and $\chi(\hat{s}) = (1/\cos^2\theta_W\sin^2\theta_W)\cdot(\hat{s}/(\hat{s}-M_Z^2+i\Gamma_ZM_Z))$. Here we have included the γ^*/Z^0 interference term (second term) along with the pure γ^* and Z^0 terms from Section 1.3. Defining the following variables:

$$\begin{aligned} R^{VV} &\equiv e^2e_q^2 + 2ee_qc_V^fc_V^eRe(\chi(\hat{s})) + (c_V^e)^2((c_V^f)^2+(c_A^f)^2)|\chi(\hat{s})|^2, \\ R^{AA} &\equiv (c_A^e)^2((c_V^f)^2+(c_A^f)^2)|\chi(\hat{s})|^2, \\ R^{VA} &\equiv \frac{3}{2}c_A^fc_A^e(ee_qRe(\chi(\hat{s})) + 2c_V^fc_V^e|\chi(\hat{s})|^2), \end{aligned}$$

we can simplify Eq. (1.16) to the following expression:

$$\frac{d\sigma(q\bar{q} \to \gamma^*/Z^0 \to e^+e^-)}{d\cos\theta^*} = C\frac{4}{3}\frac{\pi\alpha^2}{\hat{s}}R_f[\frac{3}{8}(1+\cos^2\theta) + A_{FB}\cos\theta] \tag{1.17}$$

where

$$R_f = R^{VV} + R^{AA}, \tag{1.18}$$

and

$$A_{FB} = \frac{R^{VA}}{R_f}. \tag{1.19}$$

The first term in square brackets in Eq. 1.17 integrates to 1, and the second term integrates to zero. The total parton-level cross section can then be written as $\sigma_{tot} = CR_f\sigma_{QED}$, where σ_{QED} is the QED cross section and R_f depends on the lepton and quark couplings (Eq. 1.18). The forward-backward asymmetry A_{FB} can be written as

$$A_{FB} = \frac{\sigma_F - \sigma_B}{\sigma_F + \sigma_B} \tag{1.20}$$

where the forward and backward cross sections are defined by

$$\sigma_F \equiv \int_0^1 \frac{d\sigma}{d\cos\theta} d\cos\theta \tag{1.21}$$

$$\sigma_B \equiv \int_{-1}^0 \frac{d\sigma}{d\cos\theta} d\cos\theta. \tag{1.22}$$

The forward-backward asymmetry calculated as a function of the e^+e^- mass for the up and down quarks is shown in Fig. 1.2.

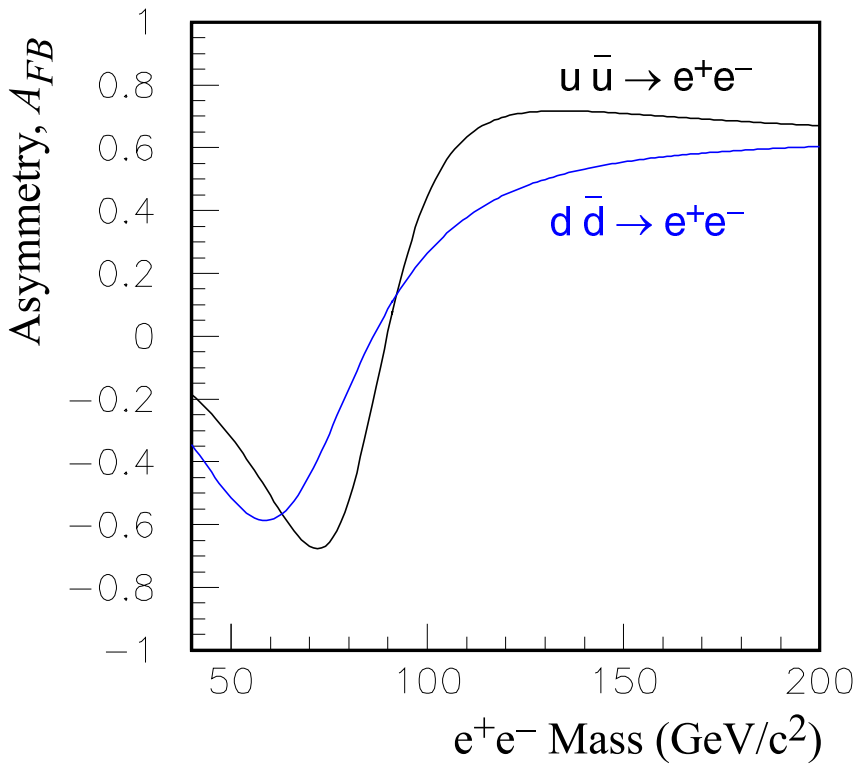

Figure 1.2: The forward-backward asymmetry for u and d quark annihilation into a dielectron final state. Taken from [9].

To minimize the effect of the unknown transverse momenta of the incoming quarks in the measurement of the forward and backward cross sections, we use the Collins-Soper reference frame [10]. This reference frame reduces the uncertainty in electron polar angle due to the finite transverse momentum of the incoming quarks. The particle four-vectors are transformed to the e^+e^- rest frame and the polar angle θ^* is measured with respect to the z-axis, defined as the bisector of the proton beam momentum vector $\mathbf{P}_1$ and the negative antiproton beam momentum

vector $-\mathbf{P}_2$, as shown in Fig. 1.3. The y-axis is parallel to $\mathbf{P_1} \times \mathbf{P_2}$, and $\cos\theta^*$ is given by [10]

$$\cos\theta^* = 2Q^{-1}(Q^2 + Q_T^2)^{-1/2}(l^+\bar{l}^- - l^-\bar{l}^+) \tag{1.23}$$

where l^ν is the electron four-momentum in the lab frame, $\bar{l}^\nu$ is the positron four-momentum in the lab frame, $Q^\nu = l^\nu + \bar{l}^\nu$ is the dielectron four-momentum in the lab frame, and $l^\pm = 2^{-1/2}(E_l \pm p_{zl})$.

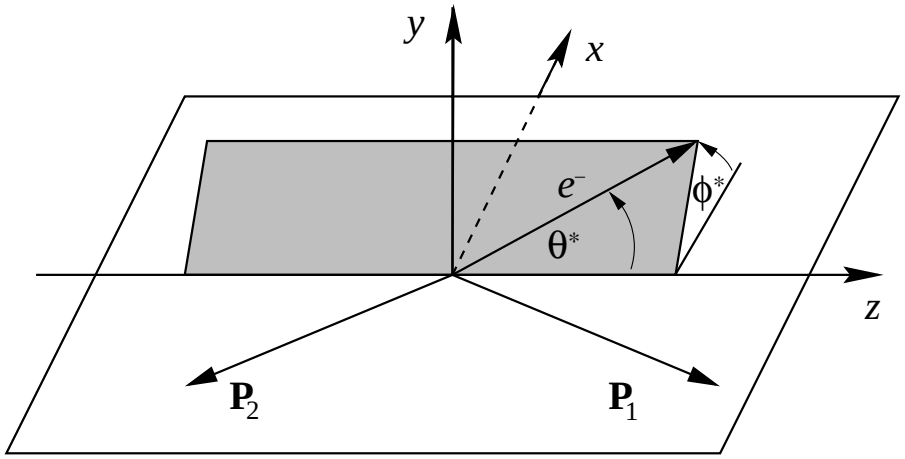

Figure 1.3: The Collins-Soper reference frame. The angle θ^* is measured with respect to the z-axis defined as the bisector of the proton beam momentum $\mathbf{P}_1$ and the negative of lab-frame antiproton beam momentum $-\mathbf{P}_2$. $\mathbf{P}_1$ and $\mathbf{P}_2$ are measured in the e^+e^- rest frame.

1.5 Importance of the Drell-Yan Process and Forward-Backward Asymmetry

The Drell-Yan process offers many interesting and important characteristics for study. First, the Drell-Yan process is directly comparable to the Standard Model theory. Therefore, we can confirm if this theory is correct, or if it does indeed breakdown. The Drell-Yan process is also unaffected by complex QCD final state interactions. This gives us a clean signal with a small background.

The forward-backward asymmetry depends on the vector and axial-vector couplings of the quarks and leptons to the Z-boson and is therefore sensitive to the effective weak mixing angle $\sin^2\bar{\theta}_W$ [9]. The weak mixing angle is an important constant in the electroweak theory that describes the connection between the weak and electromagnetic interactions. The largest asymmetry occurs at center-of-mass energies of around 70 GeV and above 110 GeV (see Fig. 1.2). At the Z-pole the asymmetry is dominated by the couplings of the Z-boson and arises from the interference of the vector and axial-vector components of its coupling. At large invariant mass the asymmetry is dominated by γ^*/Z interference and is almost constant (≈ 0.6), independent of invariant mass. The Tevatron allows measurement of the forward-backward asymmetry at partonic center-of-mass energies above the center-of-mass energy of LEP II. This measurement can be used not only to confirm the standard model γ^*/Z interference which dominates in this region, but

also to investigate possible new phenomena which may alter A_{FB} such as new neutral gauge bosons [11] or large extra dimensions [12].

Figure 1.4 shows some examples of the effects new neutral gauge bosons would have on the forward-backward asymmetry. In grand unified theories (GUTs), the electroweak theory based on SU(2) $\times$ U(1) gauge symmetry is embedded into a larger group. For example, a GUT based on SO(10) has SO(10) $\supset$ SU(5) $\times$ U(1), where SU(5) contains the Standard Model gauge group, SU(5) $\supset$ SU(3) $\times$ SU(2) $\times$ U(1). The breaking of SO(10) to SU(5) $\times$ U(1) implies the existence of an extra neutral gauge boson associated with the U(1) group, which is denoted Z_χ. For GUTs associated with E_6, we have $E_6 \supset$ SO(10) $\times$ U(1). The new neutral gauge boson associated with E_6 breaking is denoted Z_ψ. When E_6 breaks down into the subgroup SU(6)$\times$SU(2)$_I$, the $I_{3I} = 0$ element of the SU(2)$_I$ triplet is the Z_I gauge boson.

Models with large extra dimensions have been introduced [13, 14] to solve the hierarchy problem; the huge disparity between the weak scale ($\sim$ 100 GeV) and the Planck scale ($M_{Pl} \sim 10^{19}$ GeV). In these models our 3-dimensional brane is embedded in a $3 + n$ higher dimensional space. Standard model fields are confined to the 3-dimensional brane, while gravity can propagate in all $3 + n$ dimensions (the "bulk"). The equation $M_{Pl}^2 \sim r^n M_{eff}^{2+n}$ relates the Planck scale (M_{Pl}) to the fundamental scale of the extra dimensions, where r is the size of the additional dimensions, n is the number of extra dimensions, and M_{eff} is the effective Planck

scale in the bulk. If we take M_{eff} to be around a TeV, gravity can become strong near the weak scale. This theory can be tested by indirectly observing the effects of a Kaluza Klein (KK) tower of massive gravitons that interact with the SM fields on the 3-d brane [15]. The effects of large extra dimensions is shown in Fig. 1.5, where λ is a coefficient of the n massive graviton matrix element that depends on the number of extra dimensions, and how they are compactified.

The analysis presented in this thesis is directed at testing the standard model predictions of the forward-backward asymmetry over the invariant mass range $70 - 400$ GeV.

1.6 Experimental Status and Expectations

The ALEPH, DELPHI, L3, and OPAL experiments at the LEP e^+e^- collider at CERN measured the cross sections and forward-backward asymmetries for the processes: $e^+e^- \rightarrow \mu^+\mu^-$, $\tau^+\tau^-$ [16], $c\bar{c}$ [17], and $b\bar{b}$ [18] at the Z-pole and at center-of-mass energies of 130-207 GeV. These processes are closely related to the process $q\bar{q} \rightarrow e^+e^-$. They found good agreement with the Standard Model.

Measurements of the Drell-Yan process have been made at the Tevatron $p\bar{p}$ collider at Fermilab in Run I (1992-1996), with a center-of-mass collision energy of 1.8 TeV and data sets of integrated luminosity of around 100 pb^{-1}. The Drell-Yan cross section was measured by the DØ [19] and CDF collaborations [20]. CDF also

measured the forward-backward asymmetry [20]. Both experiments found good agreement with the Standard Model. A slight excess of events was seen at $M_{ee} \approx$ 350 GeV by CDF, which was 2.2σ below the standard model A_{FB} prediction. Figure 1.6 shows the DØ and CDF cross sections and the CDF A_{FB} measurement.

In Run IIa, CDF has measured the forward-backward asymmetry using a data set of 72 pb^{-1} at a center-of-mass energy of 1.96 TeV [21]. This result also shows agreement with the Standard Model. There was no excess of events in the higher mass regions that would imply physics beyond the standard model. The CDF RunIIa forward-backward asymmetry is shown Fig. 1.7.

A study of the expected precision with which A_{FB} can be measured at has been reported in Ref. [22]. Assuming 10 fb^{-1} of integrated luminosity, the precision on the forward-backward asymmetry and $\sin^2\theta_W$ were estimated to be: $\delta A_{FB} =$ 0.0014 (e^+e^-), 0.0005 ($\mu^+\mu^-$) and $\delta\sin^2\theta_W = 0.00028$ (combined e^+e^-, $\mu^+\mu^-$, DØ and CDF).

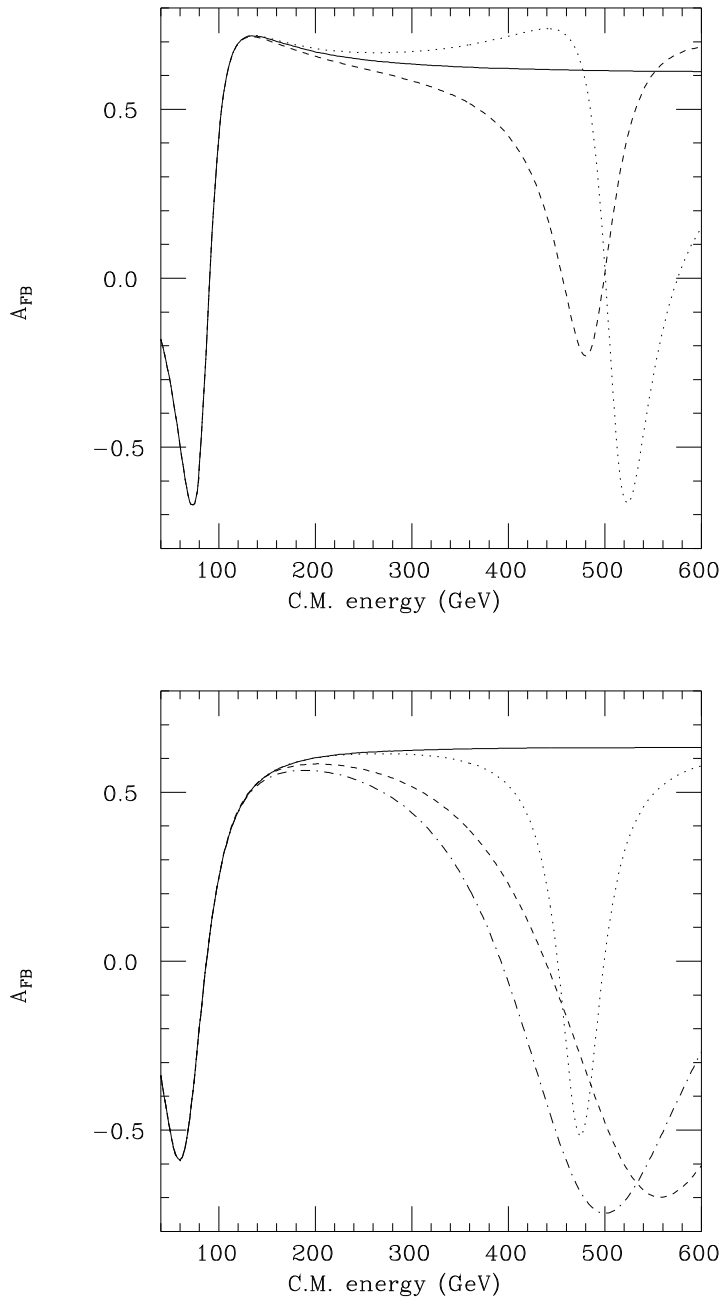

Figure 1.4: The theoretical forward-backward asymmetry with additions of new neutral gauge bosons. The top plot shows A_{FB} for the parton-level process $u\bar{u} \rightarrow e^{-}e^{+}$, and the bottom plot shows A_{FB} for the process $d\bar{d} \rightarrow e^{-}e^{+}$. The solid line is the standard model prediction. The dashed line describes the addition of a 500 GeV/c^2 Z_χ. The dotted line is for a 500 GeV/c^2 Z_ψ, and the dot-dashed line is for a 500 GeV/c^2 Z_I. Taken from [11].

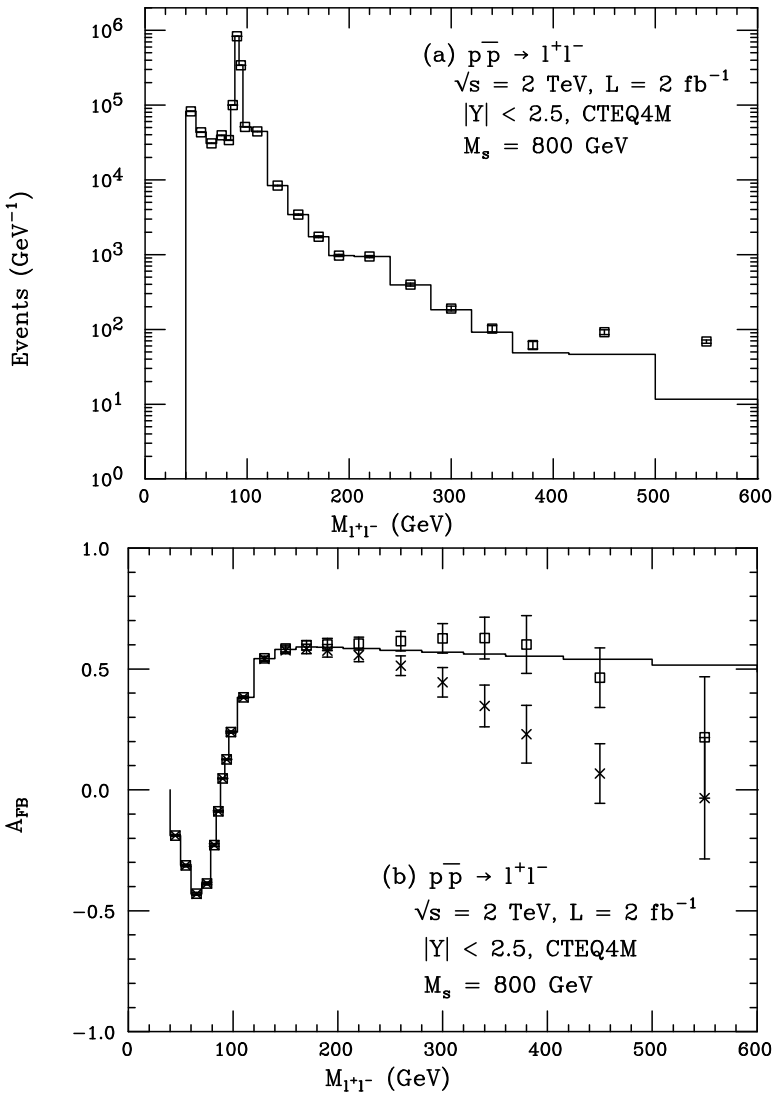

Figure 1.5: The predicted number of events as a function of M_{ee} (top) and the forward-backward asymmetry vs. M_{ee} (bottom) with the addition of two large extra dimensions. The solid line is the standard model prediction. The points show the effect from a graviton exchange with $\lambda = \pm 1$. Taken from [12].

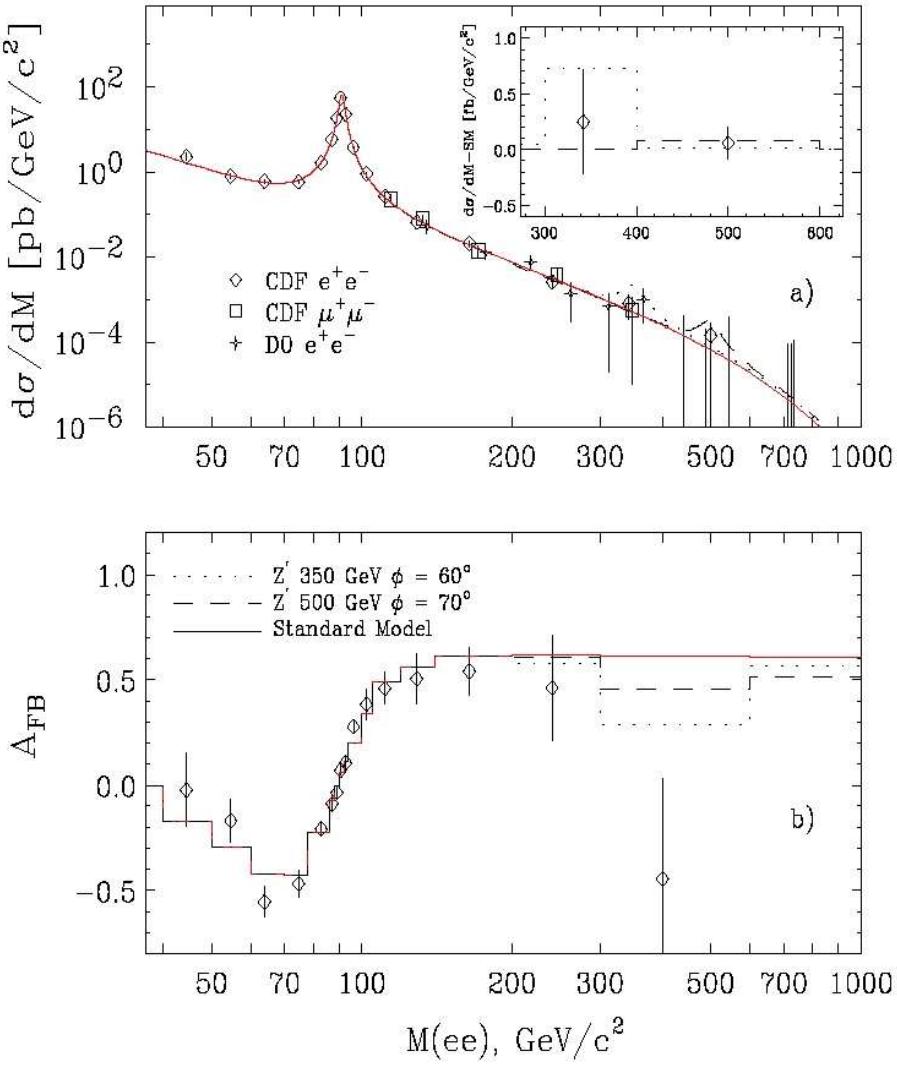

Figure 1.6: The Run I DØ and CDF Drell-Yan measurements. Taken from [20].

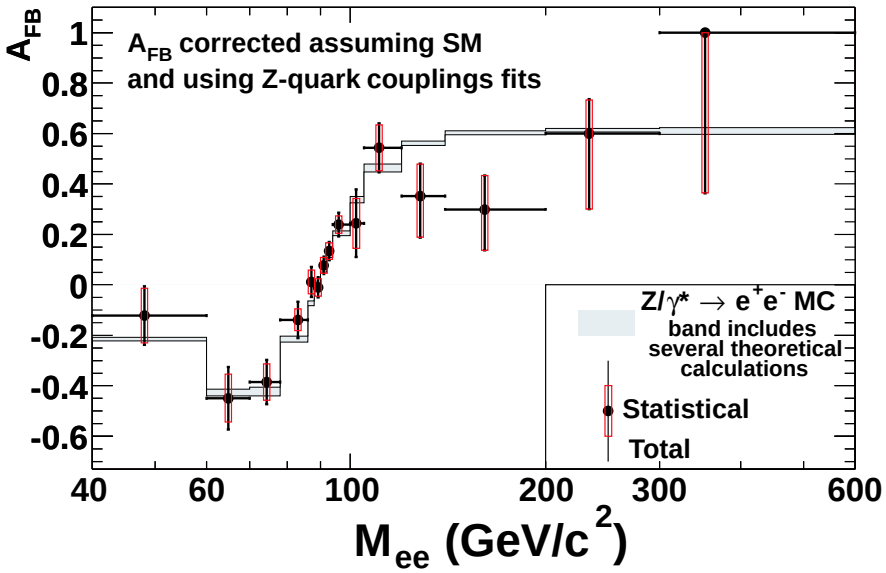

Figure 1.7: The Run II CDF forward-backward asymmetry measurement. Taken from [21].

Chapter 2

Experimental Apparatus

2.1 The Particle Accelerator

The Tevatron is currently the highest energy accelerator in operation in the world. It produces beams of protons and antiprotons with energies of almost 1 TeV, using radio-frequency electric fields for acceleration and a combination of dipole and quadrapole magnets to direct and focus the particles in a circular beam tunnel of radius 1 km. The protons can be sent to a fixed target, or they can collide with antiprotons in detectors around the Tevatron ring. The Tevatron accelerator complex is shown in Figure 2.1. The Tevatron accelerator is only part of a chain of accelerators in the complex. A detailed description of the Tevatron complex can be found in Ref. [23].

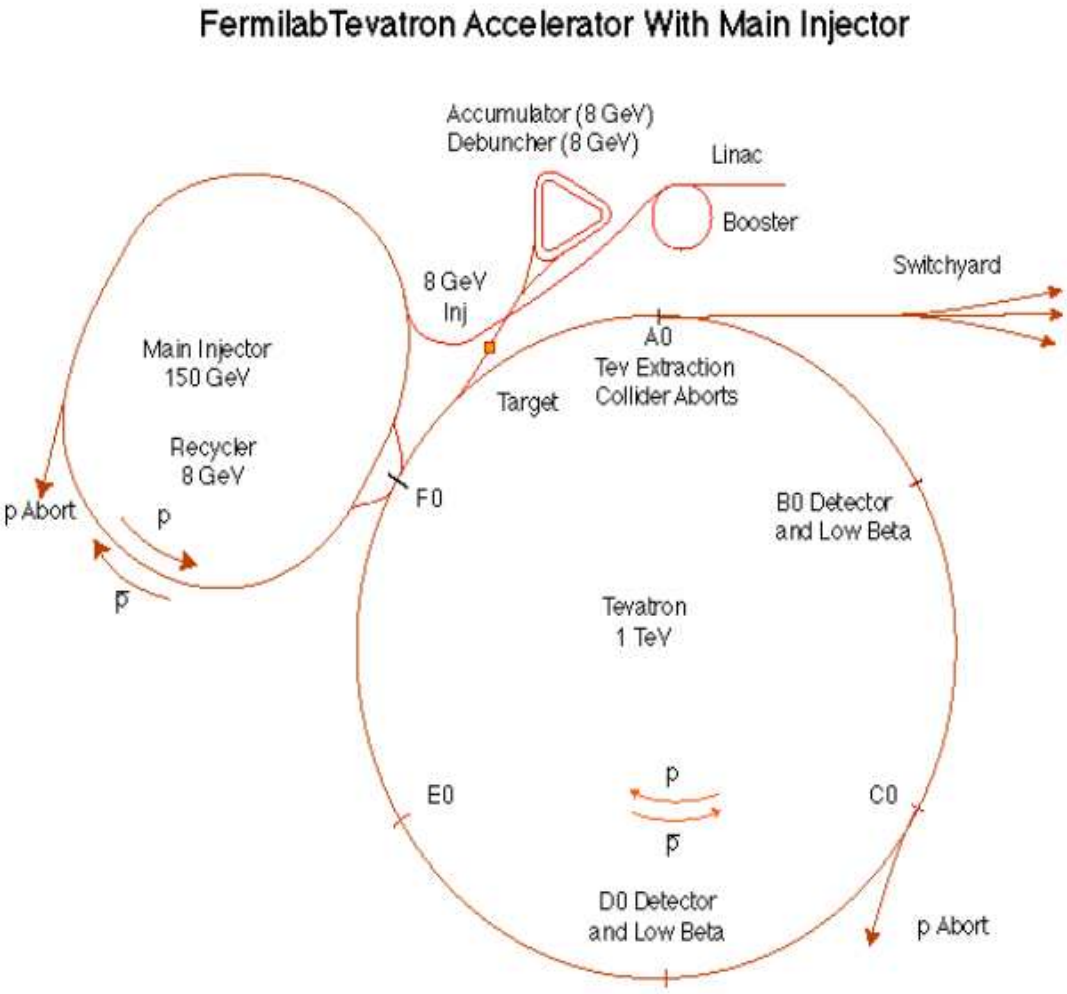

Figure 2.1: The Fermilab Tevatron accelerator.

The acceleration process begins in a Cockcroft-Walton pre-accelerator, which takes negative hydrogen ions from a magnetron source and accelerates the 1.4 x 10^{14} H^- ion bunches to 750 keV. The hydrogen ions are then accelerated to 400 MeV in the Linac [24], which is a linear accelerator 150 m in length; consisting of 12 radio-frequency (RF) cavities. The RF cavities increase in length along the direction of acceleration, which provides constant particle acceleration. At the end of the Linac stage, the hydrogen ions are passed through a carbon foil to remove the electrons, so only the protons continue through the acceleration process. The protons are injected into the Booster [25], a rapid cycling synchrotron, to further accelerate the protons to 8 GeV. The Booster has 17 RF cavities for acceleration, and it has magnets to steer and focus the beam of protons. The Booster ring is 475 m in circumference. Once the protons have been processed through the Booster, they are sent to the Main Injector [24], which is approximately 3 km in circumference. The Main Injector can accelerate protons from 8 GeV to 150 GeV for injection to the Tevatron, or to 120 GeV for use in antiproton production.

To create antiprotons [26], the 120 GeV protons are sent from the Main Injector to a target area, where the protons collide with a nickel target. The result of the collision produces antiprotons, plus many other secondary particles, which come off the target at many different angles. Following the nickel target is a lithium collection lens. This produces a solenoidal magnetic field, which focuses the particles into a beam line. The peak energy of the antiprotons after the collision

with the nickel target is 8 GeV. A pulsed dipole magnet is used after the nickel target to select 8 GeV negatively charged particles. The 8 GeV antiprotons are then sent to the Debuncher, which narrows the momentum spread and reduces the transverse profile of the antiproton beam. The antiprotons are then transferred to the Accumulator, which stores the antiproton beam for hours or days until more antiprotons are needed in the Tevatron. This is accomplished by momentum stacking successive pulses of antiprotons from the Debuncher. The injection orbit is located at about 80 mm to the outside of the core orbit of the stored antiprotons. A RF cooling system decelerates the antiprotons from there injection orbit to the core orbit of the accumulated antiprotons, and the beam is further cooled. Once there are enough antiprotons in the Accumulator, they can be transferred to the Main Injector to be accelerated to 150 GeV and sent into the Tevatron.

Protons and antiprotons are accelerated to a energy of 0.98 TeV in opposite directions in the 1-km-radius Tevatron ring [24]. This circular synchrotron contains about 1,000 superconducting magnets, which operate in the temperature range of liquid helium (4.6 K). Once the beam of protons and antiprotons have reached an energy of 0.98 TeV, they are focused by quadrapole magnets and are made to collide at the DØ and BØ interaction regions, where the DØ and CDF detectors are located. There are 36 proton bunches and 36 antiproton bunches in the Tevatron, with a bunch crossing occurring every 396 ns.

2.2 The DØ Detector

2.2.1 Overview

The DØ detector is a multi-purpose particle detector [27]. It weighs 5500 tons and its dimensions are 13 m (height) x 11 m (width) x 17 m (length). The innermost region, closest to the interaction point, contains a tracking system comprised of the Silicon Microstrip Tracker (SMT), the Central Fiber Tracker (CFT), and a 2 Tesla superconducting solenoid magnet. The energies of electrons, photons, and jets, are measured in liquid-argon/uranium calorimeters located outside the solenoid. Preshower detectors, located between the solenoid and calorimeters aide in electron identification. Beyond the calorimeters is a muon detection system with a 2 Tesla toroid magnet. All these detector systems are connected to a trigger and data acquisition system, used to pick out the interesting physics events. Figure 2.2 shows a general overview of the DØ detector.

The DØ coordinate system is such that protons travel in the $+z$ (south) direction, and antiprotons travel in the -z direction (north). Using a standard right-handed coordinate system, the $+x$ axis points out radially (east), and the $+y$ axis points up vertically. DØ also uses cylindrical and spherical coordinates, where the polar angle, θ, is in the $y-z$ plane, and the azimuthal angle, ϕ, is in the $x-y$ plane. A useful quantity used in describing the longitudinal momentum dependence

of cross sections is the rapidity, y, defined by:

$$y = \frac{1}{2} \ln \left(\frac{E + p_z}{E - p_z} \right). \tag{2.1}$$

In the limit $p \gg m$, the rapidity becomes

$$y \approx -\ln[\tan(\theta/2)] \equiv \eta, \tag{2.2}$$

where η is called the pseudorapidity.

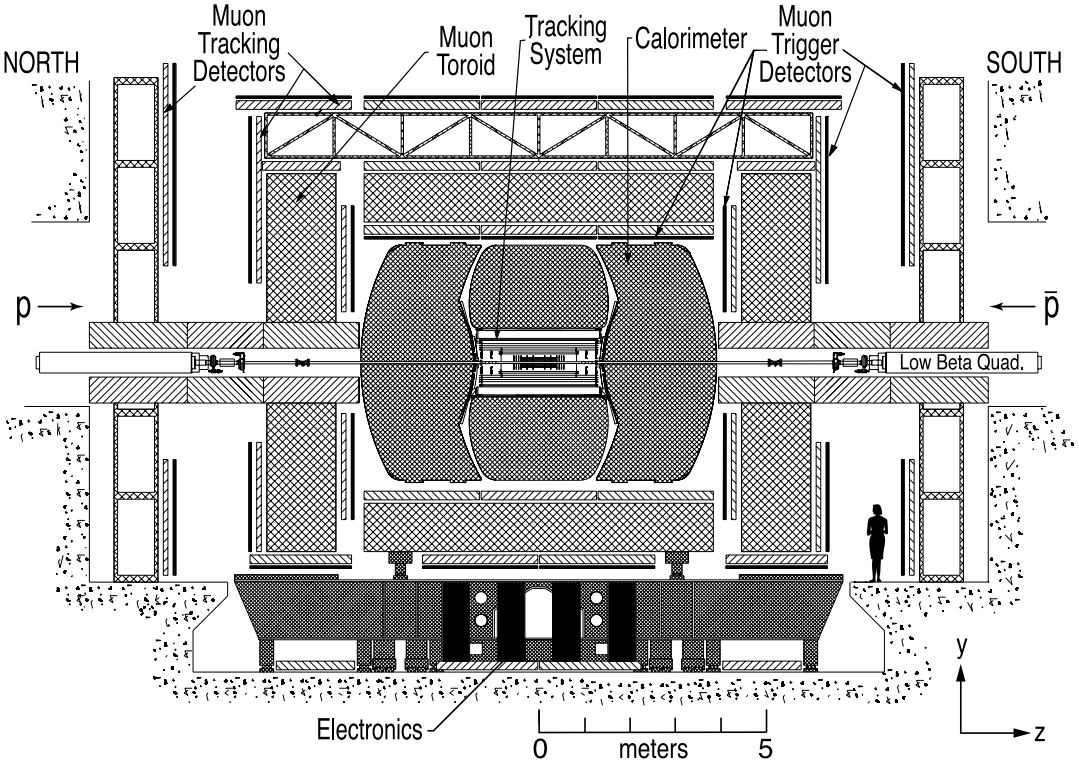

Figure 2.2: The DØ detector.

2.2.2 Silicon Microstrip Tracker

The Silicon Microstrip Tracker (SMT) [28] is the closest detector subsystem to the beamline (see Fig. 2.3), and hence to the proton-antiproton collision region. It has the highest position resolution of all the sub-detectors and is used to match tracks to the primary vertex ($p\bar{p}$ interaction point) or to a secondary vertex associated with a long-lived particle like a B hadron. With the help of the 2 Tesla superconducting solenoid magnet and the Central Fiber Tracker, the SMT is used to determine the momentum of charged particles. The SMT has a $r - \phi$ hit resolution of approximately 10 μm.

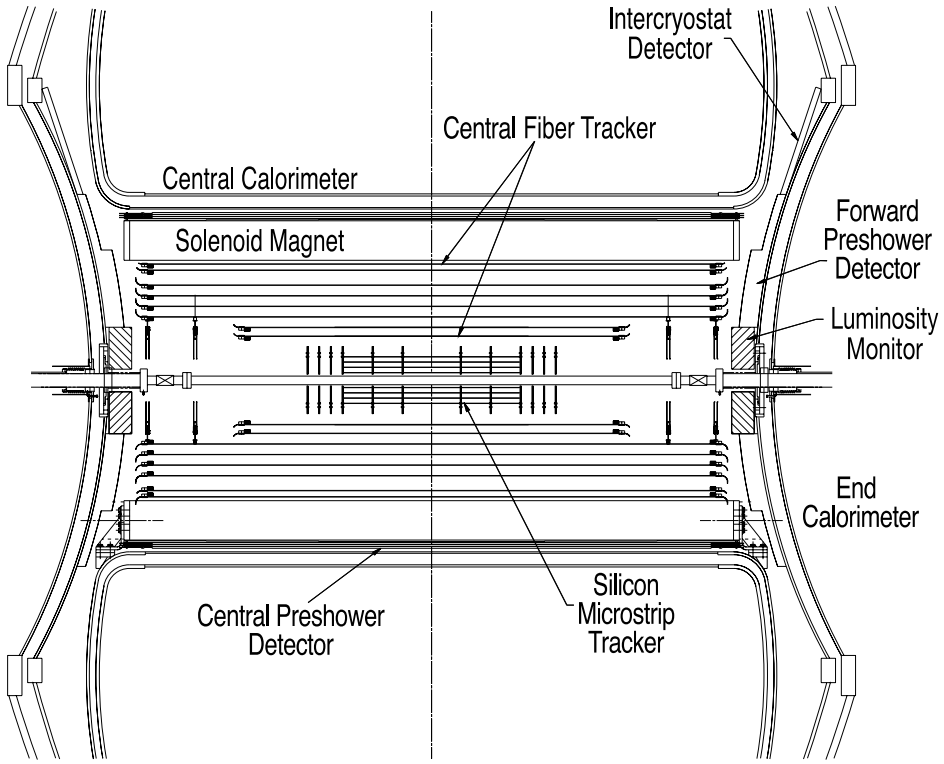

Figure 2.3: The central tracking system.

The interaction region has a mean at $z = 0$ and a standard deviation of σ_z = 28 cm. In order to track particles originating from this relatively long interaction region out to $\eta \approx 2.5$, the SMT was designed with a hybrid system of barrel detectors and interspersed disks in the central region, with larger-radius disks in the forward regions. The design is shown in Fig. 2.4. The SMT has the following components with an overall active length of 1.10 m:

- 6 barrel segments
- 4 detector layers per barrel
    - double-sided layers in the four central barrels
    - single-sided (layers 1 and 3) and double-sided (layers 2 and 4) in the two outer barrels
- 12 F (small diameter) double-sided disks
- 4 H (large diameter) single-sided disks

The barrel sections are 12.0 cm long and 21.0 cm in diameter. Each barrel comprises four layers of silicon modules (called "ladders") at radii ranging from 2.7 cm to 10.5 cm. Each layer has an inner and outer sub-layer. For the four central barrels, layers 1 and 3 have double-sided double-metal (DSDM) silicon sensors with a spatial resolution of 50 μm for p-side strips, which run parallel to the beam direction, and 153.5 μm for n-side strips, which are at an angle of 90° to the p-side

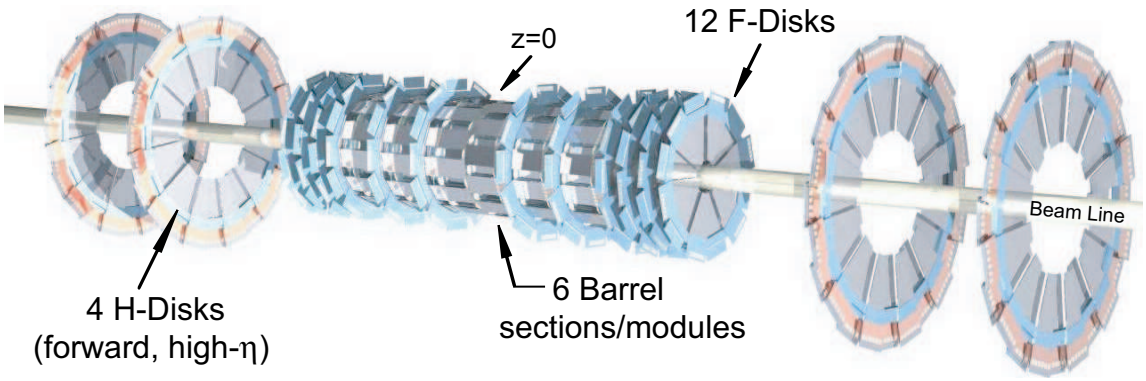

Figure 2.4: The Silicon Microstrip Tracker.

strips. Layers 2 and 4 have double-sided (DS) silicon sensors with a spatial resolution of 50 μm for the p-side strips (parallel to the beam), and 62.5 μm for the n-side strips (at an angle of 2° to the p-side strips). The two outer barrels have single-sided (SS) silicon sensors in layers 1 and 3 with a spatial resolution of 50 μm (p-side parallel to the beam) and double-sided silicon sensors in layers 2 and 4 with a spatial resolution of 50 μm for the p-side strips that are parallel to the beam, and 62.5 μm for the n-side strips, which are at an angle of 2° to the p-side strips. There is overlap between adjacent ladders for complete detection, as shown in Fig. 2.5. The SS and DS ladders have 6.0 cm long, 300 μm thick, rectangular silicon sensors mounted end-to-end. The DSDM ladders are 12.0 cm long. A typical ladder is shown in Fig. 2.6. The sensors are read out by SVX-II chips mounted on kapton high density interconnects (HDIs), which form part of the ladder. The ladders are

supported by bulkheads that also water-cool the ladders to an operating temperature of around 5-10° Celsius.

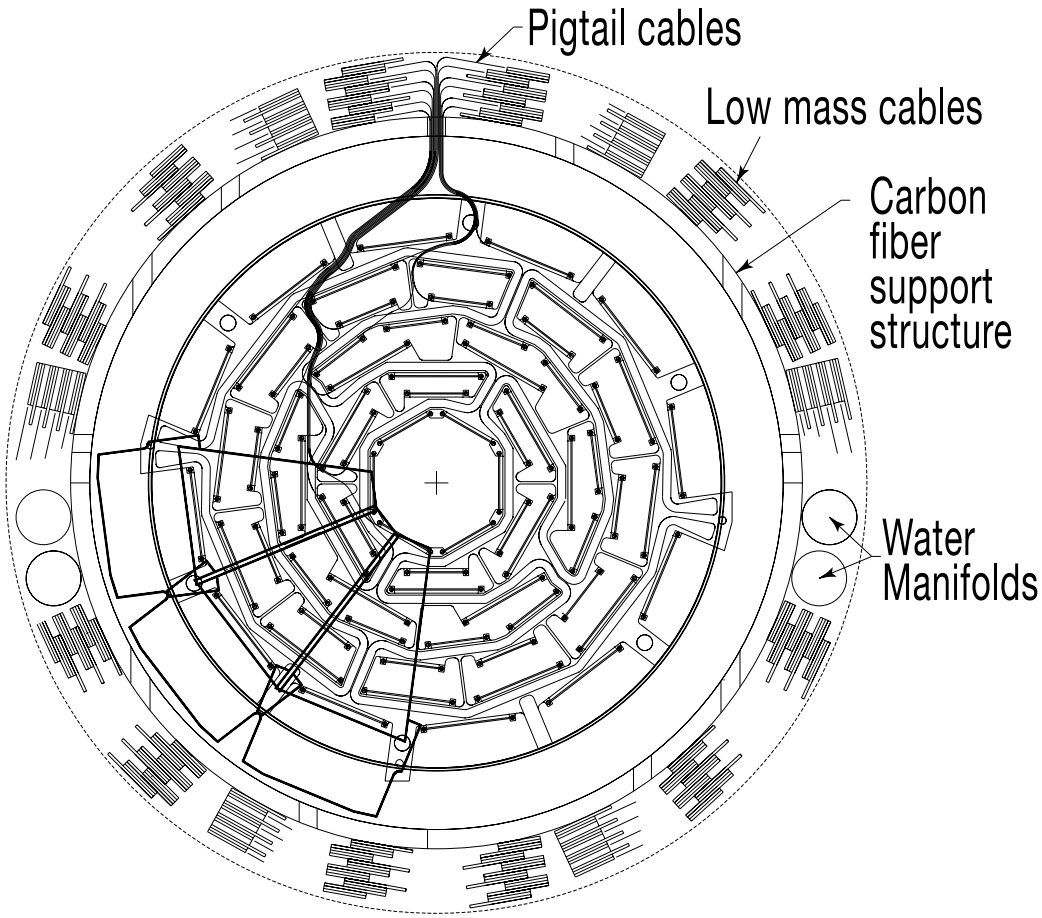

Figure 2.5: Cross section in the $x - y$ plane of an SMT barrel.

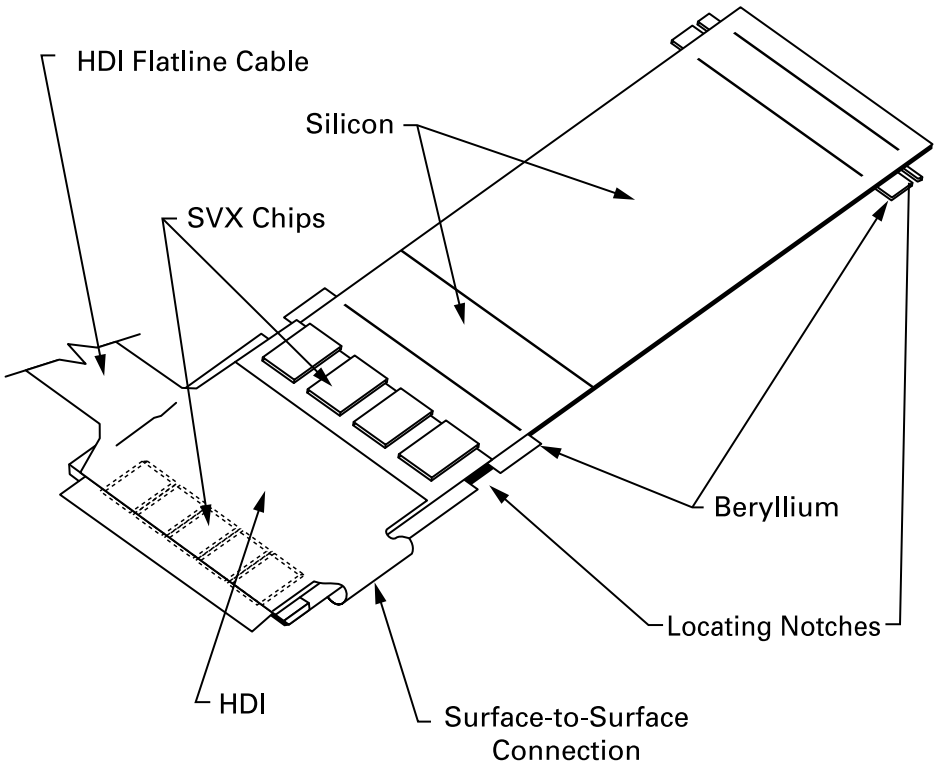

Figure 2.6: An SMT ladder.

There are 12 F-disks, six of which are interspersed between the barrels. The F-disks are constructed from 12 overlapping wedges. Each wedge is double-sided with a height of 7.5 cm. The readout strips are at a stereo angle of $+15^\circ$ on the p-side and -15° on the n-side. There are separate 8-chip HDI's to read out both sides of a wedge.

There are 4 H-disks that lie at $z = \pm 110$ cm and $z = \pm 120$ cm. The H-disk wedges are single-sided with a height of 14.86 cm. Twenty-four wedges make up one H-disk.

2.2.3 Central Fiber Tracker

The Central Fiber Tracker (CFT) [29] is the next closest subsystem to the beamline. The CFT extends the tracking capability, especially for low η ranges ($|\eta| < 2.0$). The CFT also has the use of the 2 Tesla superconducting solenoid magnet to help measure the momentum of charged particles. The CFT has a resolution on the order of 100 μm. It is also used for "Level 1" track triggering covering $|\eta| < 1.6$. The CFT, along with the rest of the tracking system, is shown in Fig. 2.7.

The CFT consists of 8 concentric support cylinders, which are covered by scintillating fibers, and extend from a radius of 20 to 52 cm. The two closest cylinders to the beamline are 1.66 m in length, and the six outer cylinders have a length of 2.52 m. There are a total of 76,800 scintillating fibers. Each cylinder has

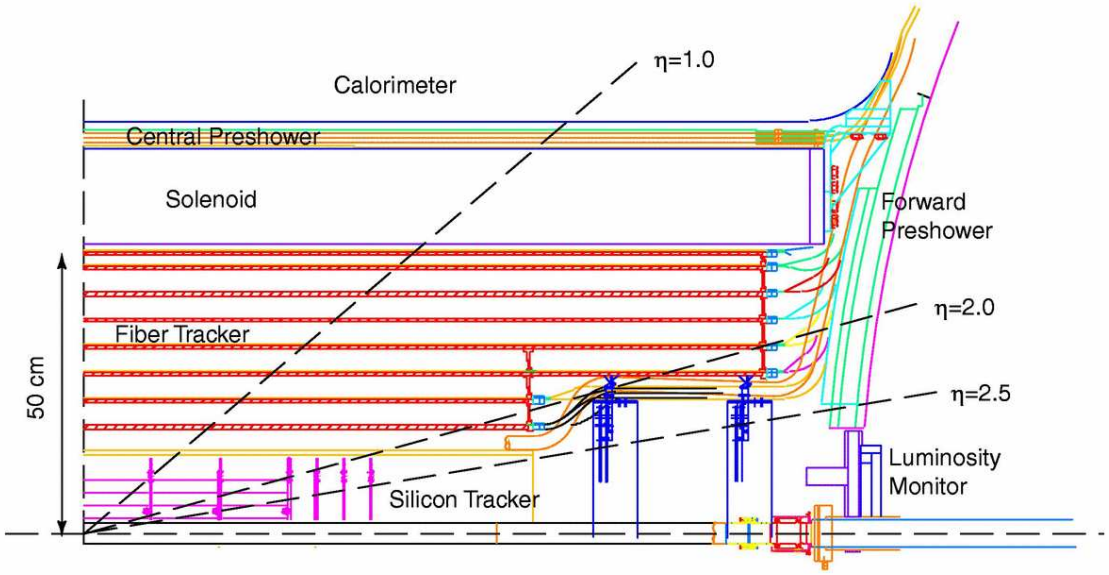

Figure 2.7: One quarter view of the DØ Tracking System.

a fiber doublet layer in the axial direction (i.e. parallel to the beam line), and an additional doublet layer in either the u or v stereo angle of approximately $+3°$ and $-3°$, respectively. The orientation from the innermost to outermost cylinder is $xu - xv - xu - xv - xu - xv - xu - xv$, where x is the axial doublet layer. Figure 2.8 shows the fiber doublet layer.

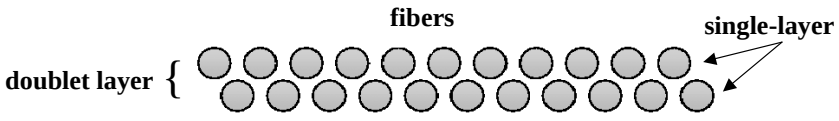

Figure 2.8: CFT fiber doublet layer.

The scintillating fibers are 835 μm in diameter and 166 cm long for the inner two cylinders and 252 cm long for the outer six cylinders. The inner two cylinders are shorter to accommodate the SMT's two H-disks on both ends. The scintillating fibers are grouped into ribbons that contain a total of 256 fibers or two layers of 128 fibers. The offset of the two layers of fiber is one-half of the fiber spacing. The scintillating fibers are connected through an optical connector to a clear fiber waveguide, which vary in length from 7.8 to 11.9 m. Light is collected from one end of the scintillating fiber; the "non-readout end" is mirrored with an aluminum coating, which provides a reflectivity of 85 to 90%. The waveguide transmits scintillation light to a Visible Light Photon Counter (VLPC), which converts the light into electrical pulses. The VLPCs are able to detect single photons and operate in a high background environment. The VLPC cassette is divided into 8 modules of 128 channels each, which will give 1024 individual pixels for light detection. The VLPCs require a liquid Helium cryosystem to operate at 9 K.

2.2.4 Central and Forward Preshower Detectors

The Central Preshower (CPS) [30] detector provides early energy sampling before the calorimeter and aids in an additional tracking measurement after the solenoid magnet. This will help to enhance electron and photon identification and to increase the rejection of fake electrons originating from jets. The CPS lies between the 2 Tesla solenoid magnet and the Central Calorimeter at a radius of 72

cm and covers the region -1.31 $< \eta <$ 1.31.

The CPS consists of a lead radiator closest to the solenoid magnet, followed by three layers of scintillating strips. The solenoid plus lead radiator equal a constant two radiation lengths. The triangular scintillating strips are arranged with the innermost layer in the axial direction followed by a u stereo angle of 23.774° and v stereo angle of 24.016°. The scintillation light is collected by wavelength-shifting (WLS) fibers and sent through clear fibers to photodetectors connected to VLPCs. Figure 2.9 shows the Central Preshower.

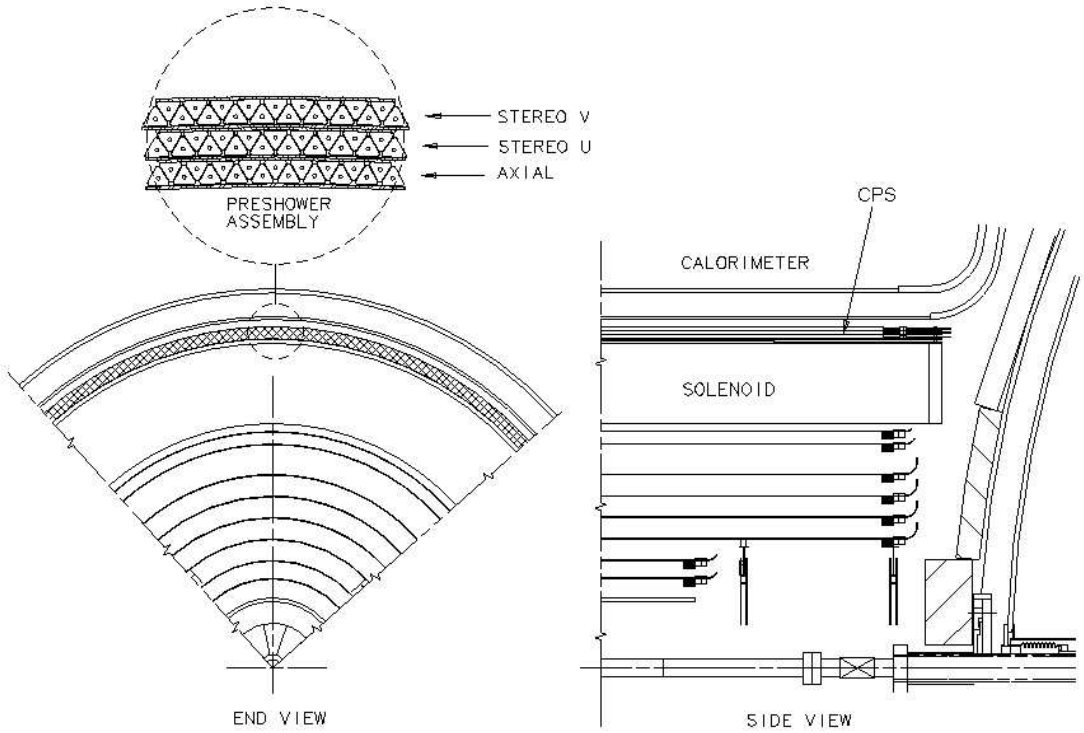

Figure 2.9: Cross-sectional end view (*left*) and side view (*right*) of the Central Preshower detector.

The Forward Preshower (FPS) [31] detectors are mounted on the inner head of the Endcap Calorimeters. The FPS consists of two scintillating layers with a tapered lead absorber of two radiation lengths sandwiched between them. The inner scintillator plane covers the region $1.65 < |\eta| < 2.5$, while the outer scintillator plane covers the range $1.5 < |\eta| < 2.5$. Figure 2.10 shows the Forward Preshower.

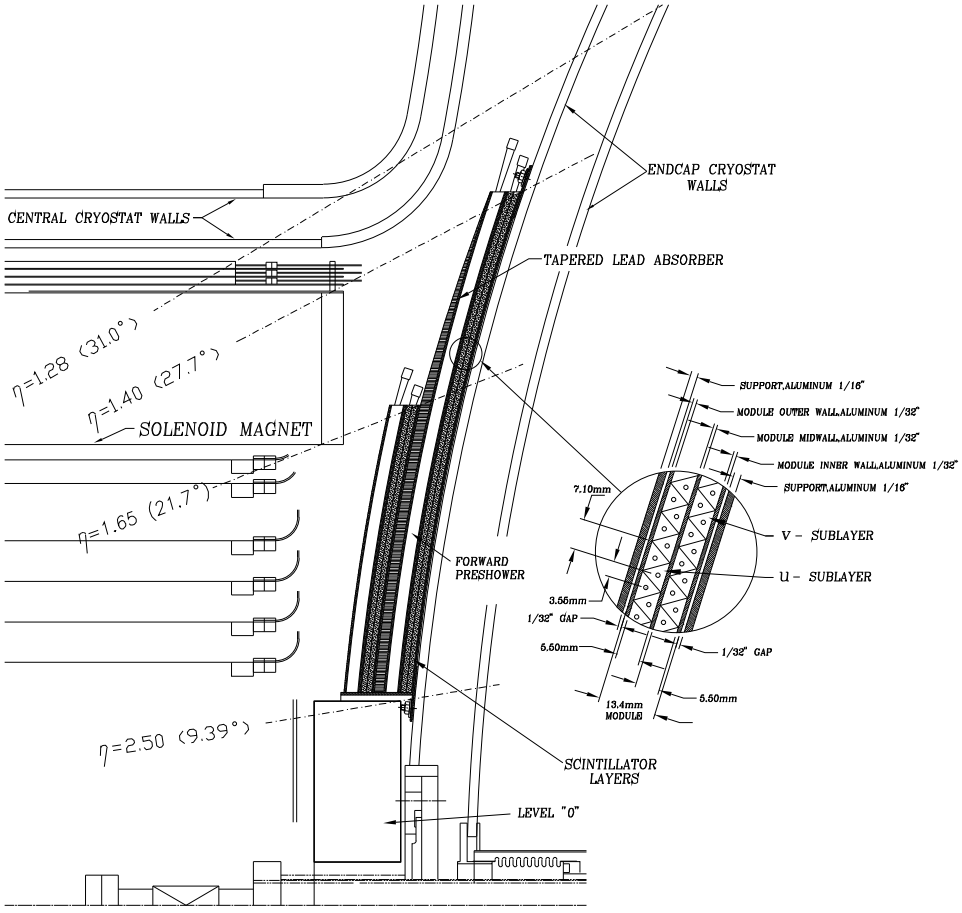

Figure 2.10: One quarter view of the Forward Preshower detector.

The FPS consists of 16 ϕ-wedges subtending 22.5°. Each wedge has a u and

v stereo layer, where the u strips are perpendicular to one radial edge, and the v strips are perpendicular to the other radial edge. The FPS has the layer orientation $u - v - l - u - v$, where l is the lead absorber. The FPS scintillation strips have the same geometry and connection to VLPCs, as the CPS strips.

2.2.5 The Calorimeter

The calorimeter [32] provides high-precision energy measurements of electrons, photons, and jets over a large η range. It is shown in Fig. 2.11. The calorimeter has three separate cryostats. A Central Calorimeter (CC) covers the range $|\eta| < 1.1$, and two Endcap Calorimeters (EC) that cover the range $1.4 < |\eta| < 5.2$. Each cryostat weighs about 300 metric tons and is filled with about 15,000 liters of liquid argon. The calorimeters are segmented into three different regions, an electromagnetic (EM) region closest to the tracking system to detect electrons and photons, followed by a fine hadronic (FH) region and coarse hadronic (CH) region to detect jets. The EM and FH sections use uranium absorber plates, while the CH section uses either copper absorber plates (CC) or steel absorber plates (EC). The EM absorber plates are 3 mm thick in the CC, and 4 mm thick in the EC. The FH absorber plates are 6 mm thick, while the CH copper absorber plates in the CC are 46.5 mm thick, and the CH steel absorber plates in the EC are 46.5 mm thick.

The absorber plates can initiate particle showers creating low energy

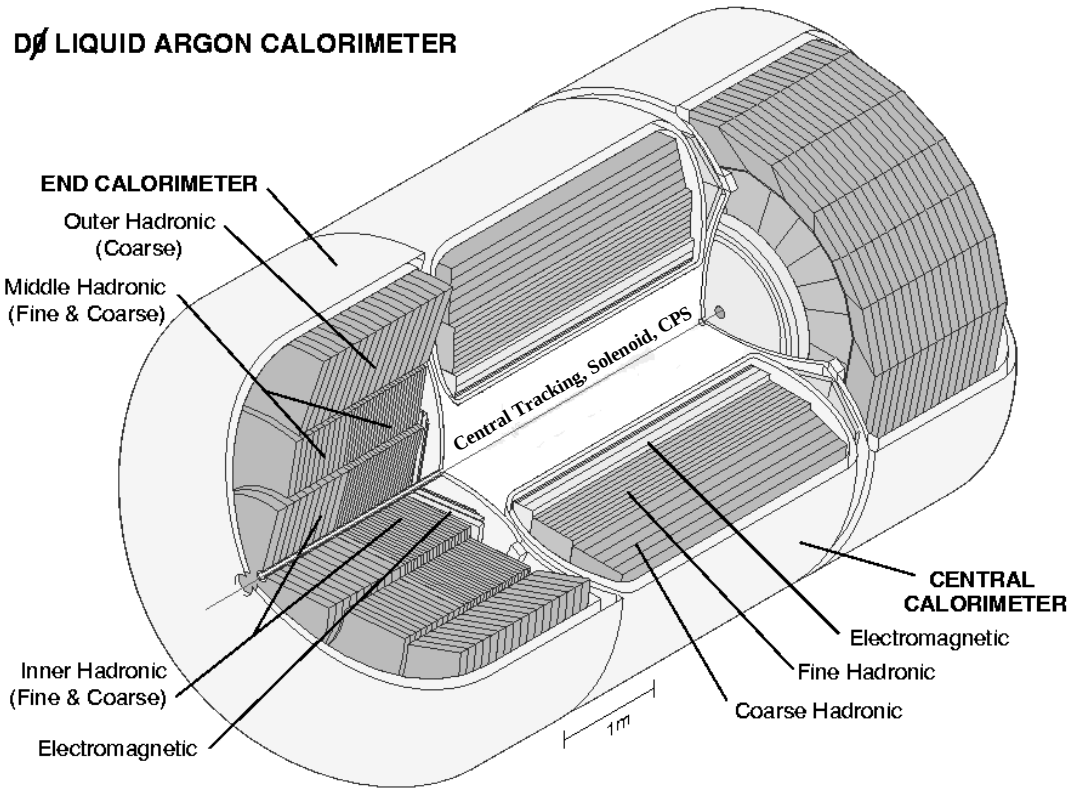

Figure 2.11: The DØ calorimeter.

secondary particles. The liquid argon is the active medium used to sample the ionization. It gives a measurement of the shower energy from the ionization of the charged secondary particles. The EM section of the calorimeter measures EM showers produced through bremsstrahlung ($e \rightarrow e\gamma$) and pair production ($\gamma \rightarrow e^+e^-$). These EM showers are well-contained in the EM part of the calorimeter. The hadronic sections of the calorimeter measure hadronic showers from high energy hadrons that interact with the uranium nuclei through the strong

nuclear force. These inelastic collisions will create many secondary hadronic particles. Hadronic showers cover a larger volume than electromagnetic showers.

The Central Calorimeter has the absorber plates parallel to the beam axis. The EM section has 32 modules subtending ≈ 0.2 radians in ϕ. The FH and CH sections have 16 modules. Each module is 250 cm in length. The modules consist of loosely stacked alternating absorber plates and readout boards in a stainless steel box structure. There are four layers in the EM section called EM1, EM2, EM3, and EM4. They have thickness of 2.0, 2.0, 6.8 and $9.8X_0$ respectively, where X_0 equals one radiation length. The readout cell segmentation for the EM1, EM2, and EM4 layers are 0.1×0.1 in $\Delta\eta \times \Delta\phi$. EM3 is located at the maximum EM shower region, and the cell segmentation is increased to 0.05×0.05 to enhance the position resolution of the EM shower centroid. The Fine Hadronic region has three layers (FH1, FH2, FH3) with thickness of 1.3, 1.0, and $0.76\lambda_A$, where λ_A equals one nuclear absorption length. The cell segmentation for the Fine Hadonic layers is 0.1×0.1. The Coarse Hadronic region has one layer (CH1) with an absorption length of $3.2\lambda_A$.

In the Endcap Calorimeters the absorber plates are perpendicular to the beam axis. The EM section has one module that covers $1.4 < |\eta| < 4.1$. The EM section in the EC has four layers (EM1, EM2, EM3, EM4) with radiation lengths 0.3, 2.6, 7.9, and 9.3. The cell segmentation in the EM module changes with η. The segmentation is the same as the Central Calorimeter for $|\eta| \leq 2.6$. In the range

$2.6 < |\eta| < 3.2$ the segmentation in the third layer reduces to 0.1×0.1. The segmentation in all layers is 0.2×0.2 for $3.2 < |\eta| < 4.0$. For $|\eta| \geq 4.0$ the segmentation is 0.4×0.4. Directly behind the EM module is an Inner Hadronic (IH) module with four fine hadronic sections and one coarse hadronic section. The fine hadronic sections are 17.6 absorption lengths and are made of uranium absorption plates. The coarse hadronic section is 4.1 absorption lengths and are made of stainless steel absorption plates. The IH covers the region $1.6 < |\eta| < 5.2$. The Inner Hadronic module is surrounded by two concentric rings of modules. The Middle Hadronic (MH) ring has four FH sections and one CH section. Each FH section is 0.9 absorption lengths and is made of uranium absorption plates. The CH section is 4.4 absorption lengths and is made of stainless steel absorption plates. The Outer Hadronic (OH) ring only uses a CH section. It uses stainless steel absorption plates, which are at an angle of about 60° relative to the beam.

A tower consists of a set of cells from many layers in the direction outward from the interaction point. A readout cell contains many adjacent unit cells. The transverse readout cell dimensions were chosen to be similar to shower sizes: $\approx 1 - 2$ cm for EM showers and ≈ 10 cm for hadronic showers. A unit cell consists of an absorber plate, signal board, and the gap between two absorber plates, as shown in Fig. 2.12. The gap between a signal board and an absorber plate is 2.3 mm. The signal boards are constructed of two layers of 0.5 mm G-10 coated with high resistivity carbon loaded epoxy and a copper pad, on which signals are

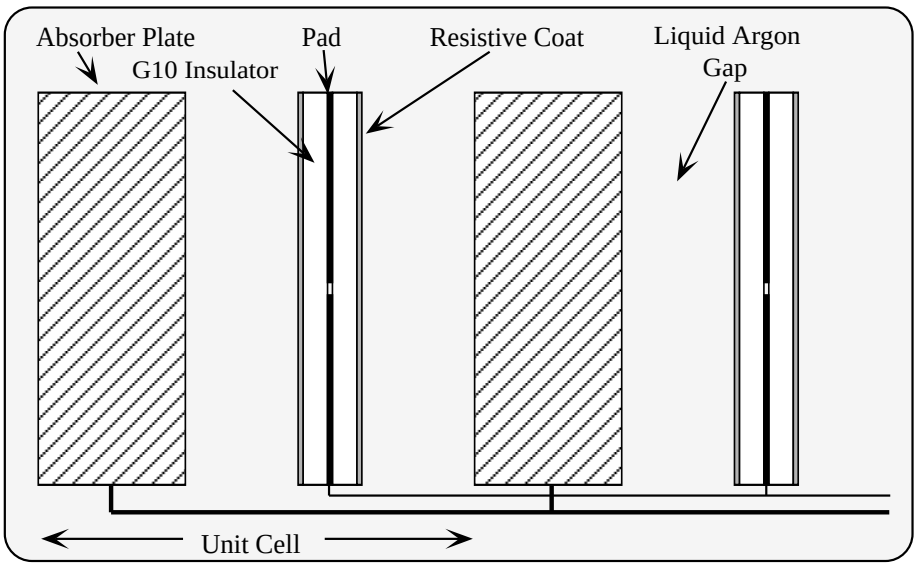

Figure 2.12: A calorimeter unit cell.

capacitively induced by charge drifting across the gap. An electric field is created by grounding the absorber plate and applying a positive high voltage (2-2.5 kV) to the resistive coat. Electrons from the ionization of the liquid argon are collected by the electrode. The electron drift time across the gap is approximately 450 ns. The charge collected on the resistive coat induces a charge on the copper pad. The analog signal is sent from the readout pad and carried to the exterior of the calorimeter via 30 Ω coaxial cables to preamplifiers, where signal shapers sample the signal voltage prior to and 2.2 μs after the $p\bar{p}$ collision. The baseline is subtracted from the peak voltage to obtain the final analog signal. The signal is digitized by Analog-to-Digital Converters, which have 12-bit resolution and 15-bit

dynamic range. The total physically connected readout channels for all three cryostats is 47,032.

2.2.6 The Inter Cryostat Detector

The Inter Cryostat Detector (ICD) [33] helps to measure the energy of jets and missing transverse energy. As shown in Fig. 2.3, it covers the region 1.1 $< |\eta| <$ 1.4, where there is a large amount of uninstrumented material (cryostat walls, support structures, cabling). The ICD uses 384 scintillation tiles of size 0.1 x 0.1 in $\Delta\eta$ x $\Delta\phi$ to make 16 tile modules, which are mounted on the inner face of the EC cryostat walls, shown in Fig. 2.13. There are wavelength shifting (WLS) fibers in the grooves of each tile to convert the scintillation light in the tile to a wavelength less likely absorbed in the subsequent light path. Clear fiber ribbon cables are used to bring the light signals from the ICD tile's module connector to the readout crates, which contain phototubes and readout electronics.

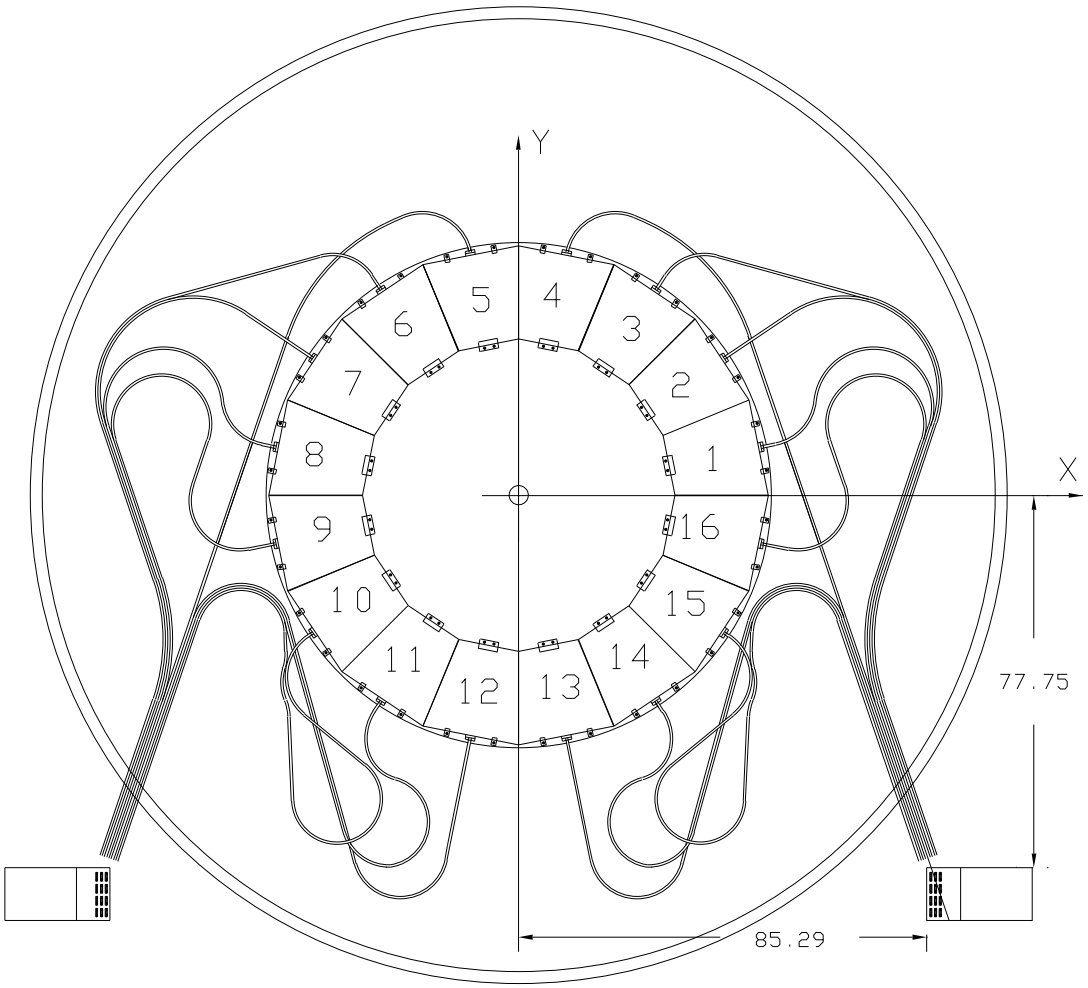

Figure 2.13: The ICD tile module orientation.

2.2.7 The Muon Detector

The Muon detector has three major components: the Central Muon system; the Forward Muon System; and a 2 Tesla toroid magnet located between the first and second layers. The toroid magnet is used to make an independent measurement of the muon momentum. It is 109 cm thick and weighs 1973 metric tons. The full muon detector is shown in Fig. 2.2, while Fig. 2.14 shows the muon detector scintillator sections, and Fig. 2.15 shows the muon detector drift tube sections.

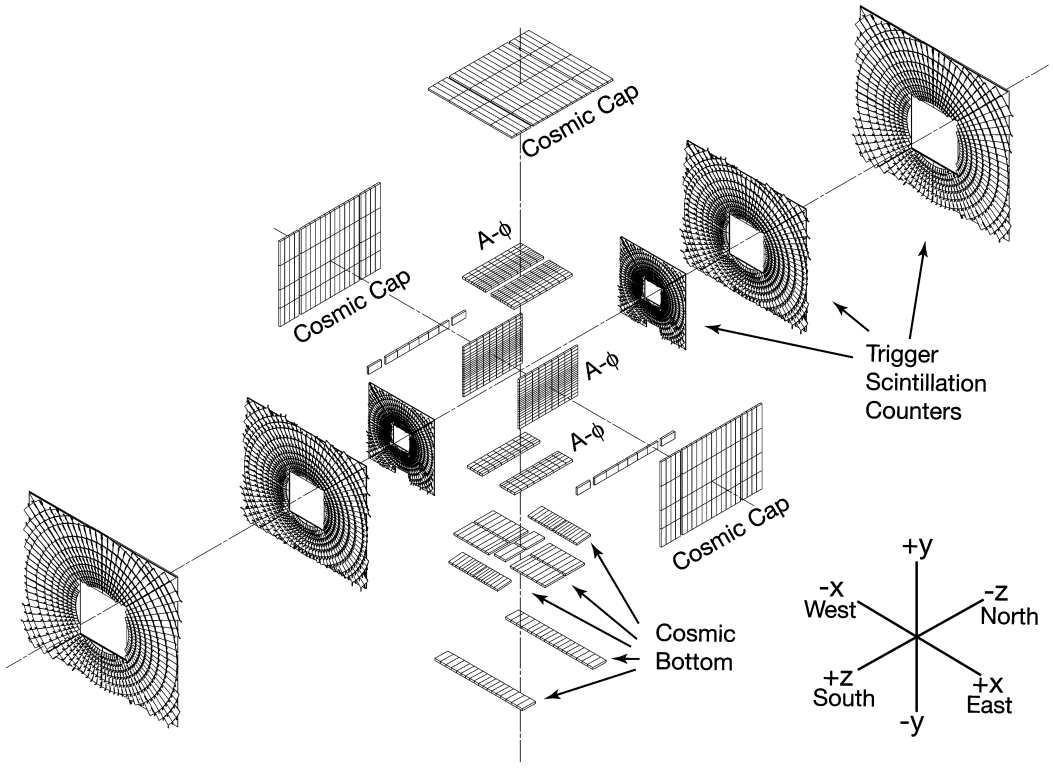

Figure 2.14: The Muon detector scintillation segments.

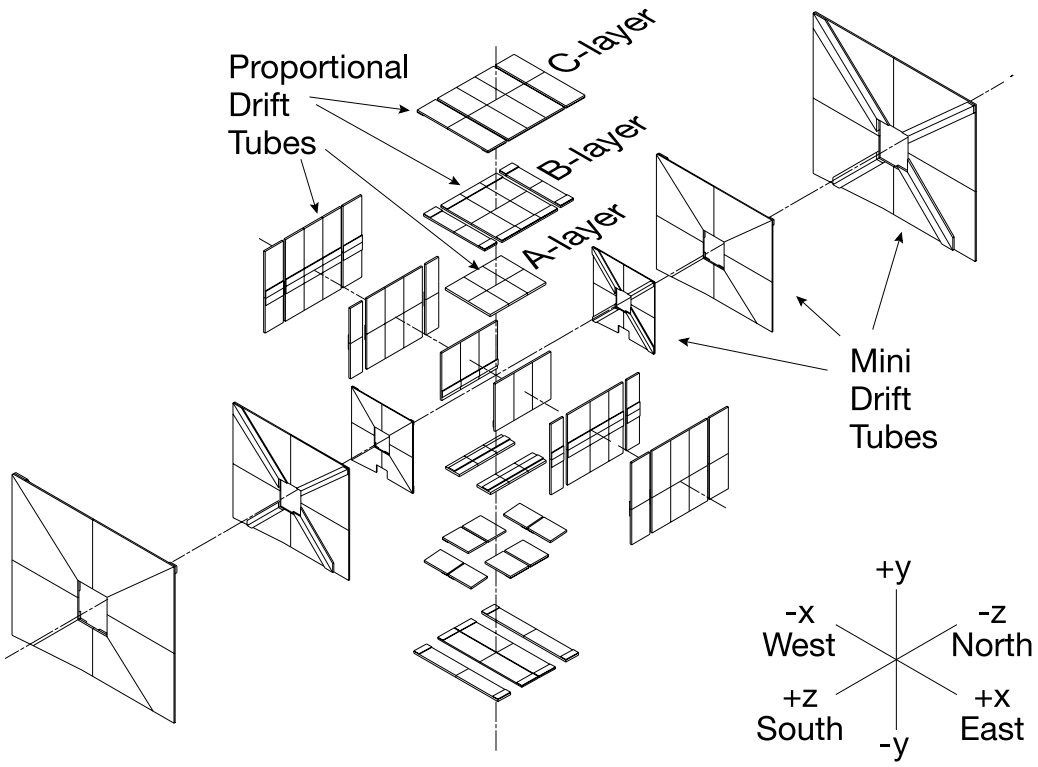

Figure 2.15: The Muon detector drift tube segments.

The central muon detector [34] consists of three detector systems: the Wide Angle MUon Spectrometer (WAMUS) drift chambers; the Cosmic Cap and Bottom scintillation counters; and the $A\phi$ scintillation counters. It covers a range of $|\eta| < 1$. The WAMUS has three layers of drift chambers. One layer is inside the toroid (A-layer) and the other two are outside (B-, and C-layers respectively). About 55% of the central region is covered by three layers of PDT's, and close to 90% has at least two layers. The A-layer PDT's have four decks of drift cells, while the B- and

C-layer PDT's have three decks. There are approximately 24 columns of cells per PDT. Each drift cell has an anode wire at its center that runs along the length of the cell, which is oriented along the magnetic field lines. The drift cells are filled with a non-flammable gas mixture of 84% argon, 8% methane and 8% CF_4. The hit uncertainty due to diffusion is about 375 μm. The momentum resolution of the PDT's is around 30% for muons with $p_T = 100$ GeV/c, but if central tracking is included the resolution is around 15%. The Cosmic Cap scintillation counters cover the top and sides of the WAMUS C layer. They use a fast trigger to identify muons from cosmic rays. This works with the WAMUS trigger to trigger a muon event if the muon registered a hit in the scintillation counters within 50 ns of the expected time-of-arrival from a beam muon. The scintillation counters have a time resolution of about 5 ns, which can be improved by offline corrections to 2.5 ns. The Cosmic Cap also provides a time stamp for muons which pass through the WAMUS PDT's to determine which beam crossing the muons came from. The Cosmic Cap has 240 scintillation counters. The Cosmic Bottom scintillation counters are used with the bottom B- and C-layers. These have the same purpose as the Cosmic Cap. The Cosmic Bottom uses 132 counters read out by two PMTs. The difference between the Cosmic Cap and the Cosmic Bottom is that the bottom counters have the narrow dimension along phi and the long dimension along eta. The $A\phi$ scintillation counters cover the WAMUS PDT's between the calorimeter and toroid magnet. These counters provide a fast muon trigger and reject out-of-time backscatters from

the forward direction. The counters have a time resolution of less than 4 ns, which can be improved by offline corrections to 2 ns. The $A\phi$ counters provide a time stamp for the muons that pass through the WAMUS PDT's, which is important for low-p_T muons that do not penetrate the Cosmic Cap or Bottom counters. The scintillation counters overlap in ϕ to improve the efficiency from muons which escape through the cracks.

The Forward Angle MUon System (FAMUS) [35] consists of 3 layers of Mini-drift Tubes (MDTs) and scintillation counters, and shielding around the beam pipe from the calorimeter to the accelerator tunnel. The shielding reduces trigger rates, fake track reconstruction, and aging of detectors. The forward muon system covers the range $1.0 < |\eta| < 2.0$. The FAMUS has a similar layer structure as the WAMUS. Each drift cell is filled with a gas mixture of 90% CF_4 and 10% CH_4. The coordinate resolution is around 0.7 mm/deck, and momentum resolution is about 20% for low momentum tracks. There are 4 planes of tubes in the A-layer, and 3 planes of tubes in the B- and C-layers. Each layer is divided into 8 octants, where the tubes are different lengths oriented along magnetic field lines. The MDT planes are supported by aluminum bars and covered with aluminum sheets, which reduces noise and the probability of track formation from low energy electrons. The A-layer is cut in the bottom octants to provide calorimeter supports. The B and C bottom octants are shorter because of the collision hall floor. The FAMUS trigger scintillation counters are mounted on the inner face of each MDT layer and are

arranged in $r - \phi$ geometry to match the CFT trigger segmentation. The muon trigger will combine the muon system information with the CFT track information. Each plane of counters is divided into 8 octants with 96 counters per octant. The phi segmentation is 4.5°, the same as in the CFT.

2.2.8 The Trigger and Data Acquisition Systems

The trigger system helps to select physics events of interest out of the millions of events possible. It uses a combination of hardware and software to quickly determine an interesting event from the large background due to inclusive inelastic collisions. Triggers are based on the characteristics of a physics event or the theoretical understanding of new physics. The DØ trigger system uses four levels of discrimination (L0, L1, L2, and L3). Each progressive level requires tighter selection criteria and decreased output rate.

The L0 trigger [36] is used to make an accurate luminosity measurement from non-diffractive inelastic collisions. The L0 detector has two arrays of twenty-four plastic scintillation counters, which are on the inside face of the Endcap Calorimeters and cover the range $2.7 < |\eta| < 4.4$. The L0 trigger can also be used to determine the z position of the event vertex by calculating the difference in arrival time for particles hitting the two L0 detectors. This information can then be used by the other trigger levels.

The L1 trigger system [37] is a hardware system, which filters the 2.52 MHz

beam crossing rate. It takes detector specific information from each sub-detector as AND-OR input terms. There are 256 AND-OR input terms available. The Level 1 trigger framework uses this input to determine if the event should be rejected or kept for further analysis in the Level 2 trigger system. The L1 trigger has an output rate of 1.6 kHz. The L1 trigger decision is not made between beam crossings, but instead the trigger framework generates input terms used between L1 decisions to retain data from up to 32 beam crossing. Level 1 can perform decisions while level 2 is making a decision. There are 128 separate sets of AND-OR term combinations evaluated every beam crossing. This in turn produces 128 separate L1 specific trigger decisions, which are ORed for the global L1 trigger decision. A specific trigger can be prescaled to get the required output rate of 1.6 kHz.

The L2 trigger system [38] is similar to the L1 system in that it consists of hardware framework and a separate set of processors. The L2 trigger reduces the L1 rate of 10 kHz to 1 kHz within 100 μs using correlations between the sub-detectors. Figure 2.16 shows the Level 1 and Level 2 data flow. The L2 Global Processor makes its decision based on information from the preprocessors. It may also impose stricter requirements for each L1 trigger bit which fired. The L1 trigger bits, whether accepted or rejected, are sent to a 128-bit L2 trigger bit mask. If any of the L2 bits pass, then the event will pass L2 and the decision is sent to the L2 hardware framework. The Global Processor receives preprocessor information at 320 Mbytes/s and makes trigger decisions within 75 μs.

The L3 trigger system [39] is a software system, which reduces the L2 rate of 1 kHz to 50 Hz within 100 ms using 82 Linux PC's. If there is a L2 accept, information from the various sub-detector readout crates is sent to L3. The Level 3 system will partially reconstruct the data from each event. Each event is examined by a processor with L3 filtering software [40]. Each filtering tool identifies a certain physics object or event topology. If the L3 event passes the filters, it will be written to tape for offline analysis. Figure 2.17 shows how the L3 trigger accepts input from earlier trigger stages and transfers to offline storage.

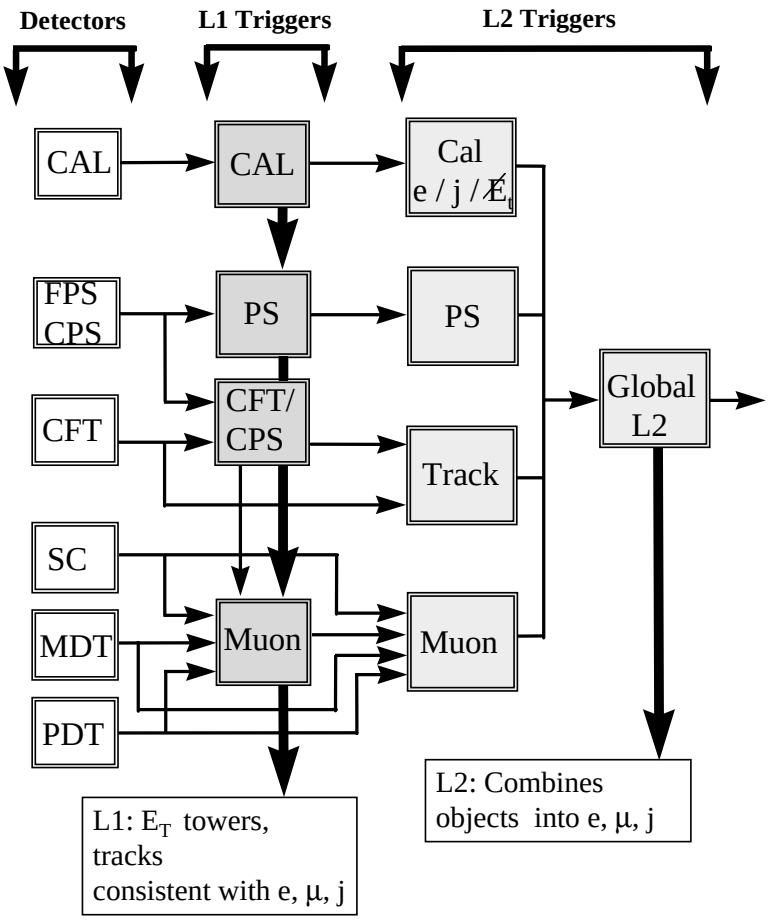

Figure 2.16: L1 and L2 data flow.

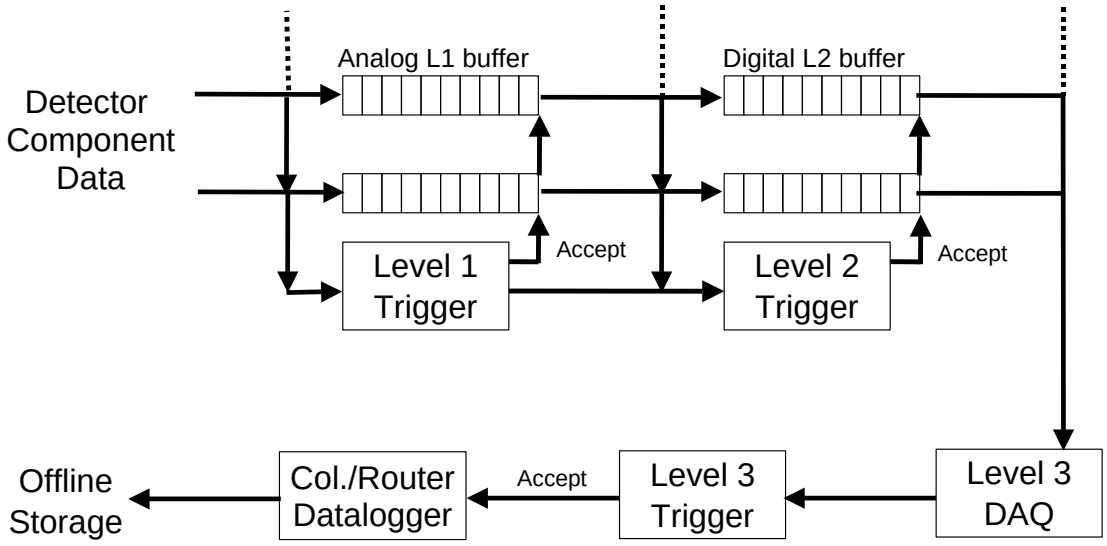

Figure 2.17: L3 data flow.

Chapter 3

Offline Event Reconstruction

In a physics event that passes trigger requirements, digitized signals (pulse heights, widths, and times) from the detector are saved on computer storage tapes for future use. This raw data can then be transformed into physical objects, like tracks and calorimeter clusters, using a C++ reconstruction program called "RECO." When the RECO software reads in a data event, it will unpack all the sub-detector digitized signals in the raw data chunk. It will then reconstruct parts of the detector to interpret hit signals where a particle had transversed. This will then be used to reconstruct particle tracks and find vertices. The reconstruction program also creates objects for particle identification, such as calorimeter clusters, electromagnetic particles, muons, jets, taus, and missing transverse energy.

3.1 Track Reconstruction

The SMT and CFT detector electronics will determine the arrival time and drift time of a pulse created by a charged particle crossing that part of the detector section, which places the location of a "hit" on that detector surface. Track finding consists of searching specific paths. Four detector regions are used to propagate these roads: central (full CFT extended into the SMT), forward (forward SMT with three F-disks), overlap (partial CFT extended into the SMT), gap (between overlap and forward). The hits on the many detector surfaces are used to calculate the best estimate for a track using the Kalman Algorithm [41] and DØ interacting propagator [42]. Starting from an initial guess, one propagates the track parameters and error matrix to the next hit surface using the interacting propagator, which propagates tracks with errors and includes detector material effects (multiple scattering and energy loss). Once the track is propagated to the next surface, a prediction of track quality is made (incremental χ^2 cut) that can be used for pattern recognition to narrow the selection of candidate hits at the new surface. The track parameters and errors will change as the track is propagated, and a final measurement of the track parameters and error matrix is made when the propagator has extended to its last hit surface. Then the Kalman fit algorithm is used calculate a minimized χ^2. A track is kept and considered good, if the match χ^2 value is less than 100, which determines the match quality to the track. Once a

track candidate is formed, the track parameters are re-estimated at each surface by starting from the outermost hit and propagating inward. This will give the optimal estimate of track parameters and is called "Kalman smoothing." An optimal estimate of the track parameters at some interior surface can be calculated by doing complimentary unidirectional Kalman fits from outermost track hits and propagating in to the interior surface, where the two track segments that were propagated in to form a single track are then combined.

3.2 Vertex Finding

Vertices are classified into two groups: primary and secondary. The primary vertex comes from the hard $p\bar{p}$ interaction point and has the highest p_T tracks and largest number of tracks associated with it. The secondary vertices are displaced from the primary vertex due to long-lived hadron decays.

To select a primary vertex candidate [43], global tracks are selected based on their distance of closest approach to the nominal vertex in the transverse plane. Then these tracks are fit to a common vertex and the χ^2 contribution of each track is calculated. If the vertex χ^2 is greater than 10, the track with the highest χ^2 contribution is removed, and the primary vertex candidate is re-fit. Then all tracks within $x, y = 0.15$ cm and $z = 0.5$ cm around a selected vertex are used to calculate the minimum bias vertex probability [44]. This probability is based on the expected

distributions of transverse momentum of tracks from minimum bias interactions and hard scattering interactions. The hard scattering interaction vertex will have higher p_T tracks than a vertex from a minimum bias interaction. The selected vertex with the smallest minimum bias probability is defined as the primary vertex.

Secondary vertices are found by combining two tracks that are displaced from and do not point to the primary vertex, and fitting the vertex with a method similar to the primary vertex fit. Then another track is added to the secondary vertex and the vertex is re-fit. If the track-to-vertex χ^2 value is too large, the track is removed. This procedure is repeated for all tracks close to this secondary vertex. There can be multiple secondary vertices in an event.

3.3 Calorimeter Clustering Algorithm

Clusters of cells in the calorimeters are built starting from cells with energy deposition above a threshold of 4σ (signal cells). Cells that are neighbors of these signal cells are kept if they are above a threshold of 2.5σ, and rejected otherwise. The algorithm [45] has good efficiency for retaining signal clusters while rejecting noise.

3.3.1 Cone Algorithm

Jets, electrons, and photons are reconstructed using the cone algorithm. Energy deposition in a cell is represented by a massless four-vector [46] that points along the cell's direction from the center of the detector. The cone algorithm starts by selecting *seeds*, which are highest E_T calorimeter towers in the event above a certain threshold. The cone space is defined by

$$\Delta R = \sqrt{(\Delta\eta_{det})^2 + (\Delta\phi_{det})^2}, \tag{3.1}$$

where $\Delta\eta_{det}$ ($\Delta\phi_{det}$) is the difference in pseudorapidity (azimuthal angle) between a tower and the seed tower. The 4-vectors of towers within a fixed cone size are added to the seed four-vector. The cells within a cone are then removed from consideration, and a new seed is formed from the remaining highest-E_T tower. The centroid of the cone is calculated from contributions from all the particles within the cone.

3.4 Electron and Photon Reconstruction

Electromagnetic particles (electrons positrons, and photons) are reconstructed using the energy from the four EM layers and the first hadronic layer of the calorimeter, which will define an EM tower. The cone algorithm is used to

form EM clusters. Preclusters are created from the highest E_T EM towers. Then adjacent towers are added to a precluster, if they are above 50 MeV and within a precluster window in ΔR space. For the Central Calorimeter, the window is 0.3 $\times$ 0.3 ($\Delta\eta \times \Delta\phi$). The adjacent tower must have a cone radius of 10 cm in the third EM layer for Endcap Calorimeter preclusters. All adjacent EM towers forming a cluster must be within a cone radius of $\Delta R = 0.4$. These clusters are then considered EM candidates, if they pass the following criteria: $E_T > 1.5$ GeV; EM fraction > 0.9; and shower isolation < 0.2. EM fraction is defined as the fraction of cluster energy measured in the EM layer of the calorimeter divided by the total cluster energy (hadronic + EM). The shower isolation is defined by:

$$f_{iso} = \frac{E_{total}(0.4) - E_{EM}(0.2)}{E_{EM}(0.2)}, \tag{3.2}$$

where $E_{total}(0.4)$ is the total cluster energy (in all layers, except CH) in a cone of radius 0.4 and $E_{EM}(0.2)$ is the total electromagnetic cluster energy in a cone of radius 0.2. To differentiate between electrons and photons, we look for nearby tracks that are matched to the EM cluster. A loose road method is used to search for tracks within 0.05 $\times$ 0.05 ($\Delta\eta \times \Delta\phi$) between the calorimeter cluster and the primary vertex. The tracks are required to have a minimum transverse momentum of 1.5 GeV. If at least one track is found in this region, the cluster is labeled as an electron (positron) and assigned an *id* of 11 (-11) according to the particle charge,

as determined from the track curvature. If no tracks are found in the road, the cluster is labeled as a photon ($id = 10$).

3.5 Muon Reconstruction

Muons are reconstructed using either the muon detector and toroid only ("local") or the muon detector, toroid, plus the tracking detectors ("central track-matched"). To be considered a muon, the charged particle must have a minimum $p_T > 1.5$ GeV. The muon quality is determined by how many hits the muon has associated with it in each layer of the muon system.

3.6 Jet Reconstruction

Jets are reconstructed from calorimeter information using the cone algorithm. Towers of size $\Delta\eta \times \Delta\phi = 0.1 \times 0.1$ that have an energy above 1 GeV or more are used as seeds in preclusters. Preclusters are formed by combining adjacent calorimeter towers within a radius of 0.3 to the seed towers. Jet clusters are defined by preclusters in a cone size $\Delta R = 0.5$ or 0.7 around the jet centroid. Jets with $E_T < 8$ GeV are thrown away. If two jets share the same tower, a split/merge fraction is calculated, which is the ratio of the shared energy of the jets to the energy of the least energetic jet. If the ratio is larger than a 50%, the jets are merged and a new centroid is calculated. Otherwise, the shared towers are split

between the jets.

3.7 Missing Transverse Energy

For neutral charged particles that do not interact with the detector (e.g. neutrinos), there will be an overall momentum imbalance in the event, which is called Missing Transverse Energy ($\not\!\!E_T$). The missing E_T is calculated by first determining the x and y components of the visible energy, E^{vis}, in the calorimeter.

$$E^{vis}_{x,y} = \sum_{cells} E^{x,y}_i \tag{3.3}$$

Then the x and y components of the missing transverse energy are $\not\!\!E_{Tx} = -E^{vis}_x$ and $\not\!\!E_{Ty} = -E^{vis}_y$. The total missing E_T is given by $\not\!\!E_T = \sqrt{(\not\!\!E_{Tx})^2 + (\not\!\!E_{Ty})^2}$.

After calculating the missing E_T from the calorimeter cell-level energies, the missing E_T is corrected to account for electron energy scale corrections. Energy corrections are applied to electrons satisfying $E_T > 5$ GeV, EM fraction > 0.9, and isolation > 0.1, and the missing E_T is corrected accordingly. We do not apply corrections for jets or muons, since the Drell-Yan events contain only the soft hadronic recoil from Z, and no high-p_T muons.

3.8 Post-RECO Corrections

After the standard event reconstruction process, further corrections are applied to jets and to the missing transverse energy. Also, events recorded during periods in which there were problems with some detector subsystems or with the data acquisition system are discarded.

3.8.1 d0correct

The software package d0correct is used to apply the proper jet and missing transverse energy corrections. It performs the following tasks:

1. Create a list of good muon candidates ("medium muons"). These are muon candidates passing a set of standard muon identification requirements.

2. Create a list of good EM clusters. Good EM clusters must pass the following cuts:

   - $p_T > 5.0$
   - $|\eta_{det}| < 2.5$
   - EM Fraction > 0.9
   - Isolation < 0.15
   - HMx8 < 10000, where HMx8 is a covariance matrix of 8 observables to take into account simultaneously both the energy observed in a given

layer and its correlations with energy deposited in the other layers.

3. Create a list of good jets. Good jets must pass the following identification requirements:

   - $0.05 <$ Jet EM Fraction < 0.95
   - Jet Course Hadronic Fraction (CHF) < 0.4, where CHF is the fraction of transverse energy of the jet in the CH layers of the calorimeter.
   - Jet Hot Cell Fraction < 1000. The jet hot fraction is the ratio of transverse energy in the most energetic tower to that in the next leading tower in the jet.
   - Jet N90 > 1, where N90 is the number of towers in a jet that contain 90% of the jet energy.
   - Jet F90 < 0.5 or Jet CHF < 0.15, where F90 = N90/(total number of towers in a jet). This requirement, together with the previous one, suppress fake jets due to noisy cells.
   - L1 confirmation > 0.4 (in CC, EC), where L1 confirmation = L1SET/($E_T^{jet}\times(1 -$ CHF)), and L1SET is the sum of L1 tower transverse energies for that jet.
   - L1 confirmation > 0.2 (in ICR $= 0.8 < |\eta| < 1.5$)

4. Remove jets matching EM clusters. These are highly electromagnetic jets

that also appear in the list of EM clusters.

5. Perform jet energy scale corrections [47]. Corrections are made for the effects of calorimeter noise, non-uniform energy response, out-of-cone energy deposition and muons within the jet cone.

6. Correct missing E_T. Loop over good muons, good EM clusters, and good jets to get corrected missing E_T from them. For this analysis, we have used the definition of missing E_T defined in Section 3.7.

3.8.2 Jet Energy Scale

The measured jet energy from the calorimeter is not equal to the true energy of the parton that initiated the hadron shower. Effects of calorimeter noise, non-uniform energy response, and out-of-cone energy deposition can cause an inaccurate measurement. A Jet Energy Scale (JES) correction [47] is applied to the measured jet energy to correct back to parton-level jet energies. The true jet energy, E_{jet}^{true}, measured with a cone algorithm of radius $\mathcal{R}$, is calculated using the measured jet energy E_{jet}^{meas} by

$$E_{jet}^{true} = \frac{E_{jet}^{meas} - E_O(\mathcal{R}, \eta, \mathcal{L})}{R_{jet}(\mathcal{R}, \eta, E)S(\mathcal{R}, \eta, E)}, \tag{3.4}$$

where

- $E_O(\mathcal{R}, \eta, \mathcal{L})$ is an offset term for non-diffractive events to account for detector noise, and energy deposition from the underlying event (i.e. spectator quarks and gluons), from previous $p\bar{p}$ crossings, and from additional $p\bar{p}$ interactions. Since the number of additional interactions depends on the luminosity, the offset term is a function of luminosity $\mathcal{L}$. The offset increases as the cone size $\mathcal{R}$ increases.

- $R_{jet}(\mathcal{R}, \eta_{det}, E_{jet})$ defines the energy response of the calorimeter for jets. This depends on the cone size $\mathcal{R}$ because the cone size determines how much of energy from the calorimeter cluster is included in the measurement.

- $S(\mathcal{R}, \eta, E)$ is the fraction of the jet energy inside the jet cone.

3.8.3 wz_analyze

After data events have been reconstructed with RECO and corrected for using d0correct, a software package called wz_analyze is used to analyze the events. It creates a storage array called a "ROOT-tuple," which reads over the RECO output and makes physics quantities that are useful for analysis. The program also removes runs that have known problems with detector sub-systems or the data acquisition system.

Chapter 4

Signal Event Simulation

In order to model detector acceptances, efficiencies, and background contributions, computer simulations are used. The simulations must be compared to data to ensure that the data is correctly modeled. Monte Carlo events are generated based on standard model calculations and are processed through detector simulation programs which model the DØ detector response.

4.1 Monte Carlo Event Generator

The Monte Carlo Drell-Yan events are generated using PYTHIA (version 6.202) and PHOTOS (version 2.0) with the CTEQ6M [48] parton distribution functions (PDFs). PYTHIA [49] is a physics simulation program that generates high-energy physics events. Based on theoretical calculations, it provides models

for a number of the physics aspects of the interactions, including hard and soft interactions, parton distributions, initial and final state parton showers, multiple interactions, fragmentation and decay. The Monte Carlo program PHOTOS [50] is used to model final state QED radiation.

4.2 Detector Simulation

After physics events are generated, they are passed through a detector simulation program to model detector effects. There are two detector simulation packages that are used at DØ: a full detector simulation and a fast Monte Carlo.

4.2.1 Full Detector Simulation

The full detector simulation tool, based on GEANT [51], describes the passage of particles through a variety of materials of different shapes and sizes, and is used to study the responses from particle interactions using realistic detector effects. The two packages used for the full detector simulation used at DØ are DØgstar and DØsim. DØGEANT Simulation of the Total Appartus Response (DØgstar) simulates the amount of energy deposition in the active region of the DØ detector. It generates detector "hits" similar to real data collisions in the detector. The DØsim program takes the output from the DØgstar program and does digitization for each sub-detector. It models calorimeter pileup from previous

events, overlapping minimum bias events, detector noise, and detector inefficiencies. The output of DØsim is then similar in format to real data output and can be used for input into the reconstruction program.

The full detector simulation uses a large amount of computing resources and time, especially for large generated samples. Therefore, a faster and less detailed detector simulation is also needed.

4.2.2 Fast Monte Carlo: PMCS

The Parameterized Monte Carlo Simulation (PMCS) simulates the kinematic and geometric acceptance and detector response by using efficiencies and smearing parameters measured from data. The PMCS package [52, 53] is about 2000 times faster than the full detector simulation. The generated events have been processed through the p14.05.02 version of PMCS. Photons that have a momentum vector in a direction within $\Delta R = 0.2$ of the direction of an electron are merged with the electron; i.e. the photon 4-vector is added to that of the electron. The 0.2 cone size roughly corresponds to the extent of the EM clustering algorithm used in the calorimeter. If $\Delta R(e - \gamma) > 0.2$, the photon 4-vector is separate and treated as part of the recoil system. The momentum of the recoil system (i.e. hadronic particles recoiling against the e^+e^- pair) is calculated from the generator-level transverse momentum of the e^+ and e^-. The magnitude of the recoil momentum is multiplied by the hadronic energy response and smeared by the hadronic energy

resolution, both of which are determined from data [53].

In the PMCS detector simulation the reconstructed energy E of electrons is related to the generated electron energy E_0 by

$$E = \alpha E_0 + \delta \tag{4.1}$$

where α is the electron energy scale and δ is the energy offset. The EM resolution is parametrized by

$$\frac{\Delta E}{E} = \sqrt{C^2 + S^2 + N^2/E^2} \tag{4.2}$$

The sampling term S and noise term N are taken from test beam data; $S = 0.15$ GeV/c^2, and $N = 0.29$ GeV for the central calorimeter. The electron energy scale, energy offset, and electron resolution constant term are optimized for the PYTHIA/PHOTOS Drell-Yan Monte Carlo sample by tuning the Monte Carlo to data, using the methods described in [54]. A binned likelihood function is calculated using the following expression:

$$L = -\sum_{bins}[x_i \ln y_i - y_i - \ln x_i!], \tag{4.3}$$

where x_i is the number of data events in bin i and y_i is the number of Monte Carlo events in bin i. The Z-peak mass region used is $75 < M_{ee} < 105$ GeV/c^2. All

parameters are fixed, except for the one that is being evaluated using the binned likelihood function. The optimal value is determined from the minimum of a cubic polynomial fit to L. The following values are found to give best agreement with the data:

$$\alpha_{CC} = 1.006 \pm 0.003$$

$$\delta_{CC} = 0.069 \pm 0.045$$

$$C_{CC} = 0.045 \pm 0.002$$

Figure 4.1 shows the $-$log-likelihood fit for the electron energy scale in the CC region. The $-$log-likelihood fits for the energy offset and constant term in the CC region are shown in Fig. 4.2 and Fig. 4.3, respectively.

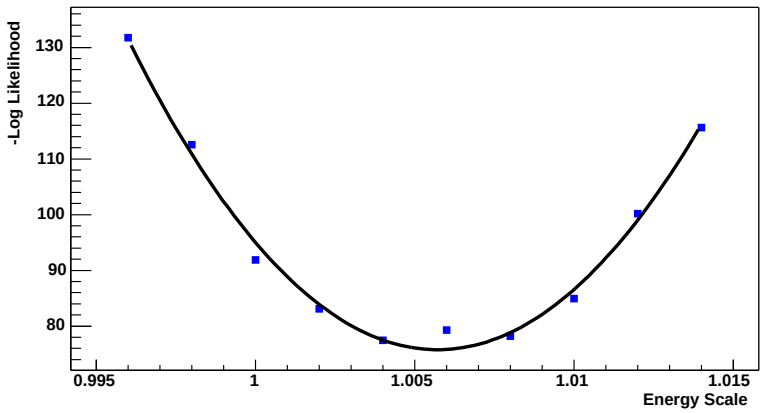

Figure 4.1: $-$Log likelihood vs. electron energy scale in the CC region.

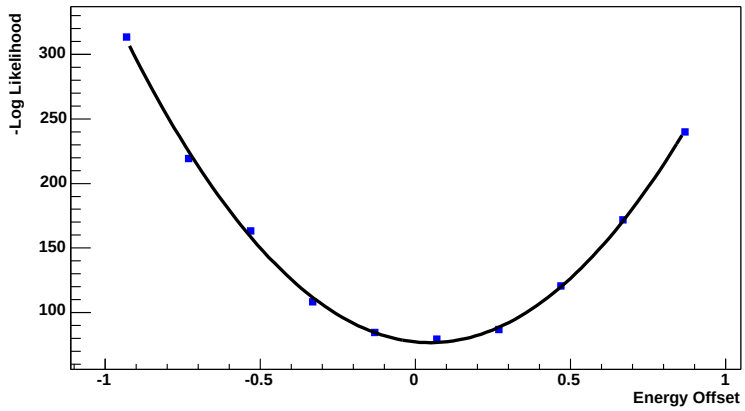

Figure 4.2: −Log likelihood vs. electron energy offset in the CC region.

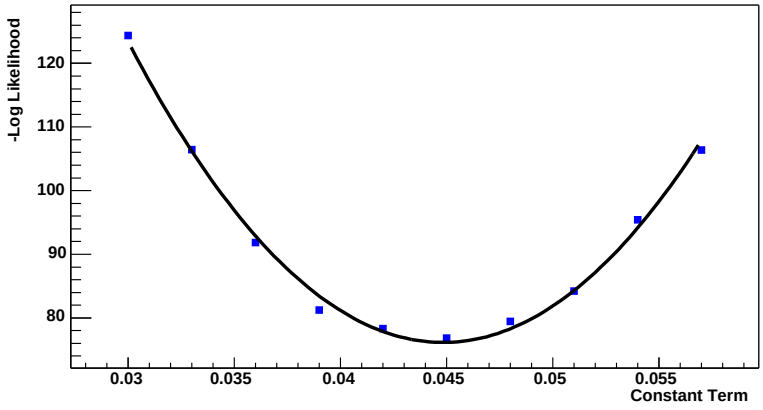

Figure 4.3: −Log likelihood vs. electron energy constant term in the CC region.

4.3 Drell-Yan Monte Carlo

In order to obtain a sufficient number of events at high dielectron invariant masses, the events are generated in several mass ranges. The invariant mass ranges, cross sections, and total number of events are given in Table 4.1. The total number of events generated in all mass ranges is 1,725,000.

Mass Region (GeV/c^2)	Avg. Cross Section (pb)	Pythia/Photos Events	No FSR Events
$40 < M_{ee} < 75$	26.49	450000	450000
$75 < M_{ee} < 110$	191.7	450000	450000
$110 < M_{ee} < 200$	3.523	375000	375000
$200 < M_{ee} < 500$	0.3029	225000	225000
$500 < M_{ee} < 1000$	0.004659	225000	225000

Table 4.1: Drell-Yan Monte Carlo samples.

Monte Carlo samples generated with PYTHIA using CTEQ6M, but without QED final state radiation (FSR) are used in obtaining the correction factor (see Section 8.2). Table 4.1 gives the invariant mass ranges, cross sections, and total number of events generated for the no-FSR sample. The total number of events generated for this sample in all mass ranges is 1,725,000.

Chapter 5

Event Selection

5.1 Data Samples

The stored data is reduced to a manageable size by selecting specific event characteristics. For this analysis, a sub-sample referred to as the CSskim-1EMloose sample, that requires at least one EM object with id $= 10, \pm 11$ and $E_T > 15$ GeV is used. There is no initial trigger requirement. Data was collected between run 161973 (August 2002) and run 180956 (September 2003). The data was reconstructed using d0reco versions p14.03.00, p14.03.01, p14.03.02, p14.05.00, p14.05.02, and p14.06.00. All corrections were made using the packages wz_analyze v01-00-12 and d0correct v00-00-06. Bad runs in which there were problems with the calorimeter, SMT or CFT are removed, as well as runs that have poor jet (i.e. low number of jets or phi distribution not flat) and missing E_T (i.e. x and y

Gaussian distributions are shifted from zero or phi dist. not flat) reconstruction are removed from the sample. Furthermore, data corresponding to bad luminosity blocks, which come from losses in the detector read-out or reconstruction processes, are not used in the analysis.

The total number of events, N, is calculated using the following equation:

$$N = \sigma \int \mathcal{L} dt, \tag{5.1}$$

where $\int \mathcal{L} dt$ is defined as the integrated luminosity, and σ is the cross section. For this analysis, an integrated luminosity of 177 ± 12 pb^{-1} was used, where 1 barn $\equiv 10^{-24}$ cm^2.

5.2 Trigger

Events are required to pass one of the following trigger combinations (given in order of preference) depending on which triggers were unprescaled[1] in a given run (refer to Table 5.1 for trigger term definitions):

- E1_SH30 or E1_SHT20 or E2_SHT20 or E3_SHT20
- E1_SH30 or E1_SHT20 or E2_SHT20
- E1_SH30 or E1_SHT20

[1]For prescaled triggers, random events are rejected in order to limit the total trigger rate.

- E1_SHT20
- EM_HI_SH or EM_HI_2EM5_SH
- EM_HI_SH
- EM_HI
- EM_MX_SH
- EM_MX

The first four bullets correspond to global trigger list CMT12 (runs $\geq$ 178722), and the rest correspond to CMT8-11 (runs $\leq$ 178721). Table 5.1 lists the trigger used and defines the trigger terms used in each level of trigger.

Trigger Name	L1	L2	L3
E1_SH30	CEM(1,11)	none	ELE_NLV_SH(1,30)
E1_SHT20	CEM(1,11)	none	ELE_NLV_SHT(1,20)
E2_SHT20	CEM(2,6)	none	ELE_NLV_SHT(1,20)
E3_SHT20	CEM(1,9)CEM(2,3)	none	ELE_NLV_SHT(1,20)
EM_HI_SH	CEM(1,10)	EM(1,12)	ELE_LOOSE_SH_T(1,20)
EM_HI_2EM5_SH	CEM(2,5)	EM(1,12)	ELE_LOOSE_SH_T(1,20)
EM_HI	CEM(1,10)	EM(1,12)	ELE_LOOSE(1,30)
EM_MX_SH	CEM(1,15)	none	ELE_LOOSE_SH_T(1,20)
EM_MX	CEM(1,15)	none	ELE_LOOSE(1,30)

L1 triggers	
CEM(1,9)CEM(2,3)	one EM trigger tower with $E_T > 9$ GeV another EM trigger tower with $E_T > 3$ GeV
CEM(1,10)	one EM trigger tower with $E_T > 10$ GeV
CEM(1,11)	one EM trigger tower with $E_T > 11$ GeV
CEM(1,15)	one EM trigger tower with $E_T > 15$ GeV
CEM(2,5)	two EM trigger towers with $E_T > 5$ GeV
CEM(2,6)	two EM trigger towers with $E_T > 6$ GeV

L2 triggers	
EM(1,12)	one EM candidate with $E_T > 12$ GeV (not present for runs < 169524)

L3 triggers	
ELE_LOOSE(1,30)	one loose electron is found satisfying $E_T > 30$ GeV and $\|\eta\| < 3$
ELE_LOOSE_SH_T(1,20)	one loose electron is found satisfying transverse shower shape requirements, $E_T > 20$ GeV, and $\|\eta\| < 3$
ELE_NLV_SH(1,30)	one loose electron is found satisfying loose shower shape requirements, $E_T > 30$ GeV, and $\|\eta\| < 3.6$
ELE_NLV_SHT(1,20)	one loose electron is found satisfying tight shower shape requirements, $E_T > 20$ GeV, and $\|\eta\| < 3.6$

Table 5.1: Single EM triggers and definitions of trigger terms.

5.3 Offline Electron Identification and Event Selection

Selected events must have at least two EM objects. To make sure that the EM objects closely resemble an electron, the following criteria are applied:

- "Loose" electron:
  - ID = 10 or ±11
  - EM Fraction > 0.9
  - Isolation < 0.15
  - CC: HMx7 $< 12 + slope \times (E_T - 45)$, where $slope = 0.020$ GeV^{-1}. Here HMx7 is a covariance matrix of 7 observables that takes into account simultaneously both the energy observed in a given layer and its correlations with energy deposited in the other layers. The covariance matrix is determined from GEANT based simulations. The H-Matrix χ^2 tends to slightly increase with electron energy, so a E_T-weighted cut is used to ensure the same efficiency for electrons over the full energy range (see Section 6.2).
- "Tight" electron:
  - All the "loose" electron requirements, plus

- A track matched to the calorimeter cluster with χ^2 probability greater than 0.01, where χ^2 is given by $\chi^2 = (\frac{\Delta z}{\sigma(z)})^2 + (\frac{\Delta \phi}{\sigma(\phi)})^2 + (\frac{E_T/p_T - 1}{\sigma(E_T/p_T)})^2$ and $\Delta z, \Delta\phi$ are the distances in z and ϕ between the extrapolated track and the EM cluster centroid.

Throughout this thesis, "electron" is used generically for an electron or a positron, since their experimental signature is identical in all respects except for the charge sign determined from the track curvature.

We require one "tight" and one "loose" electron per event. EM objects in the bad calorimeter cell region are not considered as electron candidates [53]. The "tight" electron is required in order to determine the charge sign of the electron, which is required for the A_{FB} measurement. The electrons are required to be within the detector region $|\eta_{det}| < 1.1$. The electrons must also be in the fiducial region of the detector (`in_fiducial`). This cut removes electron candidates in the cracks between EM modules in the CC ($\phi > 0.02$ radians from the module boundary), and at the calorimeter cryostat edges ($|z| < 115$ cm in the CC). Electrons in the cracks and cryostat edges are not well measured due to energy losses in these regions.

The electrons are required to have a transverse energy of $E_T > 25$ GeV. If more than two electrons in an event have these requirements only the two highest E_T electrons are chosen. The invariant mass distribution for the signal selection is shown in Fig. 5.1.

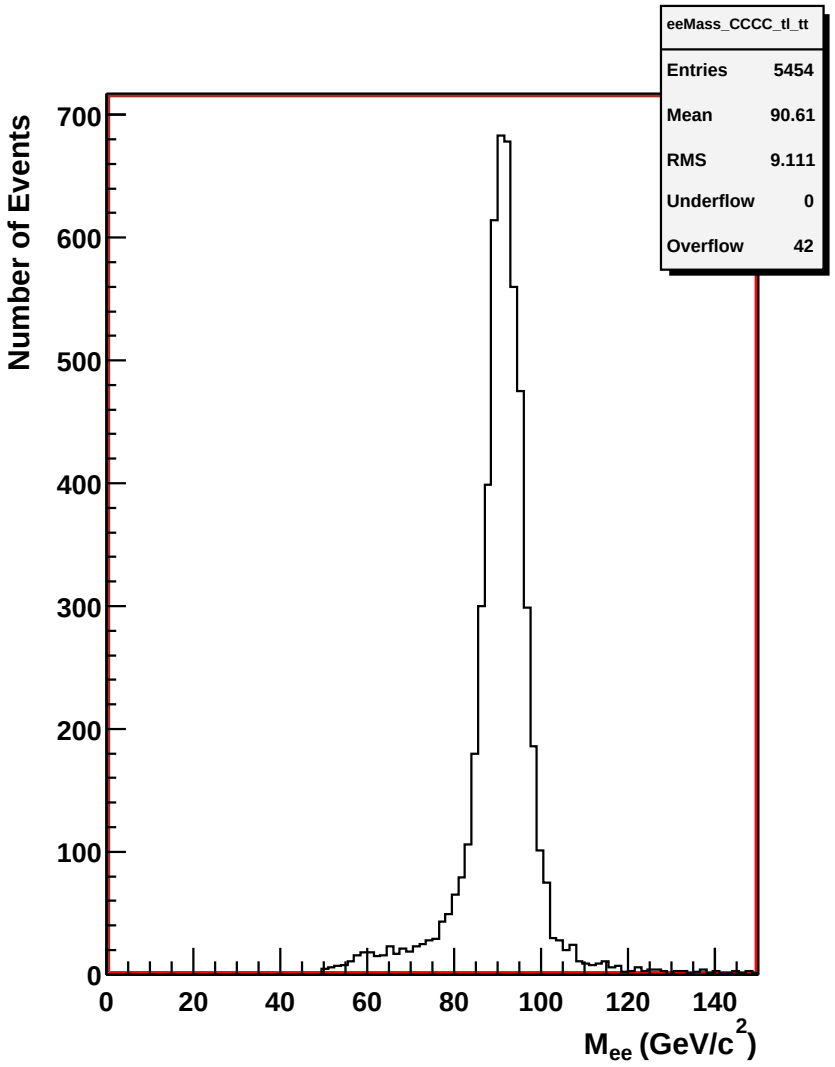

Figure 5.1: Distribution of ee invariant mass M_{ee} of the selected data sample.

Chapter 6

Detection Efficiencies

To account for the loss of real signal events due to trigger and offline selection cuts, the efficiency of each selection requirement must be calculated. Since $Z \rightarrow e^+e^-$ events are well understood and copious, they are ideal for efficiency studies.

6.1 Trigger Efficiency

The efficiency of the single electron trigger combination was calculated with the "tag/probe" method. First, two good EM clusters are selected with the following criteria:

- ID = 10 or $\pm$11
- $E_T > 15$ GeV

- EM Fraction > 0.9
- Isolation < 0.15
- CC: HMx7 $< 12 + slope \times (E_T - 45$ GeV), where $slope = 0.020$ GeV^{-1}
- `in_fiducial`: $\phi > 0.02$ radians from module boundary in CC; $|z| < 115$ cm in the CC
- $|\eta_{det}| < 1.1$
- Removed bad calorimeter cells [53]

The "tag" or highest E_T electron is a tight cut electron (has a track match and $E_T > 25$ GeV/c) and must pass the level 1, 2, and 3 requirements for the EM_HI_SH, EM_HI_2EM5_SH, E1_SHT20, or E2_SHT20 tight triggers. The "probe" or second highest E_T electron must pass the level 1, 2, and 3 requirements of the combined trigger (see Section 5.2). The trigger efficiency is the number of probe electrons divided by the number of tag electrons. The trigger efficiency versus electron E_T is shown in Fig. 6.1. The data is fit using an error function. The uncertainties in the efficiencies are calculated using the program described in Ref. [55], which accounts for the fact that only efficiencies between 0 and 1 are physical.

A Monte Carlo sample of Drell-Yan events is used to determine if the trigger efficiency has a mass dependence. The overall event trigger efficiency is calculated

using the same Monte Carlo sample described in Section 4.3. Using the same cuts as applied in the correction factor calculation, the individual electron trigger efficiency is calculated using the parametrized electron trigger efficiency versus E_T. If either electron passes the trigger requirement, then the event is retained. We calculate the event trigger efficiency versus M_{ee} by dividing the number of events retained by the total number of reconstructed events passing the acceptance cuts ($E_T > 25$ GeV, `in_fiducial`, $|\eta_{det}| < 1.1$). The event trigger efficiency versus M_{ee} is shown in Fig. 6.2. For the results presented in this thesis, we use a constant efficiency obtained from the straight line fit shown in Fig. 6.2: $\epsilon_{trig}^{CC-CC} = 1.0000^{+0.0000}_{-0.0002}(\text{stat.})^{+0.0000}_{-0.0006}(\text{sys.})$. The trigger efficiency systematic error is determined by calculating the trigger efficiency with a track match for both electrons then taking the difference between the two trigger efficiencies [53].

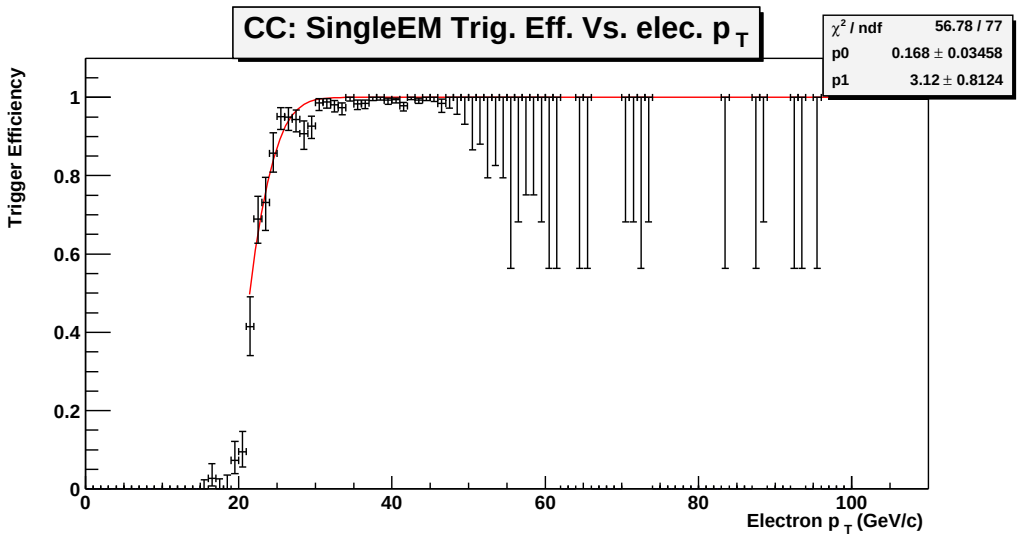

Figure 6.1: Single electron trigger efficiency vs. E_T.

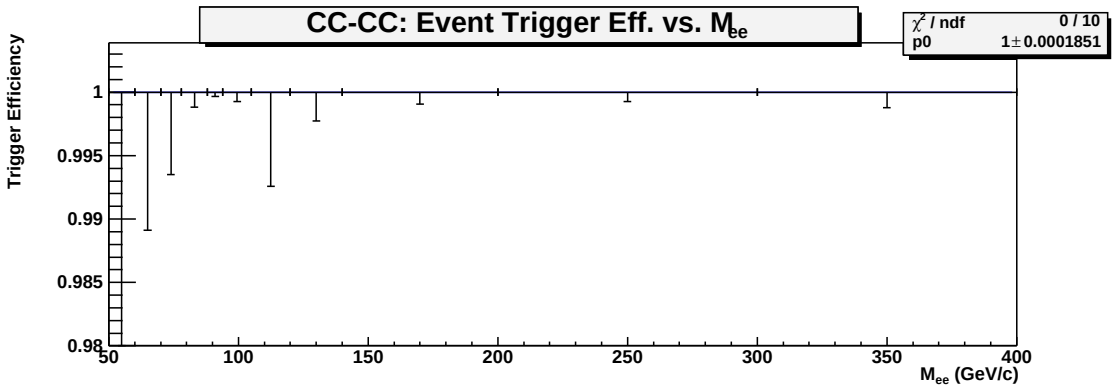

Figure 6.2: Event trigger efficiency vs. M_{ee}.

6.2 Electron Identification Efficiencies

Electrons are characterized by the following quality variables: EM fraction, Isolation, and HMx7. The EM fraction is the fraction of cluster energy measured in the electromagnetic layers of the calorimeter section divided by the total cluster energy (hadronic + EM). Isolation is defined by $I = (E_{\text{cone}} - E_{\text{core}})/E_{\text{core}}$, where E_{cone} is the energy in a cone of radius $R = 0.4$ around the direction of the electron, summed over the entire depth of the calorimeter, and E_{core} is the energy in a cone of $R = 0.2$, summed over the EM calorimeter only. Isolation rejects electron candidates which have nearby energy (e.g. from multijet events). HMx7 is a covariance matrix of 7 observables to take into account simultaneously both the energy observed in a given layer and cell and its correlations with energy deposited in the other layers and cells. This quantifies how closely an electromagnetic cluster

resembles a real electron, as predicted by a detailed GEANT simulation.

The EM-id efficiencies are calculated using $Z \rightarrow ee$ candidate events. The energy of the electrons from the $Z \rightarrow ee$ decay will be lower than electrons that come from Drell-Yan events at much higher invariant masses. Therefore, we must study how the EM-id variables vary with electron energy. For this study, we use Drell-Yan Monte Carlo events, run through the full GEANT-based detector simulation, that pass our acceptance cuts. Each electron identification variable is plotted versus the electron energy in the CC region. Figure 6.3 shows that the EM fraction and isolation have no significant energy dependence, but the H-Matrix has a slight energy dependence. The H-Matrix vs. E_T dependence is fit with a straight line shown in Fig. 6.4. The slope is found to be 0.020 ± 0.001 GeV^{-1} (CC).

For the calculation of EM-id efficiencies, we use the same data sample as is used for the signal selection. The "tag/probe" method is used, where the "probe" electron must have ID = 10 or $\pm$11, `in_fiducial`, $|\eta_{det}| < 1.1$, and $E_T > 25$ GeV. The "tag" electron is a probe electron with all of the electron selection EM-id cuts and a track match. The efficiency is the number of probe electrons passing the cut under study divided by the total number of probe electrons:

$$\epsilon_{cut} = \frac{2(tt) + (tp)}{2(tt) + (tp) + (tf)}, \tag{6.1}$$

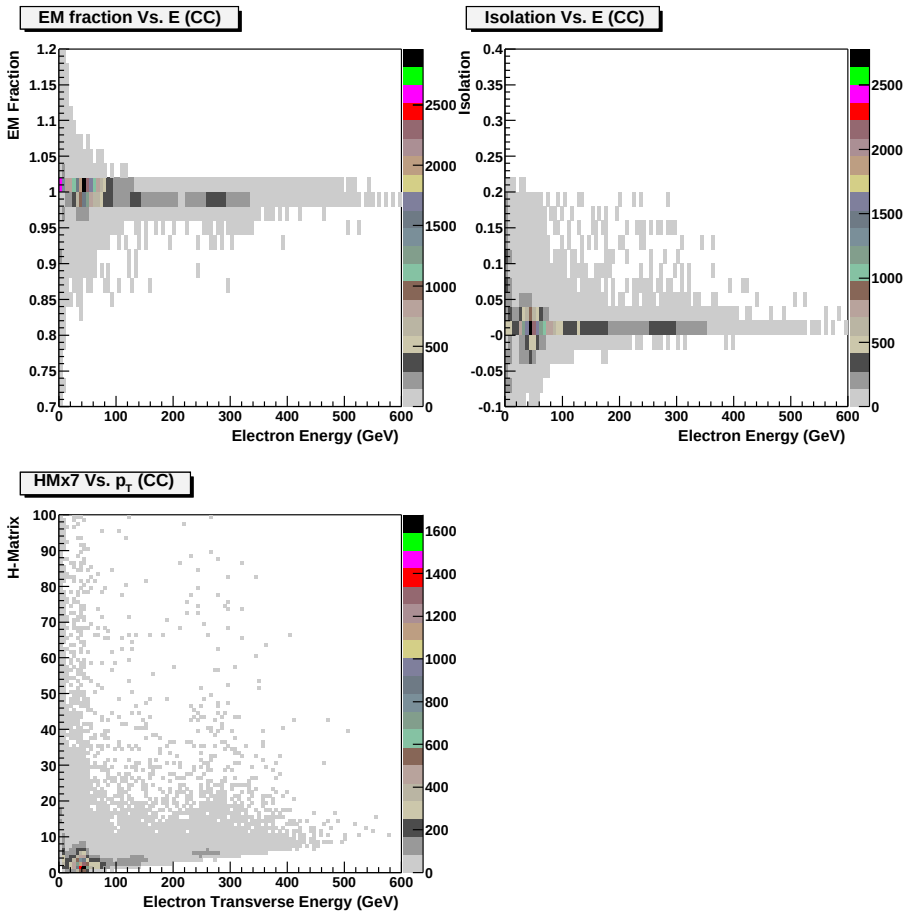

Figure 6.3: Monte Carlo EM-id variables vs. electron energy distributions for the CC region.

where

tt = number of events where both electrons pass the tag cuts (and therefore pass the cut under study);

tp = number of events where one electron passes the tag cuts and the other passes the cut under study but fails the tag cuts;

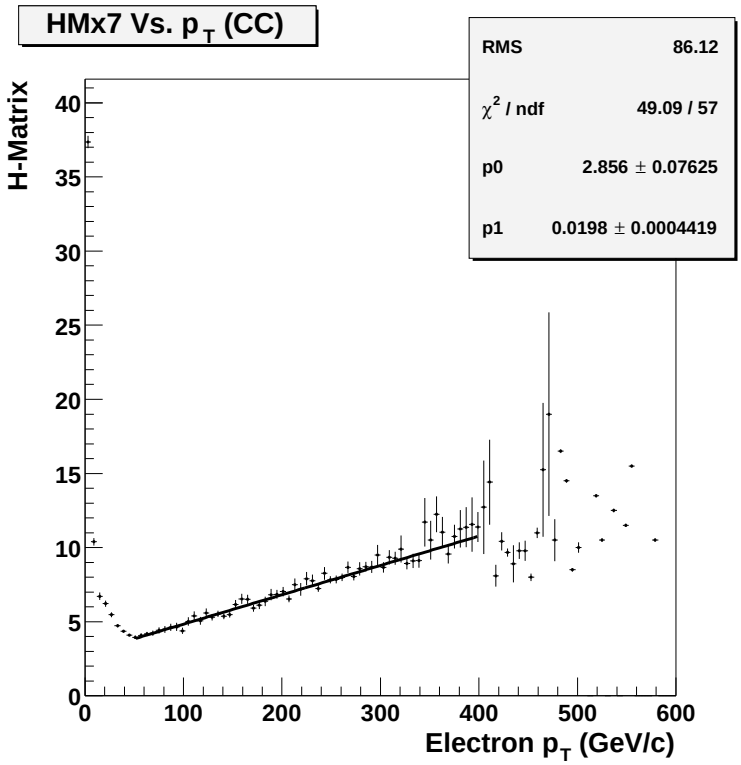

Figure 6.4: HMx7 vs. electron E_T distribution for the CC region.

tf = number of events where one electron passes the tag cuts and the other electron fails the cut under study (and therefore fails the tag cuts as well).

The background invariant mass distribution is estimated using four methods [56]:

1. Sideband Technique: Two sidebands ($60 < M_{ee} < 70$ GeV/c^2 and $110 < M_{ee} < 120$ GeV/c^2) on each side of the signal region ($86 < M_{ee} < 96$ GeV/c^2) are chosen. The sidebands are symmetric around the signal region, and span the same invariant mass range. The estimated number of

background events is then the average of the two sidebands.

2. Sideband Technique: Similar to Method 1, but with a signal region between $81 < M_{ee} < 101$ GeV/c^2. And the estimated number of background events is then the sum of the two sideband regions.

3. Breit-Wigner/Gaussian with Linear Fit: The invariant mass is fit with a Breit-Wigner convoluted with a Gaussian, which accounts for the resolution in the measurement, and a linear background in the region $70 < M_{ee} < 110$ GeV/c^2. The signal region is chosen to be $86 < M_{ee} < 96$ GeV/c^2. The parameters from the fit are then used to estimate the background.

4. Similar to Method 3, but the signal region is chosen to be $81 < M_{ee} < 101$ GeV/c^2.

Methods 3 and 4 are also repeated using an exponential background shape and the EM-id efficiencies found were similar to those found using the linear background. The M_{ee} distributions for the numerator and denominator in Eq. (6.1) using methods 3 and 4 with the linear background are shown in Fig. 6.5. The EM-id efficiency is $(91.89 \pm 0.34)\%$ for method one, $(92.51 \pm 0.29)\%$ for method two, $(92.80 \pm 0.32)\%$ for method three, and $(92.57 \pm 0.29)\%$ for method four. Method 4 is used to quote the central value of the efficiency; it is the closest method calculated with the linear background to the average of the four methods. The

individual numbers of tt, tp, and tf events integrated over the Z-peak region for method 4 are:

- CC region:

$$tt = 3012.13 \pm 165.30$$

$$tp = 1536.91 \pm 171.76$$

$$tf = 611.28 \pm 120.36$$

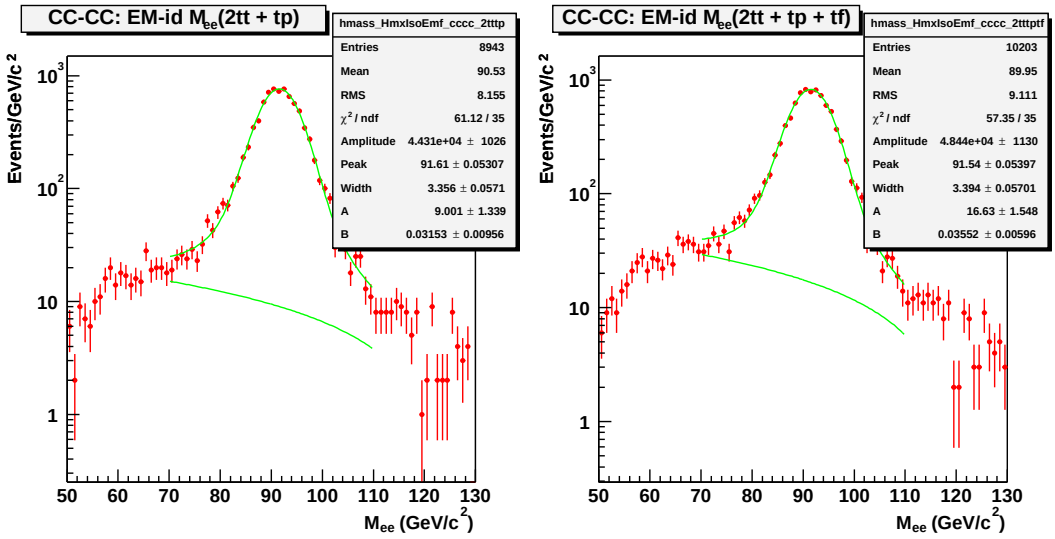

Figure 6.5: Invariant mass M_{ee} distributions for the numerator (left) and denominator (right) of Eq. (6.1) used to determine the EM-id efficiency with background subtraction methods 3 and 4. The points are the data and the lines show the linear background estimate and the result of the fit to a Breit-Wigner convolved with a Gaussian plus a linear background.

The systematic error is determined by subtracting the method that gives the lowest EM-id efficiency by the method that gives the highest EM-id efficiency and

then dividing by two. We obtain an EM-id efficiency with total error of $\epsilon^{CC}_{EM-id} = (92.57 \pm 0.54)\%$.

To determine the EM-id efficiency as a function of invariant mass, we model the EM-id efficiency using a GEANT-based Monte Carlo, then normalize the distribution to data in the Z-peak region. The efficiency for Monte Carlo events to have two EM objects passing the EM-id requirements is shown separately for forward and backward events in Fig. 6.6. The decrease in efficiency below and above the Z-pole is due to a combination of bin migration, due to detector resolution, and photon radiation. Photon radiation can affect the HMx7, isolation, and EM fraction variables, causing the electron to fail the EM-id requirements. The largest effect is on the HMx7 variable. Since the efficiencies for forward and backward events are consistent with one another within the statistical uncertainties, we use the overall EM-id efficiency for all events. Figure 6.7 shows the Event EM-id efficiency versus invariant mass, which has been normalized to data.

6.3 Track Match Efficiency

Requiring an EM cluster to have a matching track helps to remove a large background from QCD multijet production. Isolated EM objects in QCD events are from photons or π^0 mesons, which should not have tracks associated with them.

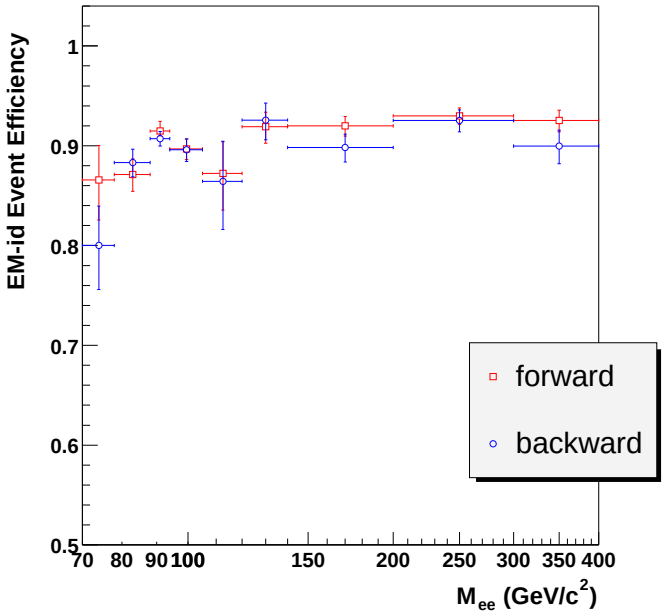

Figure 6.6: Efficiency for Monte Carlo events to pass the EM-id requirements vs. M_{ee} for forward and backward events. The efficiencies are not normalized to data.

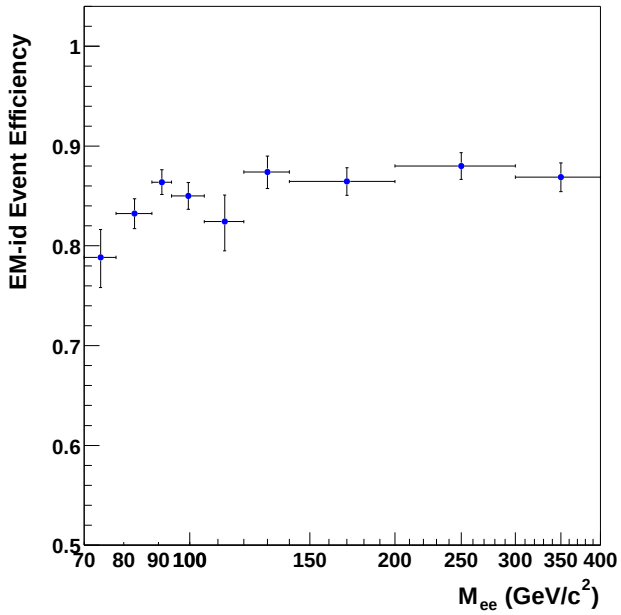

Figure 6.7: Event EM-id efficiency vs. M_{ee} for all events. The efficiencies are normalized to data.

The track match chi-square is defined by

$$\chi^2_{CC} = \left(\frac{\Delta z}{\sigma(z)}\right)^2 + \left(\frac{\Delta \phi}{\sigma(\phi)}\right)^2 + \left(\frac{E_T/p_T - 1}{\sigma(E_T/p_T)}\right)^2, \tag{6.2}$$

where $\Delta z, \Delta\phi$ are the distances in z, ϕ between the extrapolated track and the EM cluster centroid, E_T is the transverse energy of the EM cluster measured in the EM

calorimeter, and p_T is the transverse momentum of the track determined from its curvature.

The track match efficiency is calculated using $Z \rightarrow ee$ candidate events. The same data sample as was used to calculate the EM-id efficiency is used here. Events should have at least two EM objects, and the two highest E_T EM objects must pass the "loose" electron cuts. Each "loose" electron is tested to see if it has a matched track. The efficiency is given by:

$$\epsilon_{trk} = \frac{2N_2}{N_1 + 2N_2}, \tag{6.3}$$

where N_1 is the number of events with one cluster matched to a track, and N_2 is the number of events with both clusters matched to tracks. The backgrounds are calculated using the same four methods as are used for the EM-id efficiency. The M_{ee} distributions for the numerator and denominator in Eq. (6.3) using methods 3

and 4 with the linear background are shown in Fig. 6.8. The track-match efficiency is found to be $(79.45 \pm 0.52)\%$ for method one, $(79.40 \pm 0.47)\%$ for method two, $(79.85 \pm 0.52)\%$ for method three, and $(79.68 \pm 0.46)\%$ for method four. Method 4 is used to quote the central value of the efficiency; it is the closest method calculated with the linear background to the average of the four methods. The individual numbers of two-track, one-track and zero-track events, integrated over the Z-peak region are:

- CC region:

  0 Track Match = 126.48 ± 137.95

  1 Track Match (N_1) = 1537.90 ± 171.82

  2 Track Match (N_2) = 3014.09 ± 233.84

The M_{ee} distributions for the numerator and denominator in Eq. (6.3) using methods 4 with the linear background are shown in Fig. 6.8. The track match efficiency is found to be $(79.68 \pm 0.46)\%$.

The systematic error is determined by subtracting the method that gives the lowest efficiency by the method that gives the highest efficiency and then dividing by two. We obtain a track-match efficiency of $\epsilon_{trk}^{CC} = (79.68 \pm 0.51)\%$.

To determine the track match efficiency as a function of invariant mass, we model the track match efficiency using Monte Carlo, then normalize the distribution to data in the Z-peak region. We look at the efficiency for events to

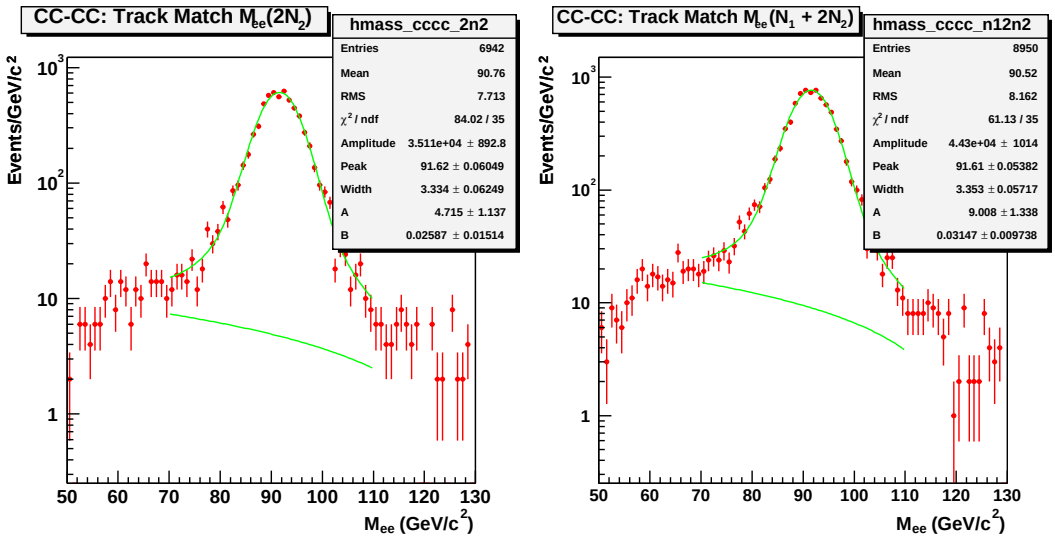

Figure 6.8: Invariant mass distributions for the numerator (left) and denominator (right) in Eq. (6.3) used to calculate the track match efficiency with background subtraction methods 3 and 4. The points are the data and the lines show the linear background estimate and the result of the fit to a Breit-Wigner convolved with a Gaussian plus a linear background.

pass the requirement of at least one track match separately for forward and backward events and find that they are consistent. This is shown in Fig. 6.9. Therefore, we use the overall track match efficiency for all events. Figure 6.10 shows the event track match efficiency versus invariant mass, which has been normalized to data. The decrease in efficiency below and above the Z-pole is due to a combination of bin migration and photon radiation.

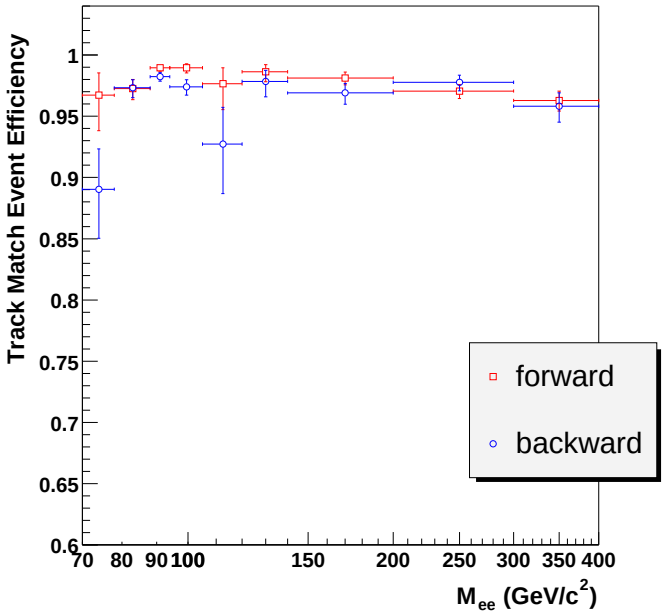

Figure 6.9: Efficiency for Monte Carlo events to pass the requirement of at least one track match vs. M_{ee} for forward and backward events. The efficiencies are not normalized to data.

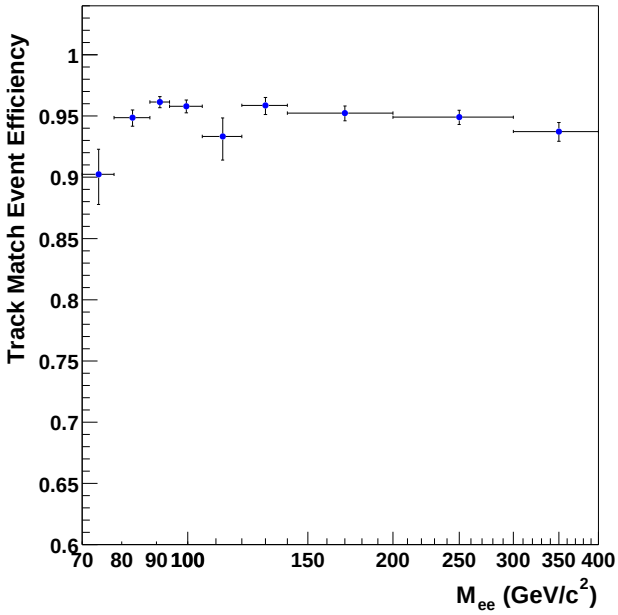

Figure 6.10: Event track match efficiency vs. M_{ee} for all events. The efficiencies are normalized to data.

Chapter 7

Backgrounds

The largest source of background for Drell-Yan events is the production of multijet and direct photon events, in which the jets have a large electromagnetic component (most of the energy is deposited in the EM section of the calorimeter) or they are mismeasured in some way that causes them to pass the electron selection criteria. This will be referred to as the QCD background. Other backgrounds are much smaller and originate mainly from $Z \to \tau\tau$, W + jets production, $t\bar{t}$ production ($t\bar{t} \to ee$), and diboson production ($W\gamma \to e\nu\gamma, WW \to ee, WZ \to ee, ZZ \to ee$).

7.1 Matrix Method

To estimate the overall normalization of the QCD background, the matrix method is used. A relatively loose sample of M $\gamma^*/Z \to ee$ events are chosen by requiring events to contain two loose electrons (the *mother* sample). We then impose tighter cuts (requiring one of the electron candidates to have a track match) and obtain a *child* subsample containing P events which pass the tight cuts, and a subsample with F events that fail the tight cuts.

The mother sample actually contains three true subsamples: one with N_s signal events comprised of the real $\gamma^*/Z \to ee$ (but also including a small number of $\tau\tau$, $t\bar{t}$, and diboson events), one with B QCD background events, and one with B_W background events from the $W(\to e\nu) + X$ background. If the efficiencies for these subsamples to pass the tight cuts (relative to the loose cuts of the parent sample) are ϵ_s for the signal, ϵ_b for the QCD background events, and ϵ_w for the $W \to e\nu + X$ events, then the number of events passing and failing are

$$P = \epsilon_s N_s + \epsilon_b B + \epsilon_w B_W \tag{7.1}$$

$$F = (1-\epsilon_s) N_s + (1-\epsilon_b) B + (1-\epsilon_w) B_W \tag{7.2}$$

From the conservation of the total number of events in the parent sample, we also

have:

$$M = P + F \tag{7.3}$$

The total number of QCD background events which pass the tight cuts is

$$N_{QCD} = \epsilon_b B \tag{7.4}$$

and the QCD background fraction is

$$f_{QCD} = \frac{N_{QCD}}{P}. \tag{7.5}$$

Solving for N_{QCD} we find

$$N_{QCD} = \epsilon_b \left(\frac{\epsilon_s M - P + (\epsilon_w - \epsilon_s) B_W}{\epsilon_s - \epsilon_b} \right) \tag{7.6}$$

Thus, the QCD background estimate can be obtained from the efficiencies and the estimate of the $W(\rightarrow e\nu) + X$ background (see Section 7.2).

The signal efficiency for events requiring one tight and one loose electron, both in the CC, is related to the track match efficiency by:

$$\epsilon_s = \epsilon_{tm,CC}(2 - \epsilon_{tm,CC}) \tag{7.7}$$

where $\epsilon_{tm,CC}$ is the track match efficiency in the CC region described in Section 6.3. For the $W(\rightarrow e\nu) + X$ background we have

$$\epsilon_w = \epsilon_{tm,CC} \tag{7.8}$$

The QCD background efficiency is related to the fake track match probability by

$$\epsilon_b = \epsilon_{fake,CC}(2 - \epsilon_{fake,CC}) \tag{7.9}$$

where $\epsilon_{fake,CC}$ is the fake track match probability in the CC region.

7.1.1 Fake Track Match Probability

The fake track match probability is the probability of a QCD-produced EM object having a fake track match. The same data sample as used for electron selection is used to determine the fake track match probability. Events must pass the luminosity quality and trigger requirements as used for the electron selection. Events with one jet candidate and one EM object are selected, and the requirement $\not\!\!E_T < 10$ GeV is imposed to remove W + jet events. The EM object must pass the "loose" electron criteria described above. Jet candidates are identified using the cone algorithm with $R = 0.7$.

The jets are required to have a Level 1 trigger confirmation and pass

standard jet quality cuts. In addition, to further remove real electrons from the sample, we require the jets to pass requirements that are somewhat more stringent than the standard cuts as follows:

- N90 > 1
- F90 < 0.65
- $0.05 <$ EM fraction < 0.7
- CHF < 0.25
- Hot fraction < 5.0
- $N_{trk} \geq 5$

where

N90 is the number of towers in a jet that contain 90% of the jet energy.

F90 = N90/(total number of towers in a jet).

CHF is the fraction of the jet energy deposited in the coarse hadronic section of the calorimeter.

Hot fraction is the largest uncorrected energy from any cell divided by the second highest energy cell in a jet. It cuts on cells of the calorimeter that have energy deposition not related to a real event.

N_{trk} is the number of tracks in a jet ($\Delta R < 0.5$). This cut reduces possible background from $Z \rightarrow \tau\tau$ decays.

The electron candidate must be back-to-back with the good jet ($\Delta\phi(e - jet) > 2.5$). We then look to see if the electron candidate has a track matched to it. The probability that a QCD-produced EM object having a fake track match ("fake rate") is the fraction of these electron candidates which have a track match. The fake rate as a function of electron E_T is shown in Fig. 7.1. An overall systematic uncertainty of $\pm 13\%$ is assigned to the fake rate, because of variations of the fake rate as a function of pseudorapidity and transverse energy [53]. We assume a constant fake rate, with variations with transverse energy accounted for in the systematic error, and find the final fake rate to be $(1.6 \pm 0.2)\%$.

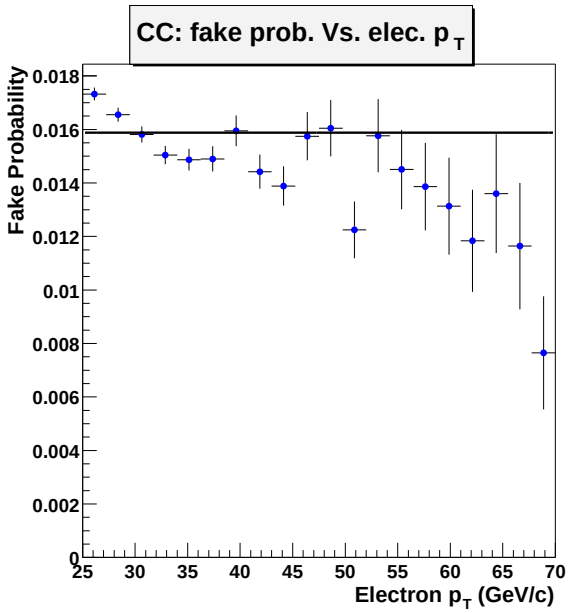

Figure 7.1: Fake track match probability vs. electron E_T.

7.1.2 QCD Background Calculation

The shape of the background invariant mass distribution is obtained from di-EM events passing all the cuts used for the signal selection, except that the EM objects must fail the H-matrix chi-square cut: HMx8 > 35, and have no tracking requirement. HMx8 is the similar to HMx7 with the addition of the transverse shower shape in z. We use this H-Matrix cut, because it is known to model the QCD background. We could have used an HMx7 cut, but then we would have to optimize that cut for the QCD background. These are predominantly dijet events. These events are also divided into forward and backward events. The background shapes for the forward and backward events are consistent within errors and therefore we use one shape for all events. This is shown in Fig. 7.2. The background is normalized using the matrix method described above. The mother sample (M) is selected by requiring two loose electrons and the Drell-Yan candidate event sample (P) is selected by requiring one tight electron and one loose electron. The resulting background distributions are shown in Fig. 7.3 and Fig. 7.4. The result for the estimated number of background events for the mass range 70 GeV $< M_{ee} <$ 400 GeV is $N_{QCD} = 62.5 \pm 8.0$ for all events, $N_{QCD} = 31.1 \pm 4.0$ for forward events, and $N_{QCD} = 31.4 \pm 4.0$ for backward events. The number of selected events in the data is $N_{data} = 5259 \pm 73$ for all events, $N_{data} = 2730 \pm 52$ for forward events, and $N_{data} = 2529 \pm 50$ for backward events. We find the QCD background fraction to

be $f_{QCD} = 0.0119 \pm 0.0015$ for all events, $f_{QCD} = 0.0114 \pm 0.0015$ for forward events, and $f_{QCD} = 0.0124 \pm 0.0016$ for backward events.

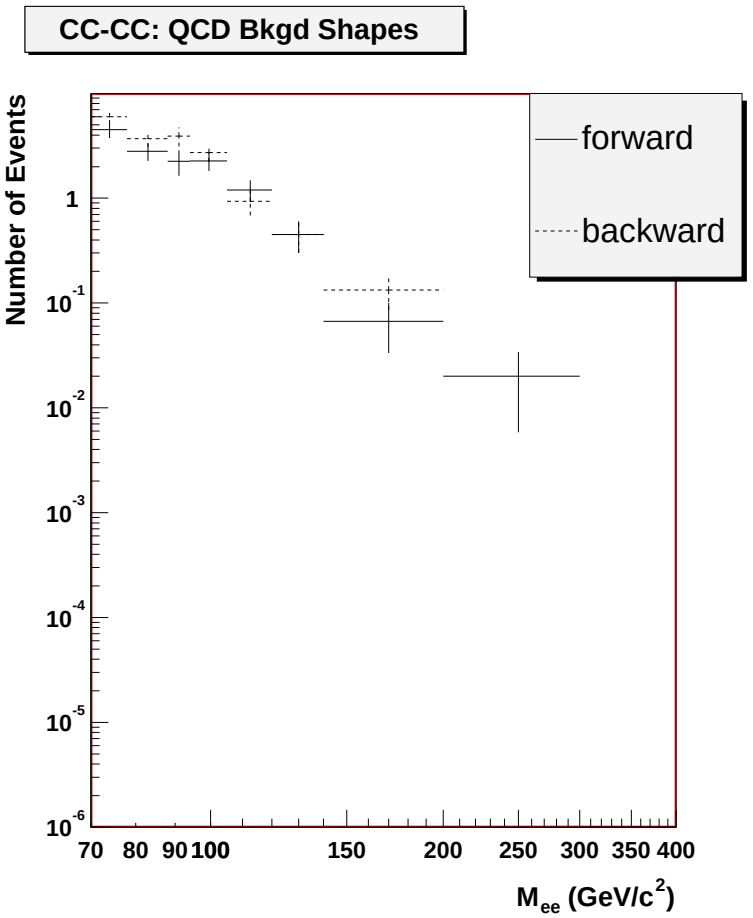

Figure 7.2: QCD background shape for forward and backward events. Matrix method normalization has not been applied.

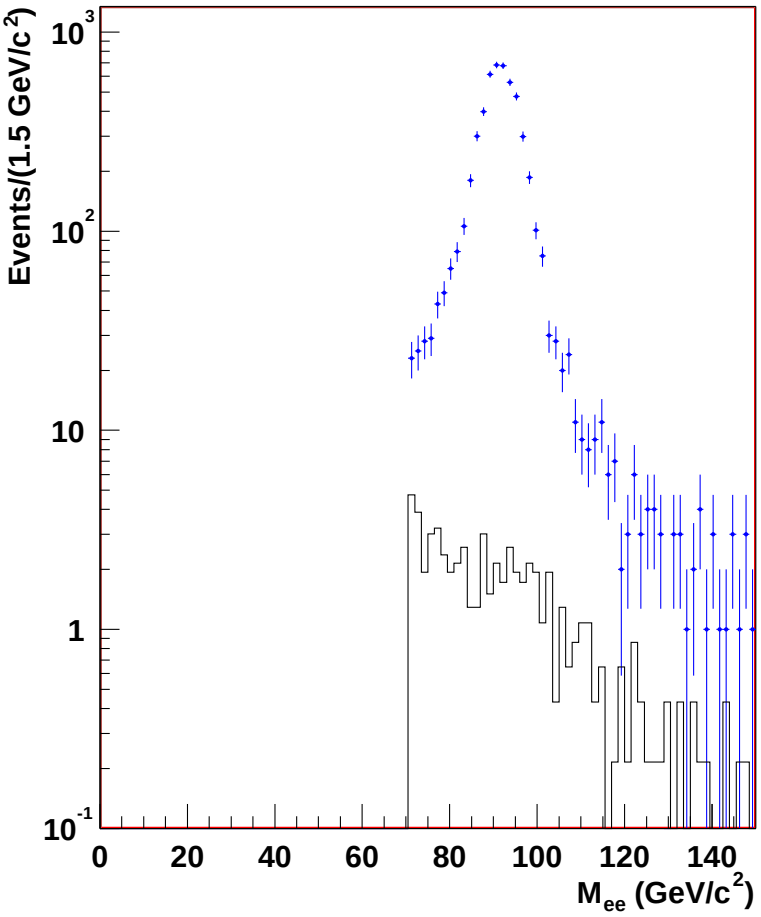

Figure 7.3: Invariant mass distributions for data (points with error bars) and estimated QCD background (histogram) in the mass region $70 < M_{ee} < 150$ GeV with 1.5 GeV bin width.

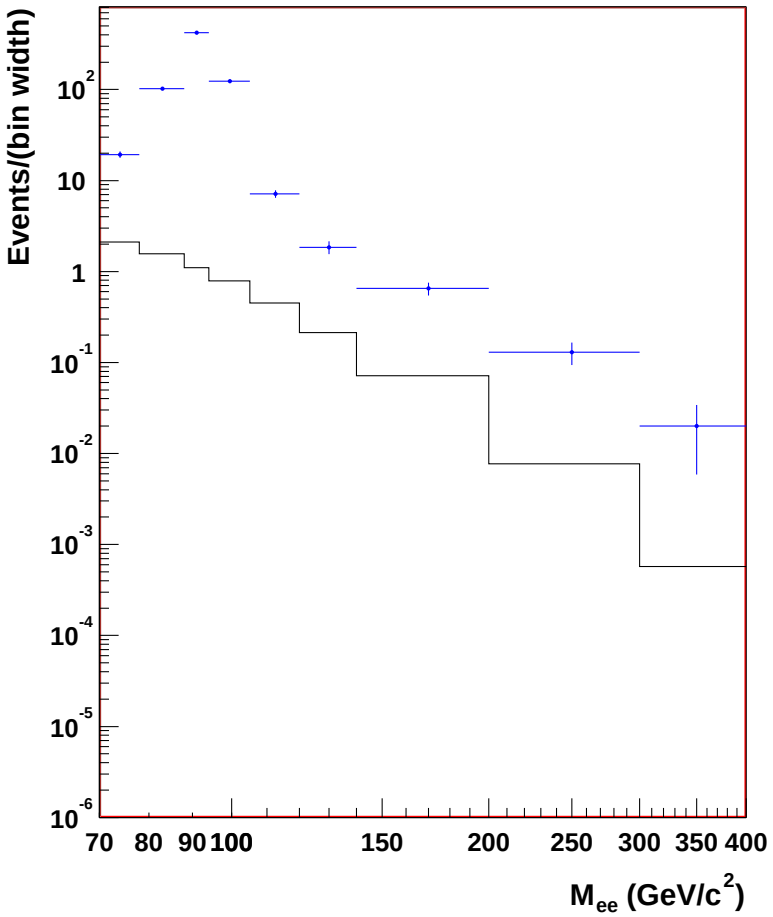

Figure 7.4: Invariant mass distributions for data (solid circles with error bars) and estimated QCD background (histogram) in the mass region $70 < M_{ee} < 400$ GeV with variable bin width.

7.1.3 W + jets Background

The background from W + jets events, where a jet fakes an electron, is obtained from a Monte Carlo sample of W + jets events. The probability for a jet to fake an electron is obtained from a jet data sample.

Probability for a Jet to Fake an Electron

A data sample of mostly dijet events is used to calculate the probability for a jet to fake an electron. The data sample is required to pass jet and minimum bias triggers. Events are required to pass one of the following two triggers:

- JT_25TT_NG: Two Level 1 calorimeter towers above 5 GeV, and a jet reconstructed at Level 3 with $E_T > 25$ GeV.
- JT_45TT: Two Level 1 calorimeter towers above 5 GeV, and a jet reconstructed at Level 3 with $E_T > 45$ GeV.

The lead jet (using the 0.5 cone algorithm) must pass the following jet quality requirements:

- $0.05 <$ Jet EM Fraction (EMF) < 0.90
- Jet Coarse Hadronic Fraction (CHF) < 0.4
- Jet Hot Fraction (HotF) < 10
- Jet N90 > 1

- Jet F90 < 0.5 or Jet CHF < 0.15,

and is required to pass the offline trigger requirements:

- Two Level 1 calorimeter towers above 5 GeV had to be matched to the lead jet. A match is defined as $\delta\phi_{det}(jet - tower) < 0.3$ and $\delta\eta_{det}(jet - tower) < 0.3$.

- The Level 3 jet must pass the appropriate Level 3 E_T threshold and be within $\Delta R(jet - tower) < 0.5$.

The leading jet must also pass the following tighter jet cuts:

- $0.05 <$ Jet EMF < 0.7

- Jet CHF < 0.25

- Jet HotF < 5

- Jet N90 > 1

- $N_{trks} \geq 5$.

- $|\eta_{det}| < 1.1$.

The event must also have missing transverse energy $\not\!\!E_T < 10$ GeV.

After finding events with $\not\!\!E_T < 10$ GeV in which the lead jet passes the above requirements, we loop over the remaining jets (which are unbiased by the

trigger requirements) to find probe jets for the probability calculation. The probe jets must be separated from the lead jet by $\Delta R > 1.5$ and must pass the following jet quality cuts:

- $0.05 <$ Jet EMF < 0.95
- Jet CHF < 0.4
- Jet HotF < 10
- Jet N90 > 1
- $|\eta_{det}| < 1.1$.

We then find the number of EM objects passing the good electron requirements:

- id = 10 or $\pm$ 11
- EM Isolation < 0.15
- EMF > 0.9
- HMx7 $< 12 + slope \times (E_T - 45)$
- `in_fiducial`
- $p_T > 25$
- $|\eta_{det}| < 1.1$.

The EM objects were also required to be separated from the lead jet by $\Delta R > 1.5$ and separated from the probe jets by $\Delta R > 0.7$ to make sure that they were not part of any of the jets. The electron p_T was required to be less than the lead jet p_T to make sure that the lead jet was the tag object in the event. The fake probability is equal to the number of good EM objects divided by the total number of probe jets and EM objects:

$$P_{jet \to e} = \frac{EM_{good}}{\text{Probe jets} + EM_{good}}. \tag{7.10}$$

We find the probability for a jet to fake an electron to be

$P_{jet \to e} = 0.003 \pm 0.0001(\text{stat.})$.

Calculation of the W + jets Background

To obtain the invariant mass distribution of the W + jets background a Monte Carlo sample of $W(\to e\nu)$ + jets is used. The EM candidate is required to pass the same EM-id and track match requirements as used in the data signal selection and the jet candidates must pass the probe jet cuts used in the fake probability study above. The Monte Carlo events are then weighted by $P_{jet \to e}$ and efficiencies are applied using the efficiencies normalized to the data efficiencies. The invariant mass distribution of the resulting W + jets background is shown in Fig. 7.5.

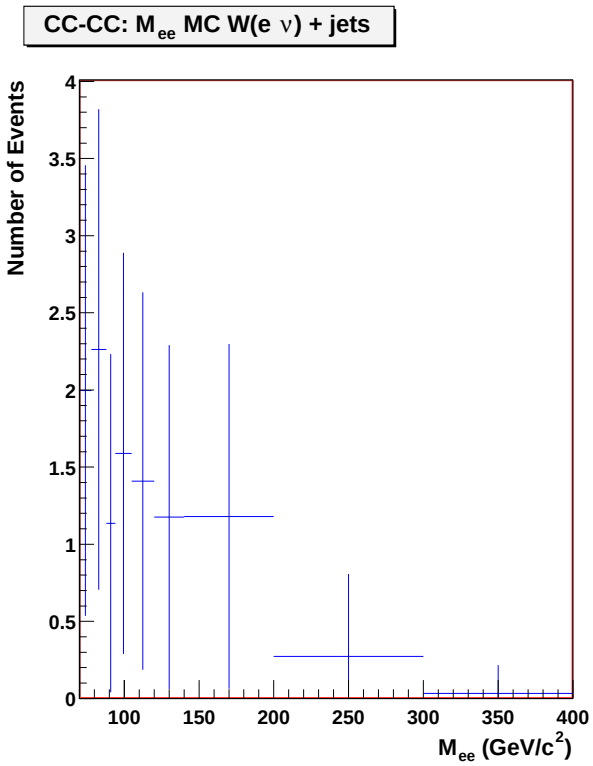

Figure 7.5: Invariant mass distribution of background events from W + jets.

7.2 Other Backgrounds

Other backgrounds are much smaller and originate mainly from $Z \rightarrow \tau\tau$, $t\bar{t}$ production, and diboson production. These backgrounds are estimated from samples of Monte Carlo events that must pass acceptance cuts and are scaled by the event efficiencies derived from data and a K-factor of $\approx 1.2 - 1.4$, obtained from the ratio of the NLO cross section to the Monte Carlo generated cross section. We have considered the the following sources of additional backgrounds:

- $\gamma^*/Z \rightarrow \tau\tau$
- $t\bar{t} \rightarrow ee$
- $W\gamma \rightarrow e\nu\gamma$
- $WW \rightarrow ee$

Figure 7.6 shows the invariant mass distributions of these backgrounds. The total number of events from these backgrounds for each mass bin are given in Table 7.1. All of these backgrounds, including the QCD and W + jets backgrounds, have been subtracted in the cross section calculation.

Mass Bin (GeV/c^2)	$\gamma^*/Z \rightarrow \tau\tau$	$t\bar{t} \rightarrow ee$	$W\gamma \rightarrow e\nu\gamma$	$WW \rightarrow ee$	$W(\rightarrow e\nu) + jets$
70 − 78	0.8595 ± 1.0473	0.1328 ± 0.3838	1.0231 ± 1.0394	0.2347 ± 0.5311	1.9968 ± 1.4605
78 − 88	0.8664 ± 1.0515	0.1656 ± 0.4287	0.3410 ± 0.5976	0.2347 ± 0.5311	2.2621 ± 1.5570
88 − 94	0.1257 ± 0.4005	0.1136 ± 0.3550	1.0231 ± 1.0394	0.1370 ± 0.4058	1.1361 ± 1.0961
94 − 105	0.0753 ± 0.3100	0.1779 ± 0.4443	0.3410 ± 0.5976	0.2108 ± 0.5033	1.5888 ± 1.2997
105 − 120	0.1473 ± 0.4335	0.2135 ± 0.4867	0.3410 ± 0.5976	0.2327 ± 0.5289	1.4095 ± 1.2228
120 − 140	0.2404 ± 0.5538	0.2190 ± 0.4929	0.0000 ± 0.0000	0.1978 ± 0.4876	1.1761 ± 1.1154
140 − 200	0.0944 ± 0.3471	0.3271 ± 0.6024	0.3410 ± 0.5976	0.2382 ± 0.5351	1.1801 ± 1.1174
200 − 300	0.0173 ± 0.1486	0.1382 ± 0.3916	0.0000 ± 0.0000	0.1121 ± 0.3671	0.2734 ± 0.5349
300 − 400	0.0096 ± 0.1105	0.0164 ± 0.1350	0.0000 ± 0.0000	0.0169 ± 0.1427	0.0325 ± 0.1841
70 − 400	2.4358 ± 1.7631	1.5041 ± 1.2919	3.4104 ± 1.8946	1.6149 ± 1.3933	11.0553 ± 3.4287

Table 7.1: Numbers of background events from $\tau^+\tau^-$, $t\bar{t}$, $W\gamma$, WW, and $W + jets$ for each mass bin. The last row gives the total backgrounds for the whole range 70-400 GeV.

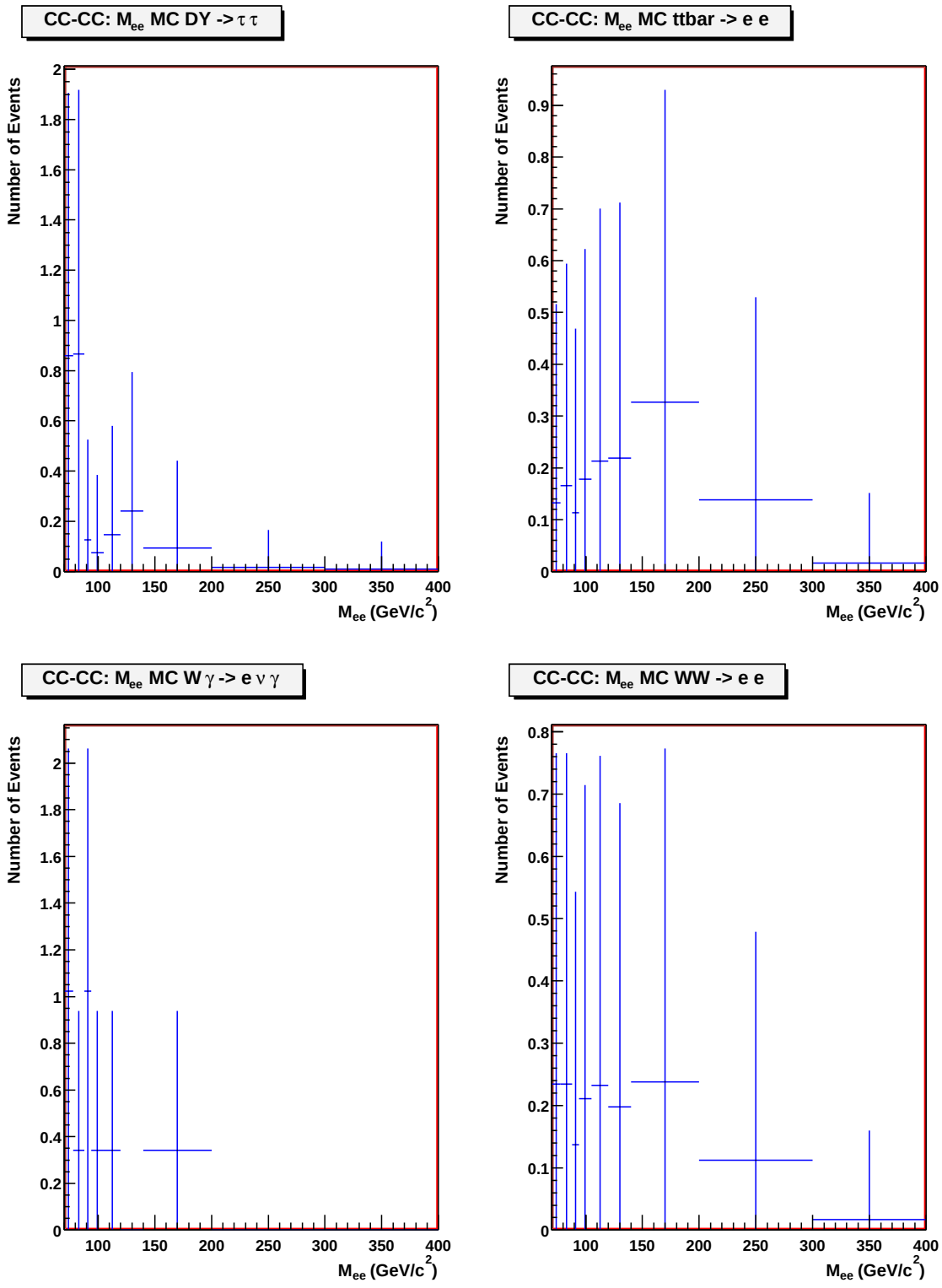

Figure 7.6: Invariant mass distributions of background events from $\tau^+\tau^-$, $t\bar{t}$, $W\gamma$, and WW.

Chapter 8

Results

8.1 Comparison of Monte Carlo and Data

To model equivalent data distributions, the Drell-Yan Monte Carlo events are weighted by the factor $\mathcal{L}\sigma/N$, where $\mathcal{L}$ is the integrated luminosity of the data, σ is the Monte Carlo cross section, and N is the number of events generated in the relevant invariant mass range. Since the PYTHIA/PHOTOS Monte Carlo gives a lowest order (LO) cross section, a K-factor must be applied to include higher-order QCD corrections. For the comparison of the dielectron invariant mass distributions, we use a mass-dependent K-factor. Since the Monte Carlo events were generated using the next-to-leading order (NLO) CTEQ6M PDF, we define the K-factor as

$$\text{K-factor} = \frac{\sigma(\alpha_s^2) \text{ with CTEQ6M}}{\sigma(\alpha_s^0) \text{ with CTEQ6M}}. \tag{8.1}$$

The cross sections are obtained from the calculation of van Neerven [8]. The van Neerven code allows evaluation of the leading order cross section, as well as the cross section to order α_s^2. The K-factor for each bin is calculated at the invariant mass equal to the average M_{ee} in the bin as calculated using the Monte Carlo. The K-factor as a function of M_{ee} is shown in Fig. 8.1. To compare the Monte Carlo to the data, Monte Carlo events must pass the acceptance cuts, and are then weighted by the M_{ee}-dependent K-factor and the total efficiency obtained from data. Figure 8.2 shows a comparison of the invariant mass distributions of Monte Carlo and data. Figure 8.3 shows the fractional difference between Monte Carlo and data as a function of M_{ee}: $(N_{data} - N_{theory})/N_{theory}$, where N is the number of events in each mass bin. Other data distributions are compared with Monte Carlo by applying the acceptance cuts, and then normalizing the Monte Carlo to the data.

The electron E_T distribution is shown in Fig. 8.4. Figure 8.5 shows the detector η distribution. The electron ϕ distribution is shown in Fig. 8.6. Figure 8.7 shows the cos θ^* distribution, where θ^* is the polar angle of the electron in the Collins-Soper frame.

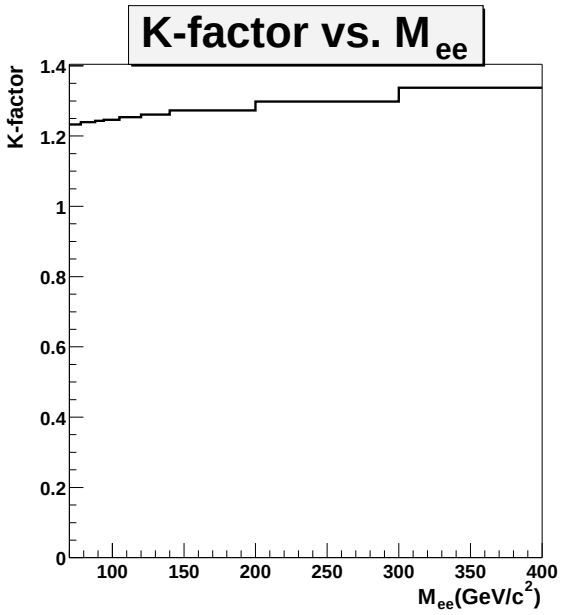

Figure 8.1: K-factor as a function of invariant mass.

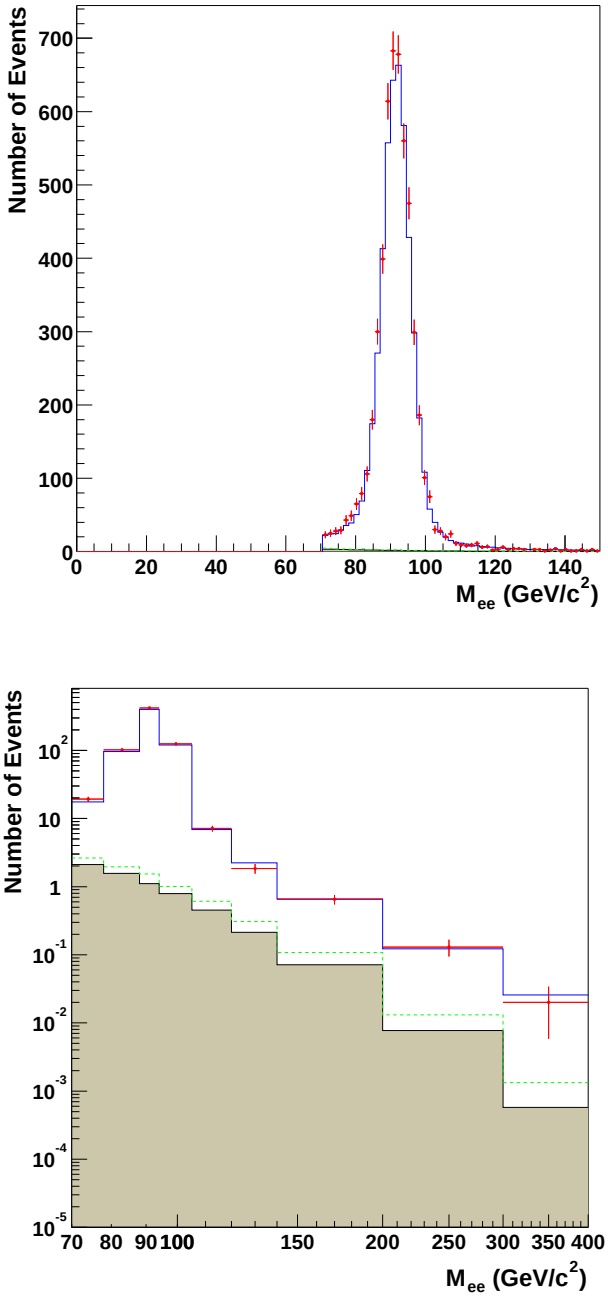

Figure 8.2: Comparison of the invariant mass distribution from data with that from Monte Carlo with linear (top) and log (bottom) axes scales. The red points are data with statistical errors only. The blue line is the sum of the Drell-Yan Monte Carlo and the total background estimate. The green dashed line is the sum of the estimated backgrounds, and the brown shaded histogram is the QCD background only.

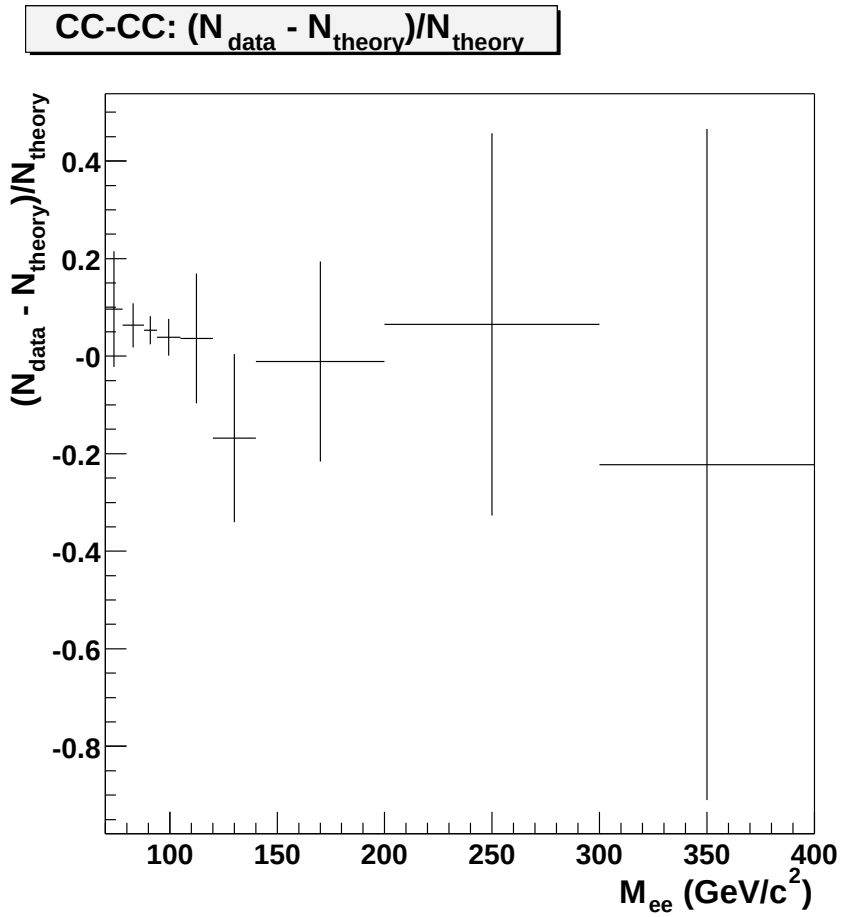

Figure 8.3: Comparison of PYTHIA/PHOTOS predictions with the data.

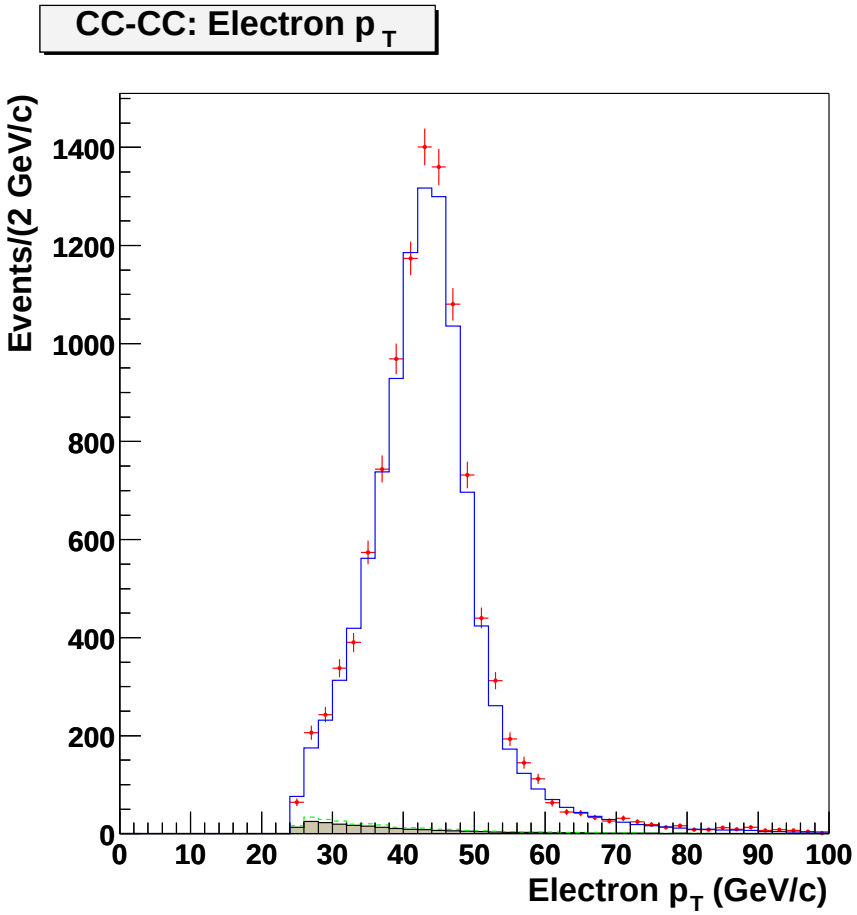

Figure 8.4: Comparison of the electron transverse momentum distribution from data with that from Monte Carlo. The red points are data with statistical errors only. The blue line is the sum of the Drell-Yan Monte Carlo and the total background estimate. The green dashed line is the sum of the estimated backgrounds, and the brown shaded histogram is the QCD background only.

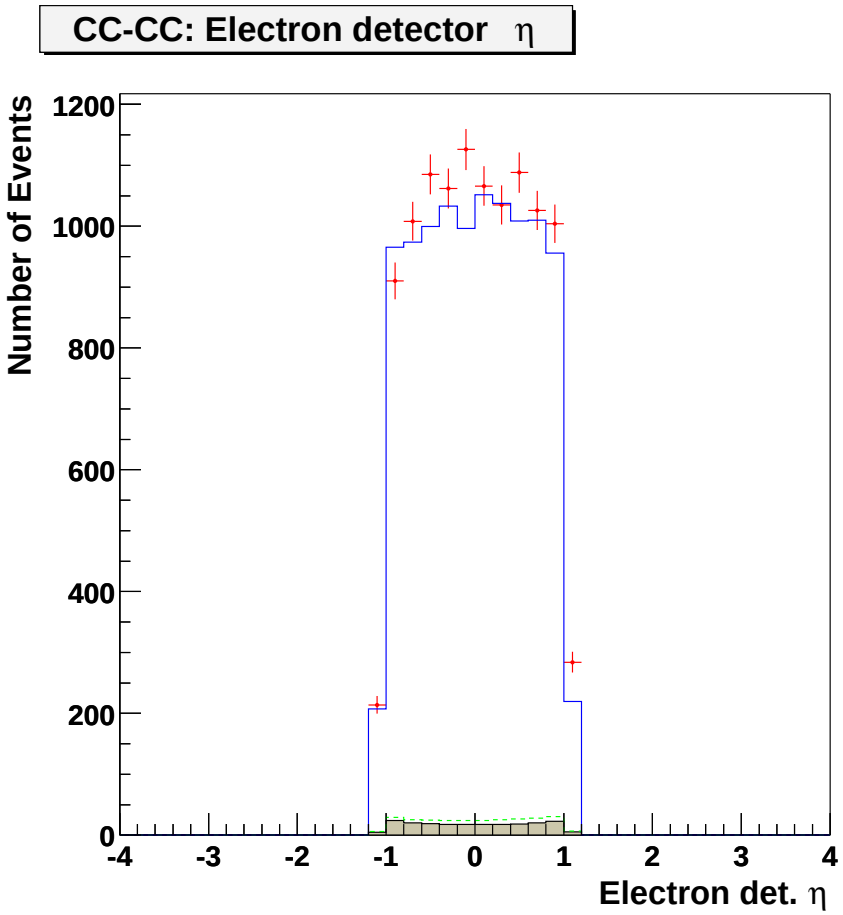

Figure 8.5: Comparison of the electron detector eta distribution from data with that from Monte Carlo. The red points are data with statistical errors only. The blue line is the sum of the Drell-Yan Monte Carlo and the total background estimate. The green dashed line is the sum of the estimated backgrounds, and the brown shaded histogram is the QCD background only.

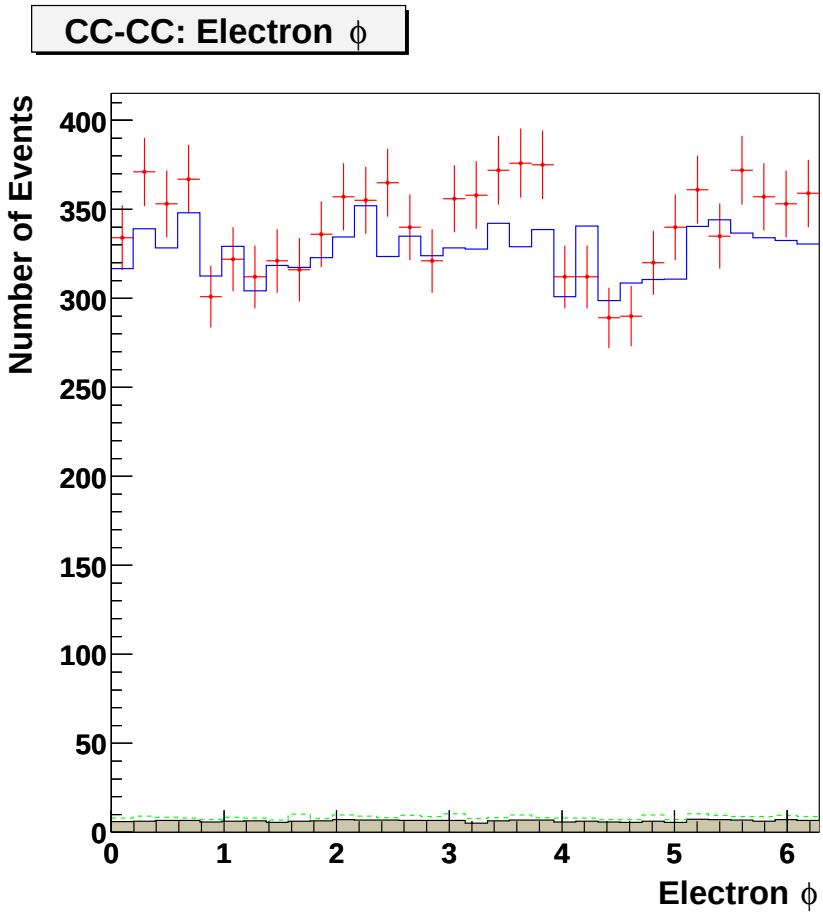

Figure 8.6: Comparison of the electron phi distribution from data with that from Monte Carlo. The red points are data with statistical errors only. The blue line is the sum of the Drell-Yan Monte Carlo and the total background estimate. The green dashed line is the sum of the estimated backgrounds, and the brown shaded histogram is the QCD background only.

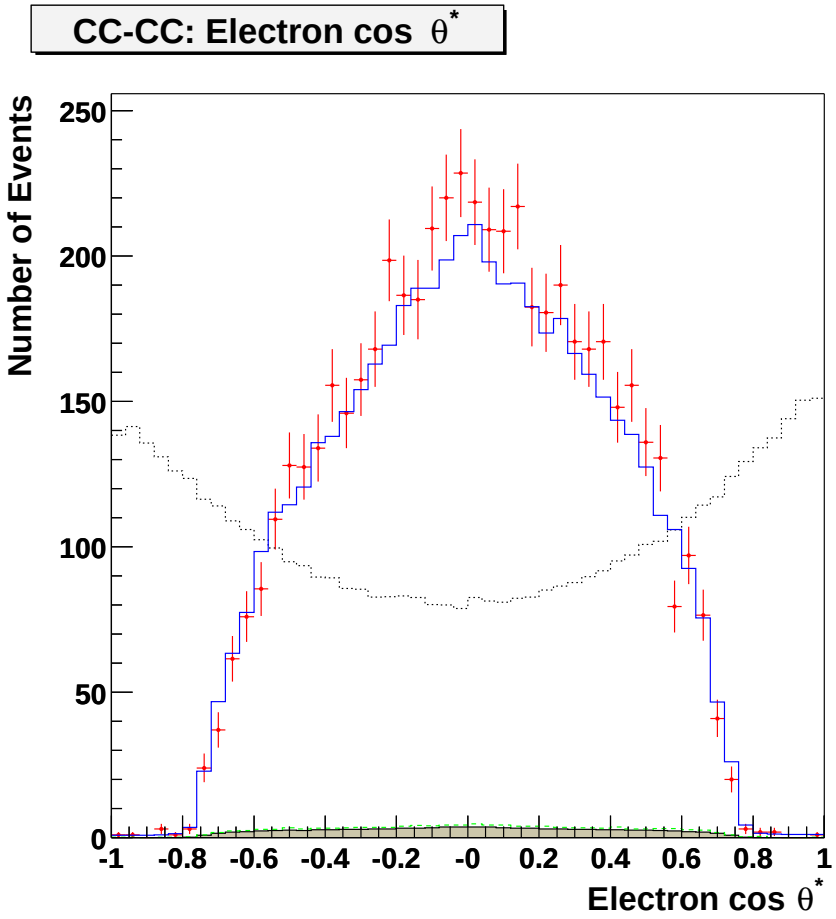

Figure 8.7: Comparison of the cos θ^* distribution from data with that from Monte Carlo. The points are data with statistical errors only, the solid line is the sum of the Drell-Yan Monte Carlo and the background estimate, the shaded histogram is the QCD background only, and the dashed histogram is the total background. The dotted histogram shows generator level distribution for the signal before selection cuts are applied.

8.1.1 Uncorrected Forward-Backward Asymmetry

In this section we compare the measured forward-backward asymmetry with predictions of the Monte Carlo simulation. The measured or "raw" asymmetry is defined by

$$A_{FB}^{raw} = \frac{(N_F - B_F) - (N_B - B_B)}{(N_F - B_F) + (N_B - B_B)}. \tag{8.2}$$

where N_F, N_B are observed number of forward and backward events in the data, and B_F, B_B are the estimated backgrounds for forward and backward events, respectively. The data are not corrected for kinematic acceptance, geometric acceptance, detector resolution, or QED radiation effects.

First we show the observed and predicted cos θ^* distributions in each e^+e^- invariant mass bin; see Figures 8.8 - 8.10. The plots show the data compared with the expectation from the sum of the Monte Carlo signal and total background estimate. Good agreement is seen between data and the SM predictions for all eleven mass regions. Also shown are the generator-level cos θ^* distributions with no kinematic or geometric acceptance cuts applied.

The raw forward-backward asymmetry from data is shown in Fig. 8.11, and is compared to the Monte Carlo prediction. Good agreement between the data and the standard model prediction is seen; the chi-square per degree of freedom is $\chi^2/dof = 1.47$.

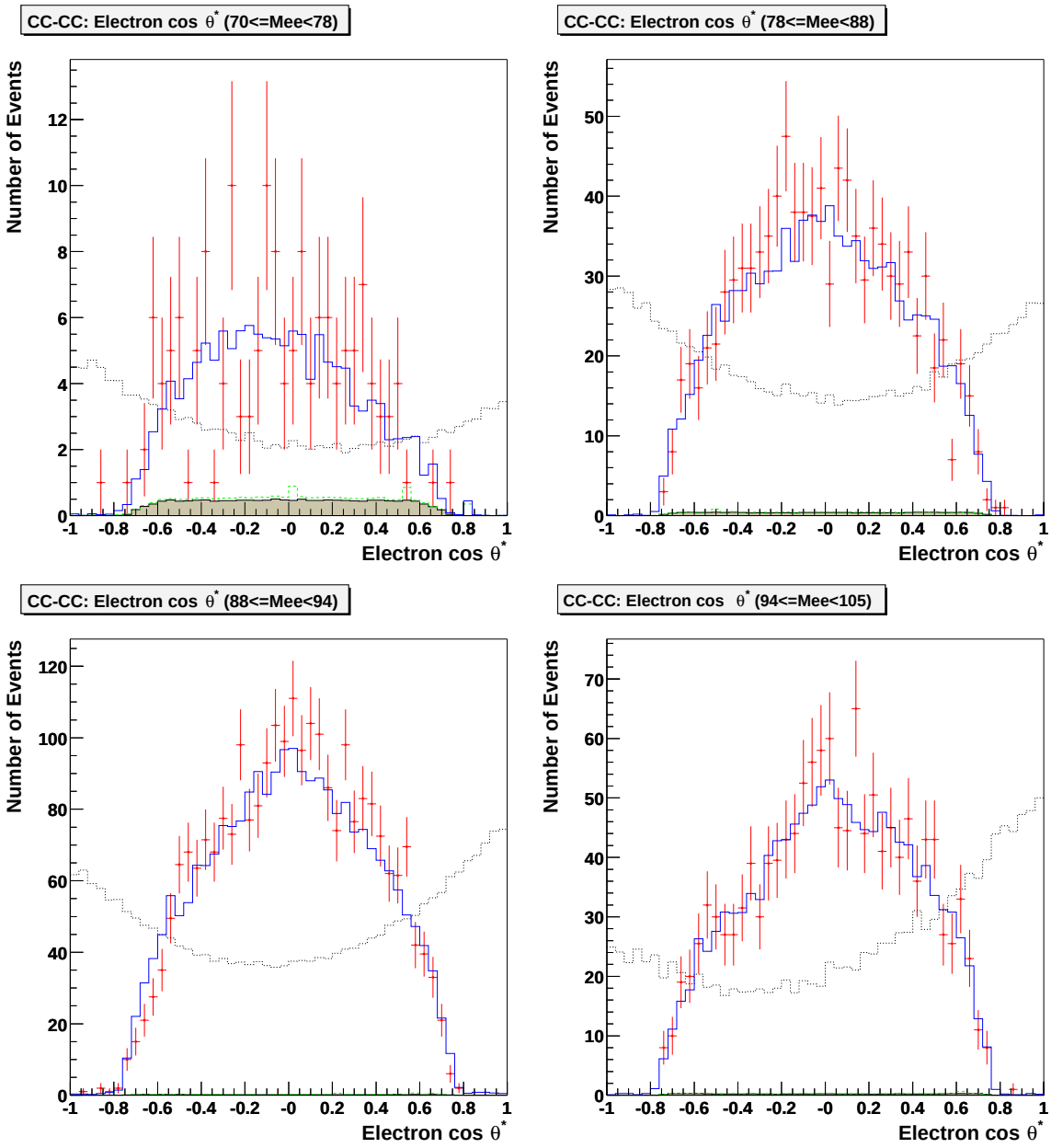

Figure 8.8: Comparisons of the cos θ^* distribution from data with that from Monte Carlo in various M_{ee} bins. The points are data with statistical errors only, the solid line is the sum of the Drell-Yan Monte Carlo and the background estimate, the shaded histogram is the QCD background only, and the dashed histogram is the total background. The dotted histogram shows generator level distribution for the signal before selection cuts are applied.

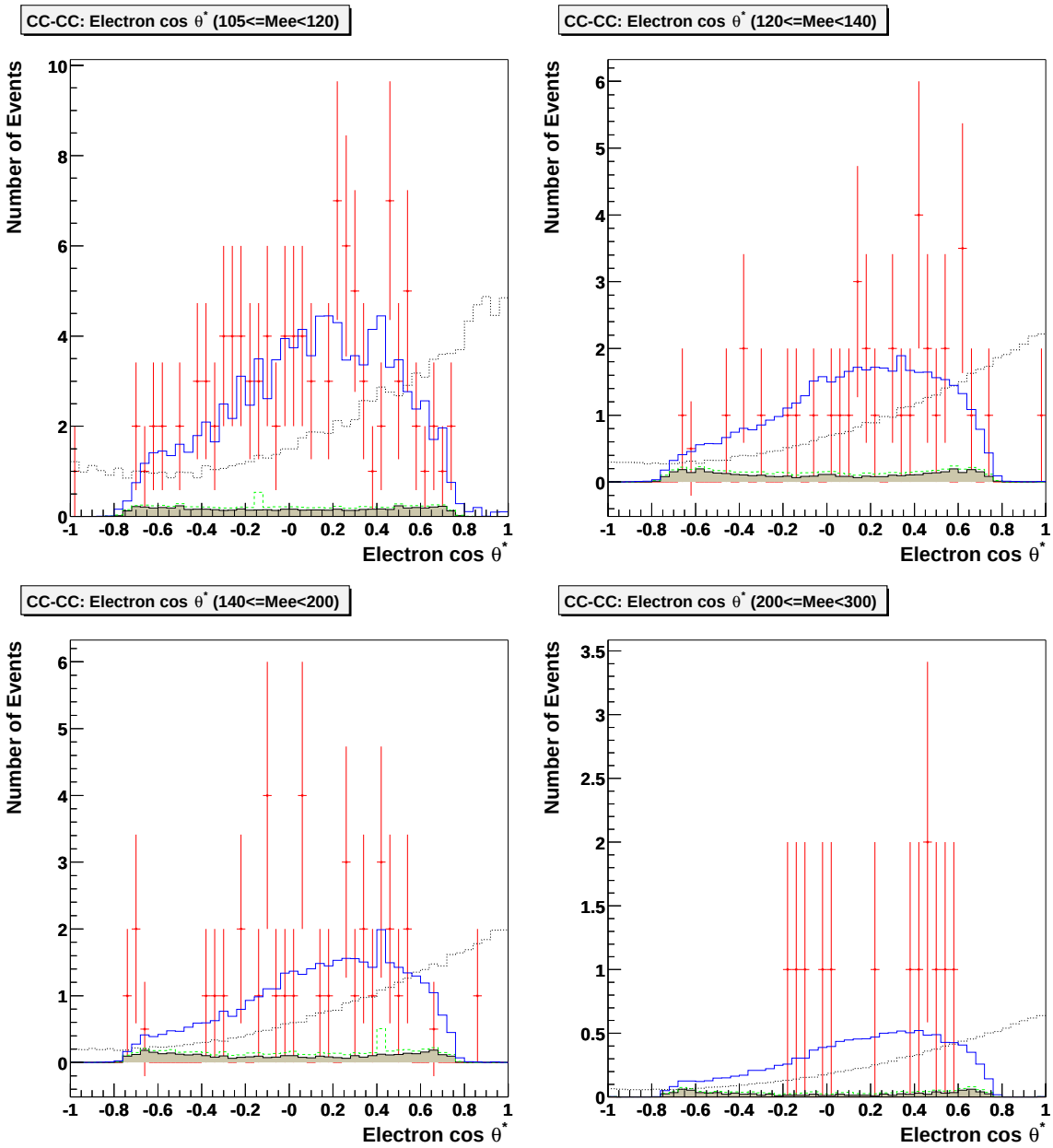

Figure 8.9: Comparisons of the cos θ^* distribution from data with that from Monte Carlo in various M_{ee} bins. The points are data with statistical errors only, the solid line is the sum of the Drell-Yan Monte Carlo and the background estimate, the shaded histogram is the QCD background only, and the dashed histogram is the total background. The dotted histogram shows generator level distribution for the signal before selection cuts are applied.

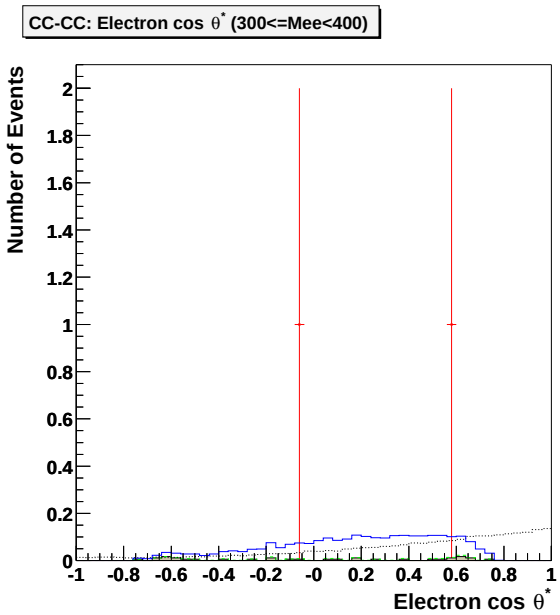

Figure 8.10: Comparisons of the cos θ^* distribution from data with that from Monte Carlo in the 300-400 GeV/c^2 M_{ee} bin. The points are data with statistical errors only, the solid line is the sum of the Drell-Yan Monte Carlo and the background estimate, the shaded histogram is the QCD background only, and the dashed histogram is the total background. The dotted histogram shows generator level distribution for the signal before selection cuts are applied.

8.2 Correction Factor

This section describes the method used to correct for kinematic cuts, geometrical acceptance, effects of the detector resolution, and QED radiation effects.

8.2.1 QED Radiative Corrections

The effect of QED radiation on the measured Drell-Yan differential cross section and forward-backward asymmetry is corrected for in order to obtain a

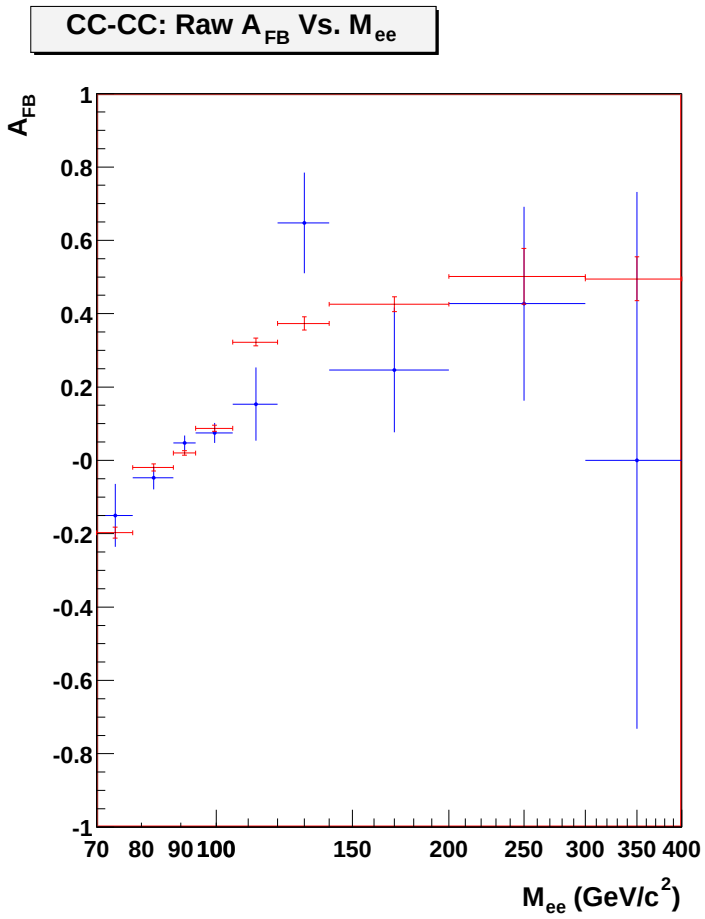

Figure 8.11: Comparison of the raw forward-backward asymmetry distribution from data with that from Monte Carlo. The blue points are data with statistical errors only, the red line is the Drell-Yan Monte Carlo.

Born-level cross section. This allows easy comparison with Born-level predictions and with results from other experiments. Purely weak corrections are very small and can be ignored [6, 57]. The largest QED corrections come from final state photon bremsstrahlung; the initial state QED corrections are negligible. $\mathcal{O}(\alpha)$ QED corrections and $\mathcal{O}(\alpha_s)$ QCD corrections are small (and have opposite sign) above the Z-peak region. QED corrections are significantly larger in the lower mass

regions 50 GeV $< M_{ee} <$ 100 GeV.

If detector effects are taken into account, the QED corrections are reduced, but are still sizable. This reduction occurs because the calorimeter has a finite resolution, and an electron and photon with a small opening angle will be measured as one EM object. The QED radiative corrections are taken into account in the correction factor. In this analysis, we correct for final state QED bremsstrahlung effects only.

8.2.2 Calculation of the Correction Factor

The Monte Carlo events described in Section 4.3 are used to obtain the correction factor. The correction factor β is calculated in bins of dielectron invariant mass and is used to correct for the kinematic cuts and geometrical acceptance, the effects of the detector resolution, and the QED correction factor. An estimate of the true invariant mass distribution is computed by multiplying each bin i of the observed experimental distribution by the ratio of the "true" to the "observed" Monte Carlo event numbers:

$$d_i^{true} = \frac{m_i}{m_i'} \cdot d_i^{obs} \equiv \frac{d_i^{obs}}{\beta_i} \tag{8.3}$$

where $\beta_i = m_i'/m_i$ is the ratio of the "observed" to the "true" Monte Carlo event numbers. We use this technique to obtain the true invariant mass distribution and

(after dividing by the efficiency and integrated luminosity) the differential cross section.

Therefore, the correction factor in each bin is defined by

$$\beta_i = \frac{m_i'}{m_i} \tag{8.4}$$

where m_i' is the number of Drell-Yan Monte Carlo events passing kinematic and acceptance cuts with reconstructed mass M_{ee} in bin i, and m_i is the number of generated Drell-Yan Monte Carlo events without final state QED radiation with generator-level mass M_{ee} in bin i.

The Monte Carlo events used to obtain the correction factor are generated in five mass regions (see Table 4.1). The events in each mass region are weighted to account for the different cross section in each range. The correction factor is calculated in each mass bin using Eq. (8.4), and the error is given by

$$\delta\beta_i = \sqrt{\frac{1}{D^2}\delta N^2 + \frac{N^2}{D^4}\delta D^2} \tag{8.5}$$

where $N \equiv m_i' = \sum_{j=1}^{5} w_j n_j$ and $D \equiv m_i = \sum_{j=1}^{5} w_j' n_j'$, n_j is the number of events in bin i from Monte Carlo event sample j, and the sum runs over all five Monte Carlo event samples. The weights are given by $w_j = (\mathcal{L} * \sigma_j)/N_j$, where σ_j and N_j are the cross section and generated number of events in the j^{th} Monte Carlo event sample.

The error on the number of events is $\delta n_j = \sqrt{n_j}$ and $\delta n_j^{'} = \sqrt{n_j^{'}}$. The kinematic and acceptance cuts applied to the events in the numerator of Eq. (8.4) are:

- 2 EM objects with
  - ID = 10 or ± 11
  - in fiducial regions
  - in CC region
  - $E_T^{smeared} > 25$ GeV/c

The correction factor for forward and backward events is shown in Fig. 8.12, and for all events in Fig. 8.13, and is used to determine the unfolded Drell-Yan differential cross section. The dip at the Z-pole is due mostly to to detector resolution effects. At high invariant mass the correction factor is smaller for forward events than for backward events because the asymmetry is large and positive in this region ($A_{FB} \approx 0.6$). This means that more events are far forward and fall outside the acceptance of the central calorimeter.

The individual effects of the geometrical acceptance, kinematic acceptance, detector resolution, and QED correction are shown in Figs. 8.14 - 8.17.

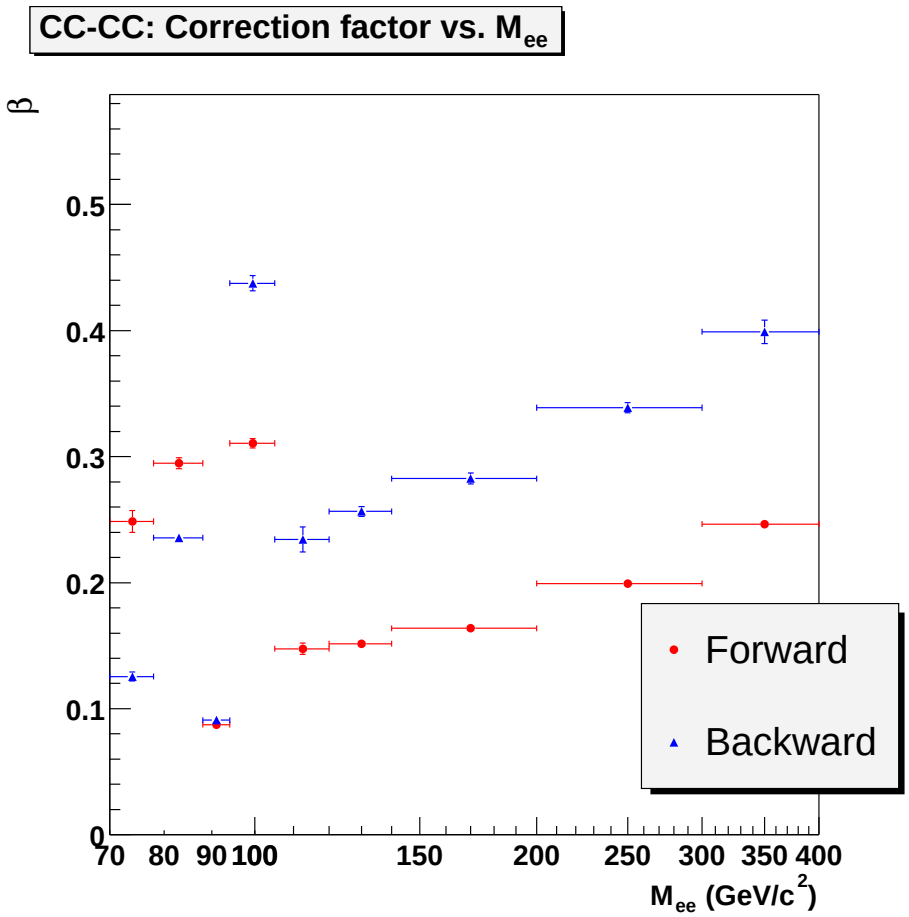

Figure 8.12: Correction factor β for forward and backward events.

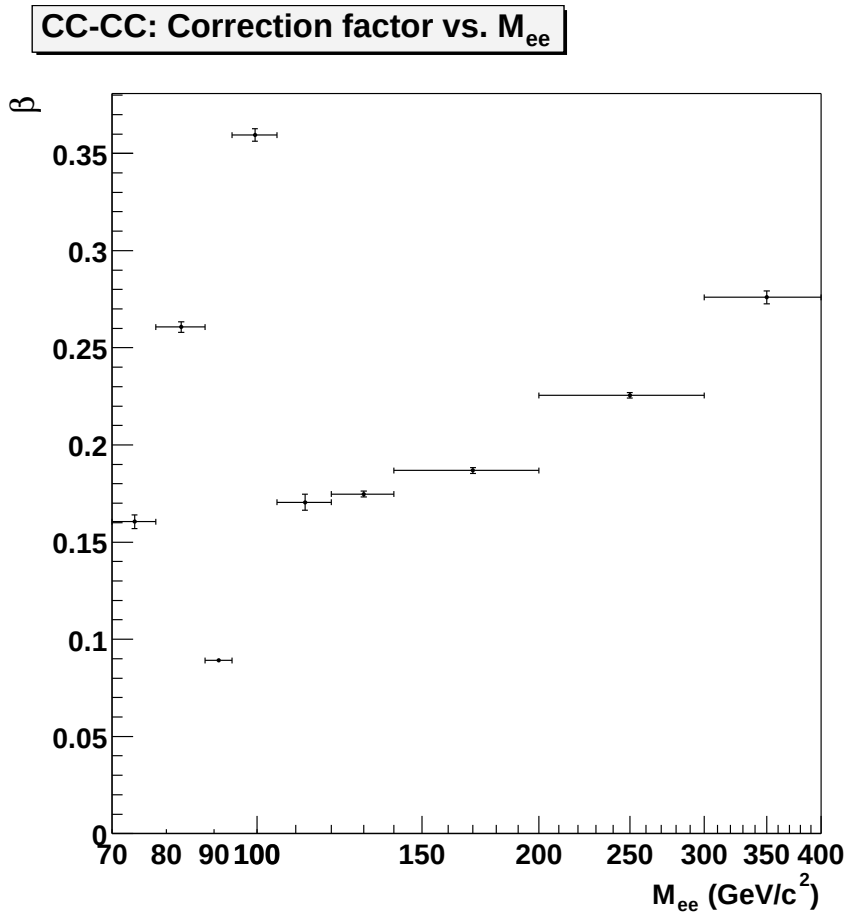

Figure 8.13: Correction factor β for all events (i.e. the sum of the forward and backward events).

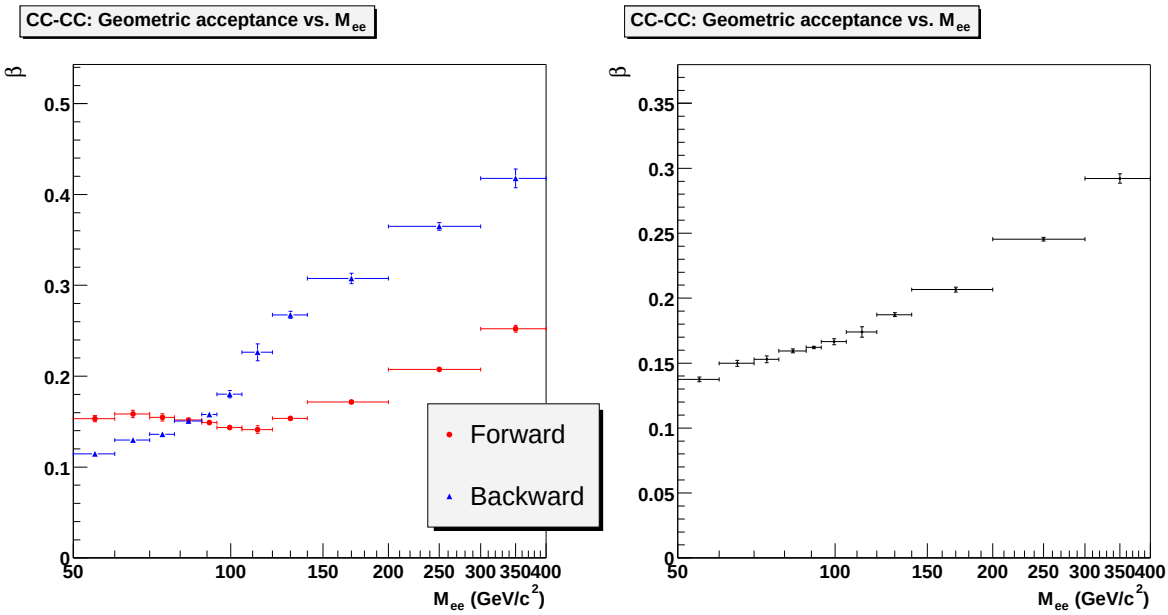

Figure 8.14: Geometric acceptance vs. e^+e^- invariant mass, shown for forward and backward events (left) and for all events (right).

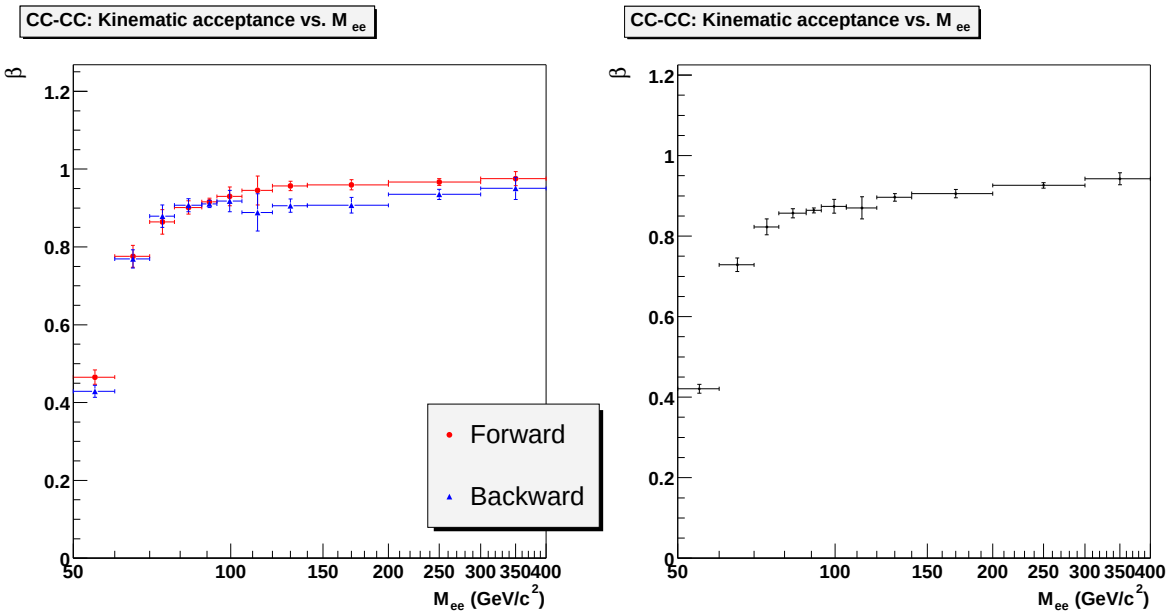

Figure 8.15: Kinematic acceptance vs. M_{ee} (calculated after geometric cuts are applied), shown for forward and backward events (left) and for all events (right).

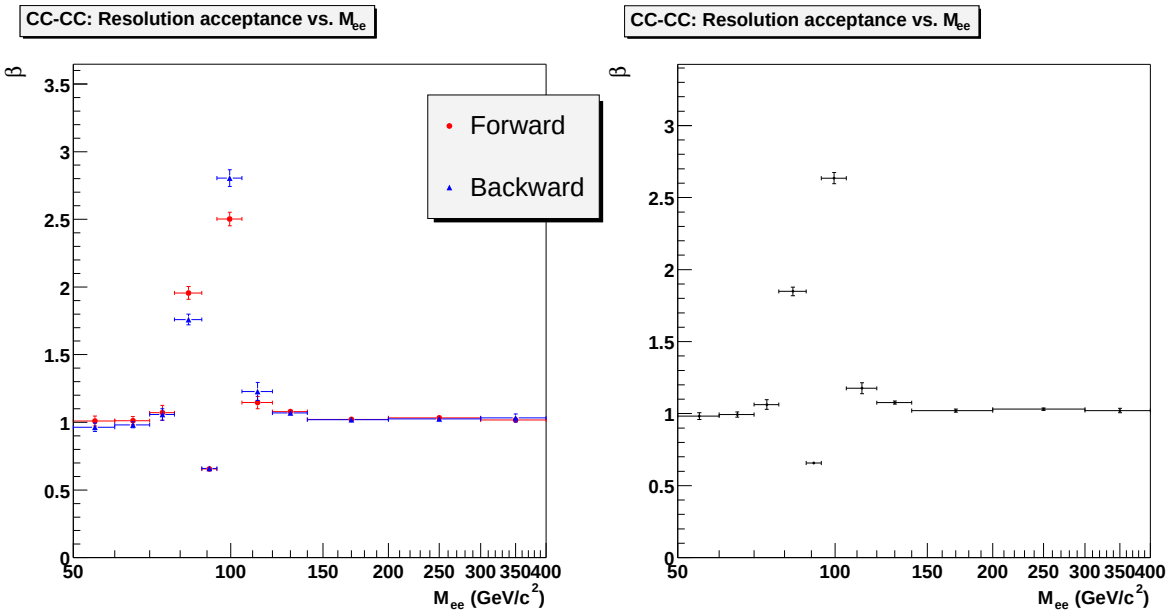

Figure 8.16: Acceptance due to detector resolution smearing (calculated with geometric and kinematic acceptance cuts applied), shown for forward and backward events (left) and for all events (right).

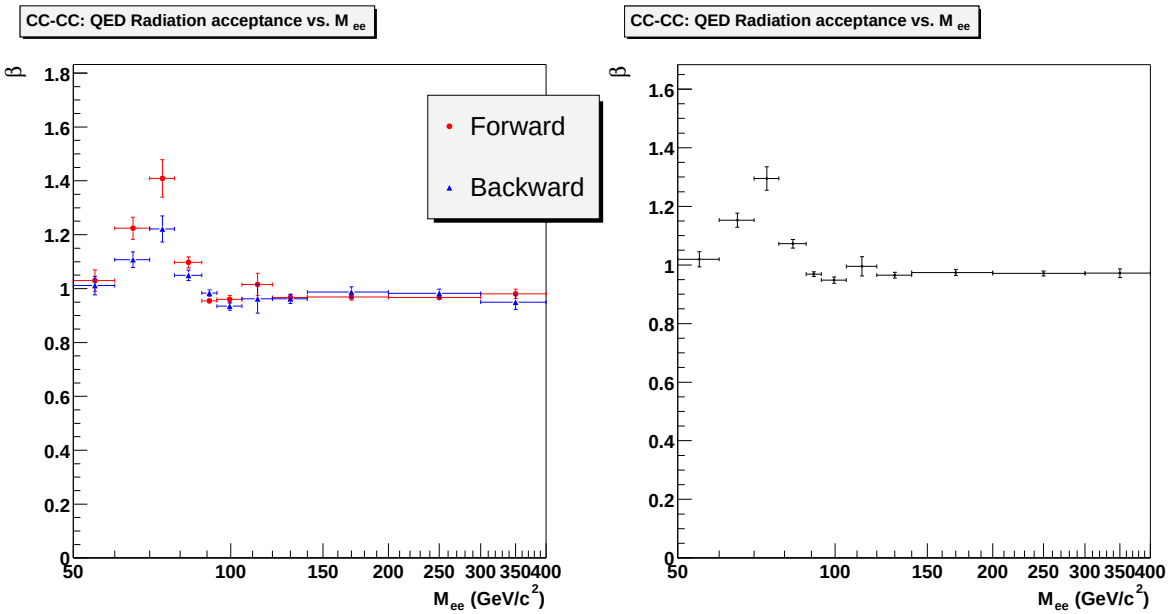

Figure 8.17: Acceptance due to QED radiation correction (calculated with geometric and kinematic acceptance cuts and detector resolution smearing applied), shown for forward and backward events (left) and for all events (right).

The systematic error in the correction factor due to the uncertainty in the PMCS parameters is determined by varying one parameter from its central value by $\pm 1\sigma$, while leaving the other parameters fixed, then re-calculating the correction factor for each mass bin. The systematic errors on the correction factor for each PMCS parameter are then $(\beta_{+1\sigma} - \beta_0)$ and $(\beta_0 - \beta_{-1\sigma})$, where β_0 is the value of β when the central value of the PMCS parameter is used. Here we have used a conservative estimate by taking the larger error as a symmetric error. Table 8.1 shows the systematic errors due to the PMCS scale parameter α for each M_{ee} bin for forward, backward, and all events, respectively. Tables 8.2 and 8.3 show the systematic errors due to the PMCS energy offset δ and constant term C in each M_{ee} bin for forward, backward, and all events.

The systematic error due to the PMCS electron-photon merging algorithm is determined by varying ΔR by ± 0.1, while leaving the other PMCS parameters fixed, then re-calculating the correction factor for each mass bin. Table 8.4 shows the systematic errors due to the PMCS ΔR parameter in M_{ee} bin for forward, backward, and all events, respectively.

The systematic error due to the PDF uncertainty is calculated using the CTEQ6 prescription [58]:

$$\delta X_{\pm} = \sum_{i=1}^{n} [X(a_i^{\pm}) - X(a_0)]^2, \tag{8.6}$$

where X is the observable (i.e. the correction factor β in our case), $X(a_i^{\pm})$ is the result for X based on the i^{th} PDF error set, and $X(a_0)$ is the result for X based on the central PDF set, CTEQ6M. For δX_+, one must sum up all the values of the observable displaced in the positive direction from the central value; and for δX_-, sum up all the values of the observable displaced in the negative direction from the central value. The correction factor is calculated for CTEQ6M and all 40 error PDFs for each mass bin using 40 Monte Carlo samples with and without QED FSR. Each sample is comprised of 150,000 events. Table 8.5 shows the PDF systematic errors for forward, backward, and all events for each mass bin.

The systematic error due to uncertainty in transverse momentum of the e^+e^- system is determined by varying the generated $p_T(e^+e^-)$ distribution in the PYTHIA event generator. We take the largest difference between the correction factor calculated with two alternatives: (a) a CDF p_T^Z-tuned PYTHIA Monte Carlo [59]; and (b) a DØ p_T^Z-tuned Monte Carlo [60]. Table 8.6 shows the systematic errors due to the $p_T(e^+e^-)$ uncertainty for each M_{ee} bin for forward, backward, and all events.

Mass Region (GeV/c^2)	σ_F^{sys}	σ_B^{sys}	σ_{ALL}^{sys}
$70 < M_{ee} < 78$	± 0.0180	± 0.0055	± 0.0077
$78 < M_{ee} < 88$	± 0.0284	± 0.0180	± 0.0223
$88 < M_{ee} < 94$	± 0.0020	± 0.0012	± 0.0012
$94 < M_{ee} < 105$	± 0.0325	± 0.0352	± 0.0336
$105 < M_{ee} < 120$	± 0.0053	± 0.0044	± 0.0040
$120 < M_{ee} < 140$	± 0.0031	± 0.0073	± 0.0029
$140 < M_{ee} < 200$	± 0.0025	± 0.0062	± 0.0026
$200 < M_{ee} < 300$	± 0.0030	± 0.0037	± 0.0032
$300 < M_{ee} < 400$	± 0.0040	± 0.0087	± 0.0042

Table 8.1: Systematic error in correction factor β due to EM energy scale parameter. Errors are shown separately for forward, backward, and all events.

Mass Region (GeV/c^2)	σ_F^{sys}	σ_B^{sys}	σ_{ALL}^{sys}
$70 < M_{ee} < 78$	± 0.0162	± 0.0042	± 0.0016
$78 < M_{ee} < 88$	± 0.0114	± 0.0081	± 0.0053
$88 < M_{ee} < 94$	± 0.0021	± 0.0009	± 0.0009
$94 < M_{ee} < 105$	± 0.0140	± 0.0114	± 0.0130
$105 < M_{ee} < 120$	± 0.0034	± 0.0082	± 0.0036
$120 < M_{ee} < 140$	± 0.0004	± 0.0067	± 0.0015
$140 < M_{ee} < 200$	± 0.0015	± 0.0031	± 0.0015
$200 < M_{ee} < 300$	± 0.0013	± 0.0061	± 0.0022
$300 < M_{ee} < 400$	± 0.0038	± 0.0042	± 0.0039

Table 8.2: Systematic error in correction factor β due to EM energy offset parameter. Errors are shown separately for forward, backward, and all events.

Mass Region (GeV/c^2)	σ_F^{sys}	σ_B^{sys}	σ_{ALL}^{sys}
$70 < M_{ee} < 78$	± 0.0238	± 0.0044	± 0.0036
$78 < M_{ee} < 88$	± 0.0207	± 0.0082	± 0.0076
$88 < M_{ee} < 94$	± 0.0035	± 0.0029	± 0.0025
$94 < M_{ee} < 105$	± 0.0063	± 0.0067	± 0.0044
$105 < M_{ee} < 120$	± 0.0032	± 0.0099	± 0.0028
$120 < M_{ee} < 140$	± 0.0014	± 0.0055	± 0.0023
$140 < M_{ee} < 200$	± 0.0008	± 0.0019	± 0.0010
$200 < M_{ee} < 300$	± 0.0012	± 0.0032	± 0.0012
$300 < M_{ee} < 400$	± 0.0020	± 0.0055	± 0.0017

Table 8.3: Systematic error in correction factor β due to EM energy resolution constant term. Errors are shown separately for forward, backward, and all events.

Mass Region (GeV/c^2)	σ_F^{sys}	σ_B^{sys}	σ_{ALL}^{sys}
$70 < M_{ee} < 78$	± 0.0243	± 0.0037	± 0.0059
$78 < M_{ee} < 88$	± 0.0182	± 0.0033	± 0.0077
$88 < M_{ee} < 94$	± 0.0031	± 0.0017	± 0.0017
$94 < M_{ee} < 105$	± 0.0070	± 0.0044	± 0.0044
$105 < M_{ee} < 120$	± 0.0028	± 0.0106	± 0.0039
$120 < M_{ee} < 140$	± 0.0018	± 0.0019	± 0.0018
$140 < M_{ee} < 200$	± 0.0015	± 0.0038	± 0.0020
$200 < M_{ee} < 300$	± 0.0021	± 0.0044	± 0.0021
$300 < M_{ee} < 400$	± 0.0051	± 0.0065	± 0.0047

Table 8.4: Systematic error in correction factor β due to electron-photon merging parameter. Errors are shown separately for forward, backward, and all events.

Mass Region (GeV/c^2)	σ_F^{sys}	σ_B^{sys}	σ_{ALL}^{sys}
$70 < M_{ee} < 78$	$^{+0.00100}_{-0.01136}$	$^{+0.00149}_{-0.00056}$	$^{+0.00036}_{-0.00119}$
$78 < M_{ee} < 88$	$^{+0.00418}_{-0.00001}$	$^{+0.00022}_{-0.00092}$	$^{+0.00052}_{-0.00006}$
$88 < M_{ee} < 94$	$^{+0.00001}_{-0.00007}$	$^{+0.00003}_{-0.00002}$	$^{+0.000005}_{-0.00003}$
$94 < M_{ee} < 105$	$^{+0.00188}_{-0.00028}$	$^{+0.00055}_{-0.00483}$	$^{+0.00073}_{-0.00046}$
$105 < M_{ee} < 120$	$^{+0.00355}_{-0.00004}$	$^{+0.01461}_{-0.00067}$	$^{+0.00506}_{-0.00001}$
$120 < M_{ee} < 140$	$^{+0.000004}_{-0.00043}$	$^{+0.00013}_{-0.00087}$	$^{+0.00000}_{-0.00049}$
$140 < M_{ee} < 200$	$^{+0.00008}_{-0.00007}$	$^{+0.00110}_{-0.00027}$	$^{+0.00009}_{-0.00006}$
$200 < M_{ee} < 300$	$^{+0.00012}_{-0.00004}$	$^{+0.00127}_{-0.00004}$	$^{+0.00020}_{-0.00001}$
$300 < M_{ee} < 400$	$^{+0.00001}_{-0.00098}$	$^{+0.00226}_{-0.00065}$	$^{+0.00005}_{-0.00069}$

Table 8.5: Systematic error in correction factor β due to PDF uncertainty. Errors are shown separately for forward, backward, and all events.

Mass Region (GeV/c^2)	σ_F^{sys}	σ_B^{sys}	σ_{ALL}^{sys}
$70 < M_{ee} < 78$	± 0.0018	± 0.0021	± 0.0018
$78 < M_{ee} < 88$	± 0.0063	± 0.0028	± 0.0008
$88 < M_{ee} < 94$	± 0.0012	± 0.0005	± 0.0007
$94 < M_{ee} < 105$	± 0.0028	± 0.0085	± 0.0008
$105 < M_{ee} < 120$	± 0.0088	± 0.0010	± 0.0072
$120 < M_{ee} < 140$	± 0.0025	± 0.0039	± 0.0021
$140 < M_{ee} < 200$	± 0.0006	± 0.0028	± 0.0007
$200 < M_{ee} < 300$	± 0.0020	± 0.0034	± 0.0022
$300 < M_{ee} < 400$	± 0.0052	± 0.0072	± 0.0054

Table 8.6: Systematic error in correction factor β due to uncertainty in the $p_T(e^+e^-)$ distribution. Errors are shown separately for forward, backward, and all events.

8.3 Drell-Yan Differential Cross Section

The differential cross section is calculated by correcting the background-subtracted signal in each M_{ee} bin by the efficiency, correction factor, and integrated luminosity:

$$\frac{d\sigma}{dM} = \frac{N - B}{\epsilon\beta\mathcal{L}\Delta M}, \tag{8.7}$$

where

N = number of observed events in bin i

B = estimate of background in bin i

ϵ = total event selection efficiency (trigger, EM-id, and track match) in bin i

β = correction factor for acceptance, detector resolution, and QED radiative corrections in bin i

$\mathcal{L}$ = integrated luminosity

ΔM = bin width

The combined efficiency is given by

$$\epsilon_{tot} = \epsilon_{trig}^{CC-CC} \cdot \epsilon_{EM}^{CC} \cdot \epsilon_{EM}^{CC} \cdot (1 - (1 - \epsilon_{trk}^{CC})^2). \tag{8.8}$$

The resulting differential cross section $d\sigma/dM$ is shown in Fig. 8.18. The data is compared with the average theoretical cross section in each bin, obtained from the calculation of Ref. [8] using the CTEQ6 parton distribution functions. Table 8.7 summarizes the input values used to calculate the differential cross section. A breakdown of the systematic errors is given in Table 8.8.

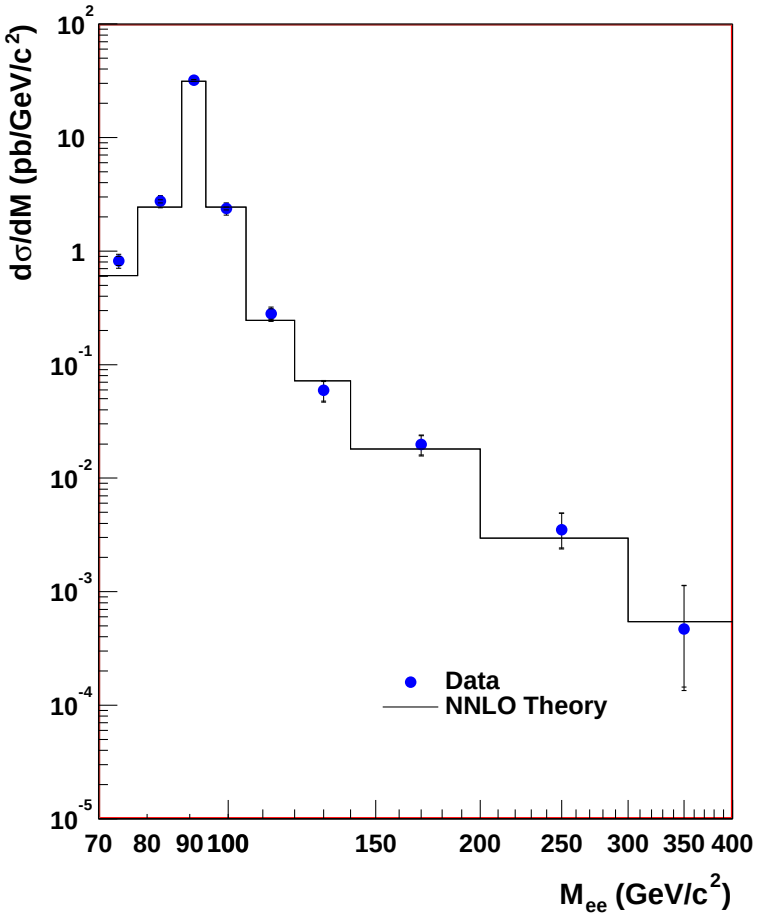

Figure 8.18: Drell-Yan differential cross sections for the CC-CC region. The blue circles are the data with the error bars representing the total uncertainty (outer error bars) and the statistical uncertainty only (inner error bars). For reference, the solid black line is a NNLO Monte Carlo calculation.

Source	Value	Statistical Error	Systematic Error
Number of Events	5259	73	
Background	84.0	5.9	
PMCS Parameters			
- Scale CC	1.006	0.003	per M_{ee} bin
- Offset CC	0.064	0.045	per M_{ee} bin
- Constant CC	0.045	0.002	per M_{ee} bin
Fake Rate CC	0.016	0.0001	0.002 $(*)$
Trigger Eff. CC-CC	1.0000	$^{+0.0000}_{-0.0002}$	$^{+0.0000}_{-0.0006}$ $(*)$
EM-id Eff. CC	per M_{ee} bin	per M_{ee} bin	per M_{ee} bin
Track Match Eff. CC	per M_{ee} bin	per M_{ee} bin	per M_{ee} bin
Charge Misid Prob. CC	per M_{ee} bin	per M_{ee} bin	per M_{ee} bin
Luminosity	177.3	11.5	
PDF			per M_{ee} bin

Table 8.7: Values used in the calculation of the cross section. $(*)$ are systematic errors taken from [53].

Mass Bin (GeV/c^2)	σ_{bkgd}	σ_ϵ	σ_β	σ_{PDF}
$70 - 78$	0.018987	$^{+0.034474}_{-0.038462}$	0.057363	$^{+0.001850}_{-0.006075}$
$78 - 88$	0.007963	$^{+0.052220}_{-0.053753}$	0.268493	$^{+0.005497}_{-0.000633}$
$88 - 94$	0.023673	$^{+0.482433}_{-0.485992}$	1.241734	$^{+0.001647}_{-0.009952}$
$94 - 105$	0.003442	$^{+0.039417}_{-0.040043}$	0.241762	$^{+0.004791}_{-0.003007}$
$105 - 120$	0.005234	$^{+0.010164}_{-0.011586}$	0.018028	$^{+0.008325}_{-0.000008}$
$120 - 140$	0.002951	$^{+0.001154}_{-0.001224}$	0.001734	$^{+0.000000}_{-0.000168}$
$140 - 200$	0.001003	$^{+0.000338}_{-0.000346}$	0.000429	$^{+0.000009}_{-0.000007}$
$200 - 300$	0.000234	$^{+0.000057}_{-0.000058}$	0.000082	$^{+0.000003}_{-0.000000}$
$300 - 400$	0.000073	$^{+0.000009}_{-0.000009}$	0.000017	$^{+0.000000}_{-0.000001}$

Table 8.8: Contributions to the systematic error on the differential cross section measurement from uncertainties in the background (σ_{bkgd}), signal selection efficiency (σ_ϵ), correction factor (σ_β), and parton distribution functions (σ_{PDF}). Units are $\mathrm{pb}/(\mathrm{GeV}/c^2)$.

The differential cross sections for forward and backward events are calculated using the same methodology as above, but for events in which the electron angle satisfies $\cos\theta^* > 0$ and $\cos\theta^* < 0$, respectively. For events with only one track match, the EM candidate with a track match is used to determine the charge. A negative charge indicates an electron, while if the charge is positive the other EM object in the event is assumed to be the electron. Figures 8.19 and 8.20 show the forward and backward differential Drell-Yan cross sections ($d\sigma_F/dM$ and $d\sigma_B/dM$, respectively). A breakdown of the systematic errors is given in Tables 8.9-8.10. The results for the differential cross sections are summarized in Tables 8.11-8.13.

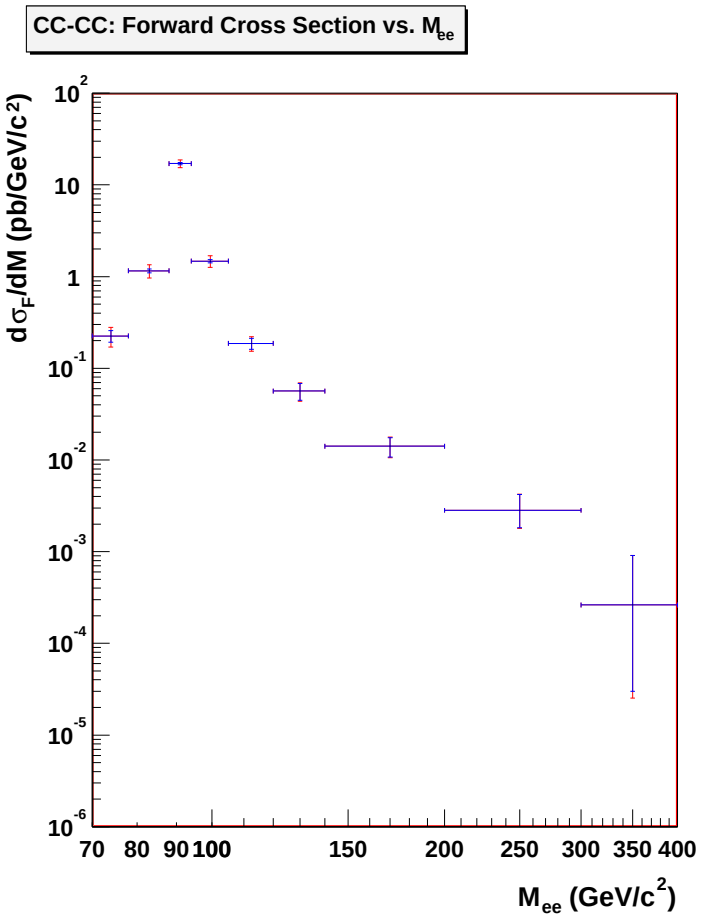

Figure 8.19: Forward Drell-Yan differential cross section. The red (outer) error bar is the total error and the blue (inner) error bar is just the statistical error.

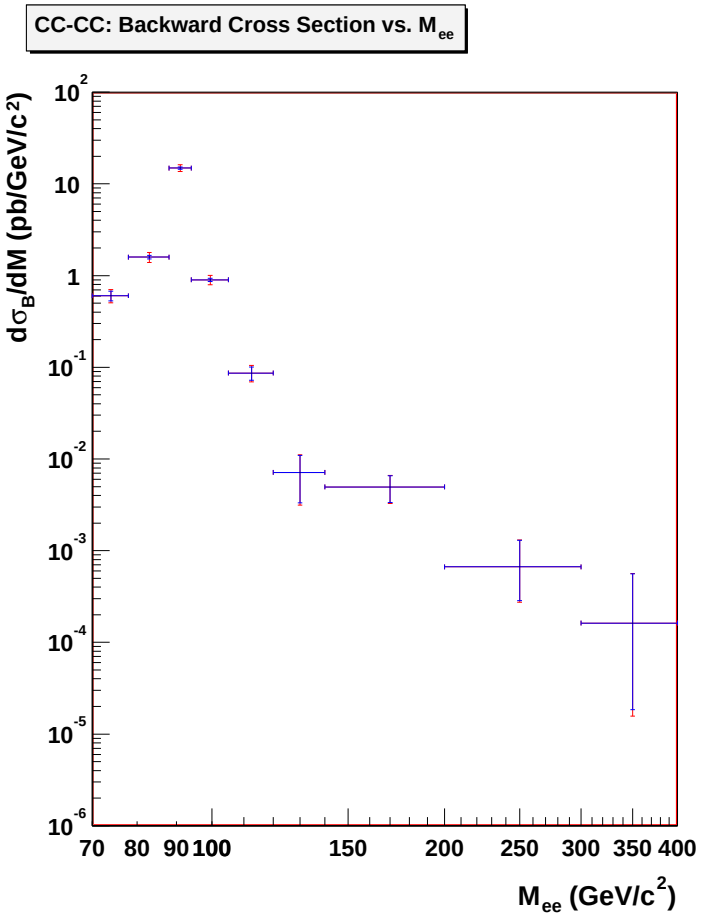

Figure 8.20: Backward Drell-Yan differential cross section. The red (outer) error bar is the total error and the blue (inner) error bar is just the statistical error.

Mass Bin (GeV/c^2)	σ_{bkgd}	σ_ϵ	σ_β	σ_{PDF}
$70-78$	0.006134	$^{+0.009459}_{-0.010553}$	0.038677	$^{+0.000910}_{-0.010297}$
$78-88$	0.003525	$^{+0.021981}_{-0.022627}$	0.164388	$^{+0.016399}_{-0.000027}$
$88-94$	0.012104	$^{+0.257892}_{-0.259795}$	1.109641	$^{+0.001406}_{-0.014299}$
$94-105$	0.001997	$^{+0.024510}_{-0.024900}$	0.175097	$^{+0.008901}_{-0.001320}$
$105-120$	0.003034	$^{+0.006771}_{-0.007718}$	0.015754	$^{+0.004501}_{-0.000056}$
$120-140$	0.001706	$^{+0.001096}_{-0.001162}$	0.001803	$^{+0.000002}_{-0.000161}$
$140-200$	0.000574	$^{+0.000240}_{-0.000246}$	0.000324	$^{+0.000007}_{-0.000006}$
$200-300$	0.000133	$^{+0.000046}_{-0.000047}$	0.000068	$^{+0.000002}_{-0.000001}$
$300-400$	0.000041	$^{+0.000005}_{-0.000005}$	0.000011	$^{+0.000000}_{-0.000001}$

Table 8.9: Contributions to the systematic error on the forward differential cross section measurement from uncertainties in the background (σ_{bkgd}), signal selection efficiency (σ_ϵ), correction factor (σ_β), and parton distribution functions (σ_{PDF}). Units are pb/(GeV/c^2).

Mass Bin (GeV/c^2)	σ_{bkgd}	σ_ϵ	σ_β	σ_{PDF}
$70 - 78$	0.012196	$^{+0.025353}_{-0.028286}$	0.047776	$^{+0.007182}_{-0.002697}$
$78 - 88$	0.004424	$^{+0.030267}_{-0.031156}$	0.149201	$^{+0.001497}_{-0.006237}$
$88 - 94$	0.011659	$^{+0.225322}_{-0.226985}$	0.616705	$^{+0.005328}_{-0.003754}$
$94 - 105$	0.001420	$^{+0.014979}_{-0.015217}$	0.080769	$^{+0.001140}_{-0.009935}$
$105 - 120$	0.001910	$^{+0.003132}_{-0.003570}$	0.007317	$^{+0.005392}_{-0.000245}$
$120 - 140$	0.001008	$^{+0.000138}_{-0.000147}$	0.000355	$^{+0.000004}_{-0.000024}$
$140 - 200$	0.000333	$^{+0.000084}_{-0.000086}$	0.000169	$^{+0.000019}_{-0.000005}$
$200 - 300$	0.000078	$^{+0.000011}_{-0.000011}$	0.000021	$^{+0.000002}_{-0.000000}$
$300 - 400$	0.000025	$^{+0.000003}_{-0.000003}$	0.000007	$^{+0.000001}_{-0.000000}$

Table 8.10: Contributions to the systematic error on the backward differential cross section measurement from uncertainties in the background (σ_{bkgd}), signal selection efficiency (σ_ϵ), correction factor (σ_β), and parton distribution functions (σ_{PDF}). Units are pb/(GeV/c^2).

Mass Bin (GeV/c^2)	$\overline{M_{ee}}$ (GeV/c^2)	N	B	$\epsilon\beta$	$d\sigma_{ee}/dM$ (pb / GeV/c^2)
70 − 78	74.6	154	21.1	0.114	$0.8209 \pm 0.0766(\mathrm{stat.})\ ^{+0.0696}_{-0.0716}(\mathrm{sys.})\ ^{+0.0018}_{-0.0061}(\mathrm{pdf})$
78 − 88	84.5	1022	19.5	0.206	$2.7468 \pm 0.0876(\mathrm{stat.})\ ^{+0.2736}_{-0.2739}(\mathrm{sys.})\ ^{+0.0055}_{-0.0006}(\mathrm{pdf})$
88 − 94	89.9,92.5	2522	9.2	0.074	$31.9070 \pm 0.6377(\mathrm{stat.})\ ^{+1.3324}_{-1.3337}(\mathrm{sys.})\ ^{+0.0016}_{-0.0100}(\mathrm{pdf})$
94 − 105	97.4	1363	11.1	0.293	$2.3683 \pm 0.0647(\mathrm{stat.})\ ^{+0.2450}_{-0.2451}(\mathrm{sys.})\ ^{+0.0048}_{-0.0030}(\mathrm{pdf})$
Mass Bin (GeV/c^2)	$\overline{M_{ee}}$ (GeV/c^2)	N	B	$\epsilon\beta$	$d\sigma_{ee}/dM$ (fb / GeV/c^2)
105 − 120	111.1	107	9.1	0.131	$280.55 \pm 29.65(\mathrm{stat.})\ ^{+21.35}_{-22.06}(\mathrm{sys.})\ ^{+8.32}_{-0.01}(\mathrm{pdf})$
120 − 140	128.7	37	6.1	0.146	$59.48 \pm 11.71(\mathrm{stat.})\ ^{+3.61}_{-3.63}(\mathrm{sys.})\ ^{+0.00}_{-0.17}(\mathrm{pdf})$
140 − 200	164.1	39	6.5	0.154	$19.87 \pm 3.82(\mathrm{stat.})\ ^{+1.14}_{-1.14}(\mathrm{sys.})\ ^{+0.01}_{-0.01}(\mathrm{pdf})$
200 − 300	240.7	13	1.3	0.188	$3.50 \pm\ ^{+1.41}_{-1.07}(\mathrm{stat.})\ ^{+0.25}_{-0.25}(\mathrm{sys.})\ ^{+0.00}_{-0.00}(\mathrm{pdf})$
300 − 400	343.3	2	0.1	0.225	$0.47 \pm\ ^{+0.66}_{-0.32}(\mathrm{stat.})\ ^{+0.08}_{-0.08}(\mathrm{sys.})\ ^{+0.00}_{-0.00}(\mathrm{pdf})$

Table 8.11: Results for the Drell-Yan differential cross section $d\sigma_{ee}/dM$. N is the number of data events, B is the background estimate, $\epsilon\beta$ is the combined efficiency times correction factor. There is an overall fractional uncertainty of 6.5% from the uncertainty in the integrated luminosity. $\overline{M_{ee}}$ is the value of M_{ee} for which the differential cross section is equal to its average value over the bin as determined from the theoretical prediction.

Mass Bin (GeV/c^2)	$\overline{M_{ee}}$ (GeV/c^2)	N	B	$\epsilon\beta$	$d\sigma^F_{ee}/dM$ (pb / GeV/c^2)
70 − 78	74.6	67	10.5	0.177	$0.2252 \pm 0.0326(\mathrm{stat.})\ ^{+0.0403}_{-0.0406}(\mathrm{sys.})\ ^{+0.0009}_{-0.0103}(\mathrm{pdf})$
78 − 88	84.5	487	9.7	0.233	$1.1563 \pm 0.0535(\mathrm{stat.})\ ^{+0.1659}_{-0.1660}(\mathrm{sys.})\ ^{+0.0164}_{-0.0000}(\mathrm{pdf})$
88 − 94	92.5	1321	4.6	0.073	$17.0564 \pm 0.4710(\mathrm{stat.})\ ^{+1.1393}_{-1.1397}(\mathrm{sys.})\ ^{+0.0014}_{-0.0143}(\mathrm{pdf})$
94 − 105	97.4	732	5.5	0.253	$1.4726 \pm 0.0548(\mathrm{stat.})\ ^{+0.1768}_{-0.1769}(\mathrm{sys.})\ ^{+0.0089}_{-0.0013}(\mathrm{pdf})$
Mass Bin (GeV/c^2)	$\overline{M_{ee}}$ (GeV/c^2)	N	B	$\epsilon\beta$	$d\sigma^F_{ee}/dM$ (fb / GeV/c^2)
105 − 120	111.1	61	4.6	0.114	$186.90 \pm 25.86(\mathrm{stat.})\ ^{+17.41}_{-17.80}(\mathrm{sys.})\ ^{+4.50}_{-0.06}(\mathrm{pdf})$
120 − 140	128.7	29	3.1	0.127	$56.48 \pm 11.85(\mathrm{stat.})\ ^{+2.71}_{-2.74}(\mathrm{sys.})\ ^{+0.00}_{-0.16}(\mathrm{pdf})$
140 − 200	164.1	24	3.2	0.135	$14.13\ ^{+3.38}_{-3.38}(\mathrm{stat.})\ ^{+0.70}_{-0.70}(\mathrm{sys.})\ ^{+0.01}_{-0.01}(\mathrm{pdf})$
200 − 300	240.7	9	0.7	0.166	$2.83\ ^{+1.39}_{-1.00}(\mathrm{stat.})\ ^{+0.16}_{-0.16}(\mathrm{sys.})\ ^{+0.00}_{-0.00}(\mathrm{pdf})$
300 − 400	343.3	1	0.1	0.201	$0.26\ ^{+0.65}_{-0.23}(\mathrm{stat.})\ ^{+0.04}_{-0.04}(\mathrm{sys.})\ ^{+0.00}_{-0.00}(\mathrm{pdf})$

Table 8.12: Results for the forward Drell-Yan differential cross section $d\sigma^F_{ee}/dM$. N is the number of data events, B is the background estimate, $\epsilon\beta$ is the combined efficiency times correction factor. There is an overall fractional uncertainty of 6.5% from the uncertainty in the integrated luminosity. $\overline{M_{ee}}$ is the value of M_{ee} for which the differential cross section is equal to its average value over the bin as determined from the theoretical prediction.

Mass Bin (GeV/c^2)	$\overline{M_{ee}}$ (GeV/c^2)	N	B	$\epsilon\beta$	$d\sigma^B_{ee}/dM$ (pb / GeV/c^2)
70 − 78	74.6	87	10.6	0.089	$0.6037 \pm 0.0737(\mathrm{stat.})\ ^{+0.0554}_{-0.0568}(\mathrm{sys.})\ ^{+0.0072}_{-0.0027}(\mathrm{pdf})$
78 − 88	84.5	535	9.8	0.186	$1.5921 \pm 0.0701(\mathrm{stat.})\ ^{+0.1523}_{-0.1525}(\mathrm{sys.})\ ^{+0.0015}_{-0.0062}(\mathrm{pdf})$
88 − 94	92.5	1202	4.6	0.076	$14.9023 \pm 0.4316(\mathrm{stat.})\ ^{+0.6567}_{-0.6573}(\mathrm{sys.})\ ^{+0.0053}_{-0.0038}(\mathrm{pdf})$
94 − 105	97.4	631	5.6	0.356	$0.9000 \pm 0.0361(\mathrm{stat.})\ ^{+0.0822}_{-0.0822}(\mathrm{sys.})\ ^{+0.0011}_{-0.0099}(\mathrm{pdf})$
Mass Bin (GeV/c^2)	$\overline{M_{ee}}$ (GeV/c^2)	N	B	$\epsilon\beta$	$d\sigma^B_{ee}/dM$ (fb / GeV/c^2)
105 − 120	111.1	46	4.6	0.180	$86.45 \pm 14.15(\mathrm{stat.})\ ^{+8.19}_{-8.36}(\mathrm{sys.})\ ^{+5.39}_{-0.25}(\mathrm{pdf})$
120 − 140	128.7	9	3.1	0.215	$7.14\ ^{+3.82}_{-3.82}(\mathrm{stat.})\ ^{+1.08}_{-1.08}(\mathrm{sys.})\ ^{+0.00}_{-0.02}(\mathrm{pdf})$
140 − 200	164.1	16	3.2	0.233	$4.95\ ^{+1.59}_{-1.59}(\mathrm{stat.})\ ^{+0.38}_{-0.38}(\mathrm{sys.})\ ^{+0.02}_{-0.00}(\mathrm{pdf})$
200 − 300	240.7	4	0.7	0.283	$0.67\ ^{+0.63}_{-0.38}(\mathrm{stat.})\ ^{+0.08}_{-0.08}(\mathrm{sys.})\ ^{+0.00}_{-0.00}(\mathrm{pdf})$
300 − 400	343.3	1	0.1	0.325	$0.16\ ^{+0.40}_{-0.14}(\mathrm{stat.})\ ^{+0.03}_{-0.03}(\mathrm{sys.})\ ^{+0.00}_{-0.00}(\mathrm{pdf})$

Table 8.13: Results for the backward Drell-Yan differential cross section $d\sigma^B_{ee}/dM$. N is the number of data events, B is the background estimate, $\epsilon\beta$ is the combined efficiency times correction factor. There is an overall fractional uncertainty of 6.5% from the uncertainty in the integrated luminosity. $\overline{M_{ee}}$ is the value of M_{ee} for which the differential cross section is equal to its average value over the bin as determined from the theoretical prediction.

8.4 Charge Mismeasurement Probability

Since the forward-backward asymmetry is dependent on measurement of the charge of the electron, we must account for the probability P_m that the electron charge is mismeasured. The measured A_{FB} will then be related to the true A_{FB} by a dilution factor $\mathcal{D}$:

$$A_{FB}^{meas} = \mathcal{D} A_{FB}^{true} = \mathcal{D}\left(\frac{\sigma_F - \sigma_B}{\sigma_F + \sigma_B}\right). \tag{8.9}$$

The error on the corrected A_{FB} is

$$\delta A_{FB}^{true} = \sqrt{\left(\frac{A_{FB}^{meas}}{\mathcal{D}^2}\right)^2 (\delta\mathcal{D})^2 + \left(\frac{1}{\mathcal{D}}\right)^2 (\delta A_{FB}^{meas})^2} \tag{8.10}$$

where

$$\delta A_{FB}^{meas} = 2\frac{\sqrt{\sigma_B^2 \delta\sigma_F^2 + \sigma_F^2 \delta\sigma_B^2}}{(\sigma_F + \sigma_B)^2} \tag{8.11}$$

The dilution factor for the CC-CC events is given by

$$\mathcal{D} = 1 - 2P_{m,CC} \tag{8.12}$$

where $P_{m,CC}$ is the probability that the charge of the electron (positron) is mismeasured as positive (negative).

The charge mismeasurement probability is measured by using the same

selection cuts as is used for the signal events, except that two track matches are required so that the charge of both EM objects is obtained. The charge mismeasurement probability is given by

$$P_m = \frac{1}{2} - \sqrt{\frac{1}{4} - \frac{1}{2}\left(\frac{N_{ss}}{N_{os}+N_{ss}}\right)} \tag{8.13}$$

$$\approx \frac{1}{2}\frac{N_{ss}}{N_{os}} \quad \text{if } N_{ss} \ll N_{os} \tag{8.14}$$

where

N_{ss} = total number of same-sign events in the Z-peak region

N_{os} = total number of opposite-sign events in the Z-peak region

The Z-boson peak region is taken to be 86 GeV $< M_{ee} <$ 96 GeV. We find the charge mismeasurement probability for CC electrons to be $P_m = 0.006 \pm 0.001(stat) \pm 0.005(sys)$. The systematic error is determined from the variation in the charge misidentification probability as a function of eta, as shown in Fig. 8.21.

To determine the charge mismeasurement probability as a function of invariant mass, we have modeled the charge mismeasurement probability using a GEANT-based Monte Carlo, then normalized the distribution to data in the Z-peak region. Two methods are used to determine the charge mismeasurement probability in Monte Carlo. In the first method, the reconstructed charge is

compared to the the generated charge. The second method is the same as used in the data. The charge mismeasurement probability versus invariant mass for both methods is shown in Fig. 8.22. Since the two methods give consistent results and the match method inheritantly gives more statistics, we choose to use the match method to model the charge mismeasurement probability. We studied the charge mismeasurement probability separately for forward and backward events and found that they were consistent, as shown in Fig. 8.23. Therefore, we use the overall charge mismeasurement probability for all events. Figure 8.24 shows the charge mismeasurement probability versus invariant mass, which has been normalized to data.

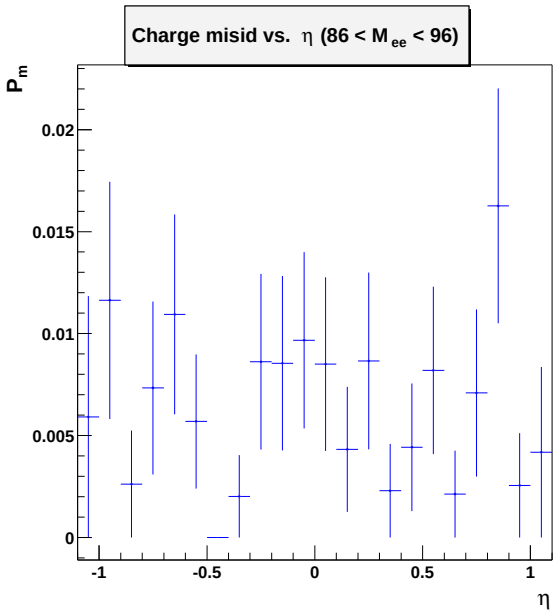

Figure 8.21: Monte Carlo charge misidentification probability vs. η.

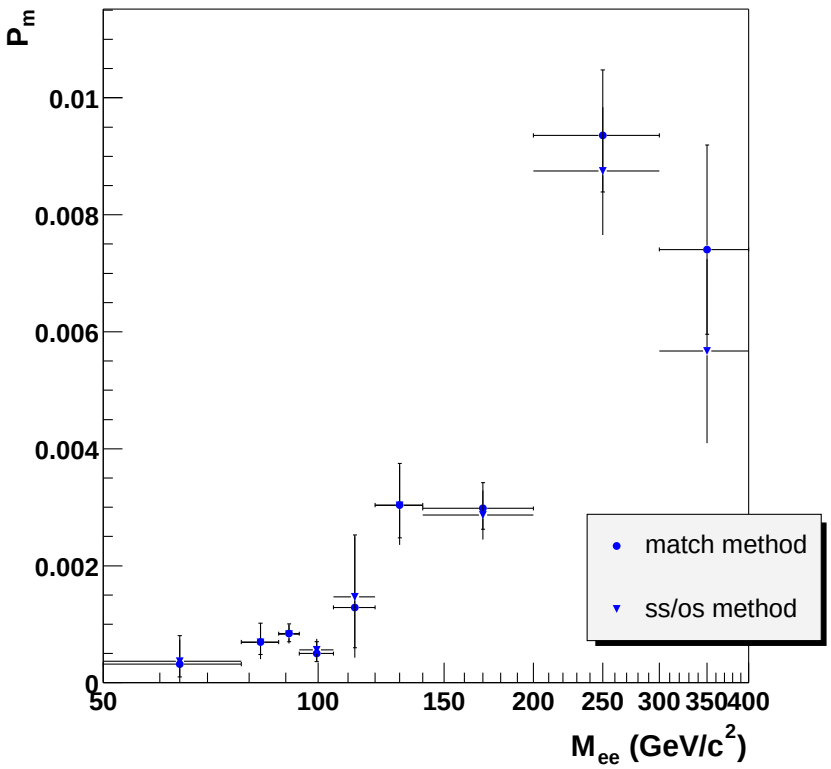

Figure 8.22: Monte Carlo charge mismeasurement probability vs. M_{ee} for match method and same-sign/opposite-sign method. The probabilities are not normalized to data.

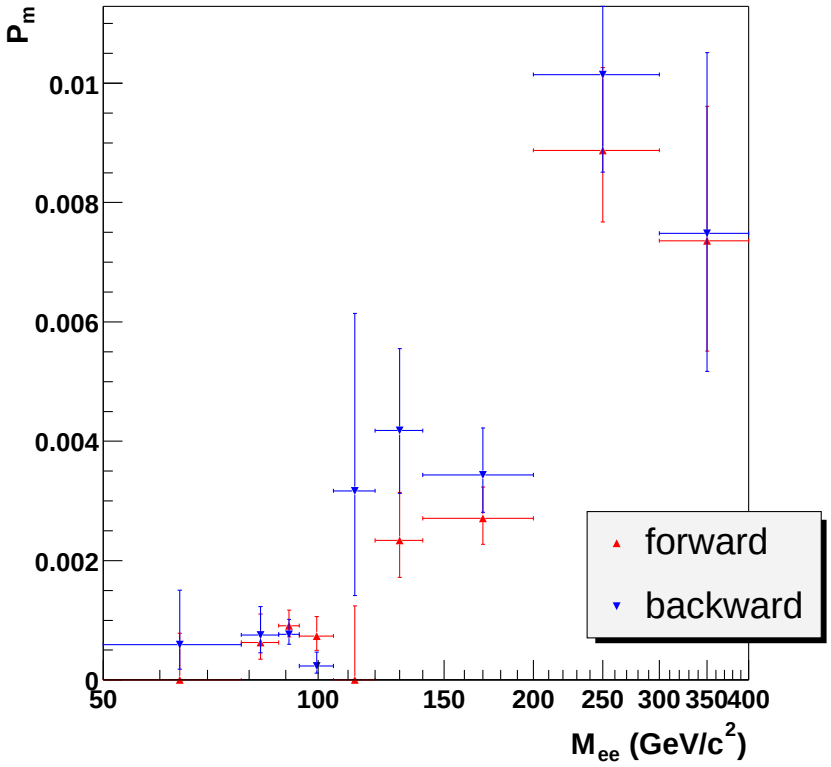

Figure 8.23: Monte Carlo charge mismeasurement probability vs. M_{ee} for forward and backward events. The probabilities are not normalized to data.

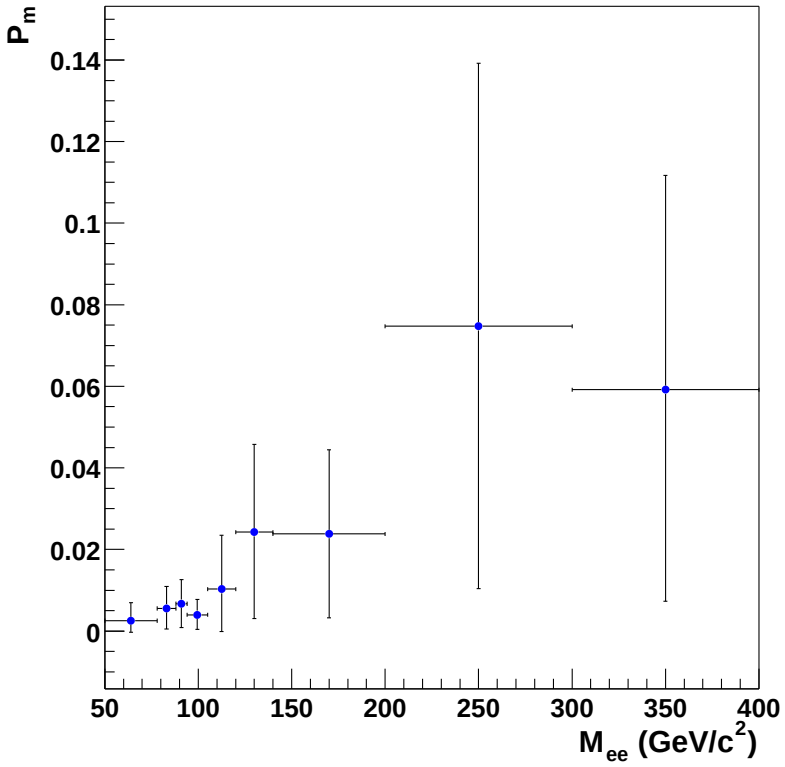

Figure 8.24: Monte Carlo charge mismeasurement probability vs. M_{ee} for all events. The probabilities are normalized to data.

8.5 Forward-Backward Asymmetry Measurement

The results for the forward-backward asymmetry as a function of e^+e^- invariant mass, after correcting for charge mismeasurement, are plotted in Fig. 8.25. The breakdown of the systematic errors is given in Table 8.14 and the final results are given in Table 8.15.

Mass Bin (GeV/c^2)	$\sigma_{\mathcal{D}}$	σ_{bkgd}	σ_{ϵ}	σ_{β}	σ_{PDF}
$70-78$	$^{+0.004112}_{-0.002576}$	0.013489	$^{+0.023625}_{-0.026359}$	0.075212	$^{+0.004998}_{-0.018273}$
$78-88$	$^{+0.001749}_{-0.001635}$	0.002033	$^{+0.013252}_{-0.013641}$	0.083931	$^{+0.007006}_{-0.001931}$
$88-94$	$^{+0.000815}_{-0.000807}$	0.000533	$^{+0.010788}_{-0.010867}$	0.038898	$^{+0.000185}_{-0.000442}$
$94-105$	$^{+0.001843}_{-0.001750}$	0.000988	$^{+0.011172}_{-0.011350}$	0.070709	$^{+0.002931}_{-0.005257}$
$105-120$	$^{+0.010128}_{-0.007934}$	0.012108	$^{+0.022622}_{-0.025789}$	0.052745	$^{+0.029521}_{-0.001260}$
$120-140$	$^{+0.036822}_{-0.036318}$	0.030251	$^{+0.005744}_{-0.006092}$	0.012369	$^{+0.000107}_{-0.000926}$
$140-200$	$^{+0.021906}_{-0.021792}$	0.031671	$^{+0.009701}_{-0.009939}$	0.016602	$^{+0.001580}_{-0.000424}$
$200-300$	$^{+0.110697}_{-0.109925}$	0.045733	$^{+0.008311}_{-0.008469}$	0.014231	$^{+0.001378}_{-0.000083}$
$300-400$	$^{+0.031940}_{-0.031534}$	0.118337	$^{+0.013837}_{-0.014329}$	0.031868	$^{+0.003037}_{-0.002303}$

Table 8.14: Contributions to the systematic error on A_{FB} from uncertainties in the dilution factor ($\sigma_{\mathcal{D}}$), background (σ_{bkgd}), signal selection efficiency (σ_{ϵ}), correction factor (σ_{β}), and parton distribution functions (σ_{PDF}). Units in pb/(GeV/c^2).

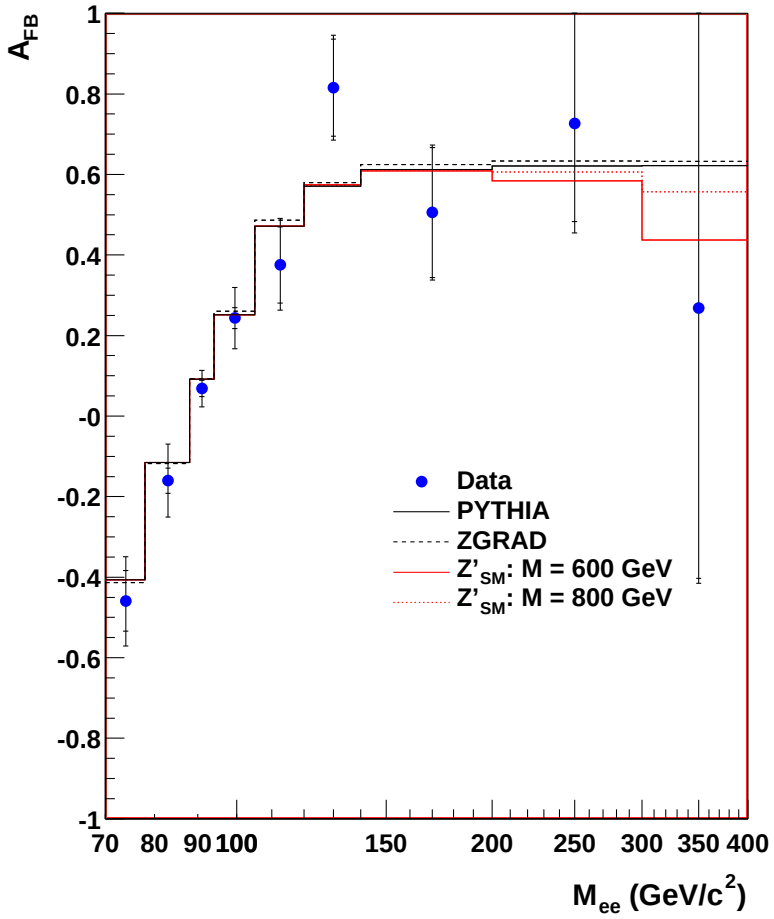

Figure 8.25: Forward-backward asymmetry vs. dielectron invariant mass. The blue circles are the data with the error bars representing the total uncertainty (outer error bars) and the statistical uncertainty only (inner error bars). The black histograms are the Born-level theoretical calculation using PYTHIA (solid) and ZGRAD (dashed). The red histograms show the effect of adding a Z' with standard-model couplings to the theoretical prediction, including full $\gamma/Z/Z'$ interference. The predictions are shown for Z' masses of 600 and 800 GeV/c^2. The width of the Z' was assumed to be 0.03 times the Z' mass.

Mass Bin (GeV/c^2)	$\mathcal{D}$	A_{FB}
$70 - 78$	$0.995\ ^{+0.009}_{-0.006}$	$-0.459 \pm 0.075(\mathrm{stat.})\ ^{+0.080}_{-0.081}(\mathrm{sys.})\ ^{+0.005}_{-0.018}(\mathrm{pdf})$
$78 - 88$	$0.989\ ^{+0.011}_{-0.010}$	$-0.160 \pm 0.031(\mathrm{stat.})\ ^{+0.085}_{-0.085}(\mathrm{sys.})\ ^{+0.007}_{-0.002}(\mathrm{pdf})$
$88 - 94$	$0.987\ ^{+0.012}_{-0.012}$	$0.068 \pm 0.020(\mathrm{stat.})\ ^{+0.040}_{-0.040}(\mathrm{sys.})\ ^{+0.000}_{-0.000}(\mathrm{pdf})$
$94 - 105$	$0.992\ ^{+0.008}_{-0.007}$	$0.243 \pm 0.026(\mathrm{stat.})\ ^{+0.072}_{-0.072}(\mathrm{sys.})\ ^{+0.003}_{-0.005}(\mathrm{pdf})$
$105 - 120$	$0.979\ ^{+0.026}_{-0.021}$	$0.375 \pm 0.095(\mathrm{stat.})\ ^{+0.060}_{-0.060}(\mathrm{sys.})\ ^{+0.030}_{-0.001}(\mathrm{pdf})$
$120 - 140$	$0.952\ ^{+0.043}_{-0.042}$	$0.815 \pm 0.120(\mathrm{stat.})\ ^{+0.050}_{-0.049}(\mathrm{sys.})\ ^{+0.000}_{-0.001}(\mathrm{pdf})$
$140 - 200$	$0.952\ ^{+0.041}_{-0.041}$	$0.505 \pm 0.162(\mathrm{stat.})\ ^{+0.043}_{-0.043}(\mathrm{sys.})\ ^{+0.002}_{-0.000}(\mathrm{pdf})$
$200 - 300$	$0.951\ ^{+0.129}_{-0.129}$	$0.727\ ^{+0.387}_{-0.244}(\mathrm{stat.})\ ^{+0.120}_{-0.120}(\mathrm{sys.})\ ^{+0.001}_{-0.000}(\mathrm{pdf})$
$300 - 400$	$0.882\ ^{+0.105}_{-0.104}$	$0.268\ ^{+1.865}_{-0.671}(\mathrm{stat.})\ ^{+0.127}_{-0.127}(\mathrm{sys.})\ ^{+0.003}_{-0.002}(\mathrm{pdf})$

Table 8.15: The Drell-Yan forward-backward asymmetry results. $\mathcal{D}$ is the dilution factor.

Chapter 9

Conclusions

9.1 Summary

We have studied the Drell-Yan process $p\bar{p} \rightarrow \gamma^*/Z \rightarrow e^+e^-$ in a data set of 177 pb^{-1} using the DØ detector at the Fermilab Tevatron. The observed cross section and kinematic distributions of the e^+e^- pairs are consistent with the Standard Model predictions. The measured raw forward-backward asymmetry was found to be consistent with Monte Carlo predictions based on the Standard Model prediction. After correcting for the final forward-backward asymmetry as a function of the $M_{e^+e^-}$, the forward-backward asymmetry was found to be consistent with the Standard Model over the mass range $70 - 400$ GeV/c^2. The measured differential cross section $d\sigma/dM_{e^+e^-}$ was also found to be consistent with the Standard Model prediction over the same invariant mass range.

9.2 Future Prospects

The differential cross section and forward-backward asymmetry measurements will be improved by adding additional data. DØ will collect ~ 1 fb^{-1} by the end of 2005. The expected integrated luminosity by the end of the Tevatron Run II is $4 - 8$ fb^{-1}. An additional significant improvement in the results will be possible by extending the pseudorapidity coverage of electrons using the endcap calorimeter. This will allow more stringent tests of the Standard Model and searches for new physics at high $M_{e^+e^-}$.

Bibliography

[1] S. L. Glashow, Nucl. Phys. **22**, 579 (1961);
S. L. Weinberg, Phys. Rev. Lett. **19**, 1264 (1967);
A. Salam, Proc. 8^{th} Nobel Symposium, Stockholm, 1968, ed. N. Svartholm (Almqvist and Wiksells, Stockholm 1968) p. 367.

[2] P. W. Higgs, Phys. Rev. Lett. **13**, 508 (1964);
idem Phys. Rev. **145**, 1156 (1966);
F. Englert and R. Brout, Phys. Rev. Lett. **13**, 321 (1964);
G. S. Guralnik, C. R. Hagen, and T. W. Kibble, Phys. Rev. Lett. **13**, 585 (1964).

[3] S. D. Drell and T.-M. Yan, Phys. Rev. Lett. **25**, 316 (1970).

[4] J. H. Christenson et al., Phys. Rev. Lett. **25**, 1523 (1970).

[5] J. J. Aubert et al., Phys. Rev. Lett. **33**, 1404 (1974).

[6] U. Baur, S. Keller, and W.K. Sakumoto, Phys. Rev. D **57**, 199 (1998).

[7] B. Kamal, Phys. Rev. D **57**, 6663 (1998).

[8] R. Hamberg, W.L. van Neerven, and T. Matsuura, Nucl. Phys. B **359**, 343 (1991);
W. L. Van Neerven and E. B. Zijlstra, Nucl. Phys. B **382**, 11 (1992).

[9] J. Ellison and J. Rha, *"Measurement of the Forward-Backward Asymmetry in e^+e^- and $\mu^+\mu^-$ events with DØ in Run II",* DØ Note 3756 (2000).

[10] J. C. Collins and D. E. Soper, Phys. Rev. D **16**, 2219 (1977).

[11] F. Del Aguila, M. Quirós and F. Zwirner, Nucl. Phys. B **287**, 419 (1987);
J. L. Rosner, Phys. Rev. D **35**, 2244 (1987);
J. L. Rosner, Phys. Rev. D **54**, 1078 (1996).

[12] J. L. Hewett, Phys. Rev. Lett. **82**, 4765 (1999).

[13] N. Arkani-Hamed, S. Dimopoulos, and G. Dvali, Phys. Lett. B **429**, 263 (1998);
I. Antoniadis et al., Phys. Lett. B **436**, 257 (1998).

[14] N. Arkani-Hamed, S. Dimopoulos, and G. Dvali, Phys. Lett. B **59**, 086004 (1999).

[15] G. Giudice, R. Rattazzi, and J. Wells, Nucl. Phys. B **544**, 3 (1999);
JoAnne L. Hewett, Phys. Rev. Lett. B **82**, 4765 (1999);
N. Arkani-Hamed, S. Dimopoulos, and G. Dvali, Phys. Rev. D **59**, 086004 (1996).

[16] G. Alexander et al., Z. Phys. C **72**, 365 (1996).

[17] R. Barate et al., Phys. Lett. B **434**, 415 (1998).

[18] M. Acciarri et al., Phys. Lett. B **485**, 71 (2000).

[19] B. Abbott et al., Phys. Rev. Lett. **82**, 24 (1999).

[20] T. Affolder et al., Phys. Rev. Lett. **87**, 13 (2001).

[21] D. Acosta et al., hep-ex/0411059, (2004).

[22] R. Brock et al., *"Report of the Working Group on Precision Measurements",* Proceedings of Physics at Run II: QCD and Weak Boson Physics, Fermilab-Conf-01-282-E, hep-ex/0011009 (2000).

[23] Fermilab Beam Division, *Fermilab's Chain of Accelerators,* available at `http://www-bd.fnal.gov/public/chain.html`

[24] B. M. Evanger et al., *"Concepts Rookie Book",* available at `http://beamdocs.fnal.gov/DocDB/0010/001023/001/Concepts%20Rookie%20Book%20v3.pdf`.

[25] B. W. Worthel, *"Booster Rookie Book",* available at `http://beamdocs.fnal.gov/DocDB/0010/001022/001/Booster%20V3_0.pdf`.

[26] J. P. Morgan et al., *"Pbar Rookie Book",* available at `http://beamdocs.fnal.gov/DocDB/0010/001021/001/Pbar%20Rookie%20Book.pdf`.

[27] DØ Collaboration, V. Abazov et al., *"The Upgraded DØ Detector",* in preparation for submission to Nucl. Instrum. Methods Phys. Res. A;
T. LeCompte and H. T. Diehl, Ann. Rev. Nucl. Part. Sci. **50**, 71 (2000).

[28] DØ Collaboration, *"DØ Silicon Tracker Technical Design Report",* DØ Note 2169, (1994).

[29] D. Adams et al., *"Central Fiber Tracker Technical Design Report",* DØ Note 4164, (1999).

[30] M. Adams et al., *"Design Report of the Central Preshower Detector for the DØ Upgrade",* DØ Note 3014, (1996).

[31] DØ Collaboration, *"The DØ Upgrade: Forward Preshower, Muon System and Level 2 Trigger",* DØ Note 2894, (1996).

[32] J. Kotcher, *"Design, Performance, and Upgrade of the DØ Calorimeter",* Fermilab Conf-95/007-E, (1995).

[33] K. De et al., *"Technical Design Report for the Upgrade of the ICD for DØ Run II",* DØ Note 2686, (1997).

[34] H. T. Diehl et al., *"Technical Design of the Central Muon System",* DØ Note 3365, (1997).

[35] G. Alexeev et al., *"Technical Design Report of the DØ Forward Muon Tracking Detector Based on Mini-drift Tubes",* DØ Note 3366, (1997).

[36] A. Lo, C. Miao, and R. Partridge, *"Luminosity Monitor Technical Design Report",* DØ Note 3320, (1997).

[37] M. Abolins et al., *"DØ Run II Level 1 Trigger Framework Technical Design Report",* available at `http://www.pa.msu.edu/hep/d0/ftp/l1/framework/l1fw_tdr_05june98.txt`

[38] D. Edmunds, S. Gross, and P. Laurens, *"Technical Design Report for the Level 2 Global Processor",* DØ Note 3402, (1998).

[39] R. Angstadt et al., *"The DZERO Level 3 Data Acquisition System",* IEEE Trans. on Nuclear Science, Vol. 51, No. 3, 445 (2004).

[40] A. Boehnlein et al., *"Description of DØ L3 Trigger Software Components",* DØ Note 3630, (1999).

[41] H. Greenlee, *"The DØ Kalman Track Fit",* DØ Note 4303, (2003).

[42] H. Greenlee, *"The DØ Interacting Propagator",* DØ Note 4293, (2003).

[43] A. Schwartzman and M. Narain, *"Primary Vertex Selection",* DØ Note 3906, (2001).

[44] A. Schwartzman and M. Narain, *"Probabilistic Primary Vertex Selection",* DØ Note 4042, (2002).

[45] J-R Vlimant, U. Bassler, G. Bernardi, and S. Trincz-Duvoid *"Technical description of the T42 Algorithm for the calorimeter noise suppression",* DØ Note 4146, (2003).

[46] N. Hadley, *"Cone Algorithm for Jet Finding",* DØ Note 904, (1989).

[47] B. Abbott et al., *"Determination of the Absolute Jet Energy Scale in the DZERO Calorimeters",* Nucl. Inst. and Meth. B, , Vol. 424, No. 2-3, 352 (1999).

[48] J. Pumplin, D. R. Stump, J. Huston, H. L. Lai, P. Nadolsky, and W. K. Tung, J. High Energy Phys. JHEP07, 012 (2002).

[49] T. Sjöstrand, P. Eden, C. Friberg, L. Lonnblad, G. Miu, S. Mrenna, and E. Norbin, Computer Physics Commun. **135**, 238 (2001).

[50] E. Barberio and Z. Wąs, Comput. Phys. Commun. **79**, 291 (1994); E. Barberio, B. van Eijk, and Z. Wąs, *ibid.* **66**, 115 (1991).

[51] R. Brun et al., CERN Program Library Writeup W5013 (1993).

[52] S. Eno, N. Hadley, M. Verzocchi, and J. Zhu, *"Status of PMCS_EM",* DØ Note 4062, Version 1.0, (2002).

[53] D. Chapin et al., *"Measurement of Z→ee and W→enu Production Cross Sections with $|\eta| < 2.3$",* DØ Note 4403, Version 1.0, (2004).

[54] Junjie Zhu, *"Determination of Electron Energy Scale and Energy Resolution using P14 zee data",* DØ Note 4323, Version 1.0, (2003).

[55] Marc Paterno, *"Calculating Efficiencies and Their Uncertainties",* FERMILAB-TM-2286-CD (2004).

[56] Gervasio Gómez, *"Extraction of the Width of the W Boson from a Measurement of the Ratio of the W and Z Cross Sections"* (DØ Ph.D Thesis), unpublished, (1999).

[57] U. Baur, O. Brein, W. Hollik, C. Schappacher, D. Wackeroth, Phys. Rev. D **65**, 033007 (2002).

[58] J. Huston et al., *"Inclusive Jet Production, Parton Distributions, and the Search for New Physics",* hep-ph/0303013, (2003).

[59] U. Yang and Y. Kim, *"ISR Studies on Drell-Yan",* Fermilab MC Workshop (2003), available at `http://cepa.fnal.gov/patriot/mc4run2/MCTuning/031204/unki.pdf`

[60] B. Tiller and T. Nunnemann, *"Measurement of the differential Z0-boson production cross-section as function of transverse momentum",* DØ Note 4660, (2004).